BIOLOGICALLY INSPIRED APPROACH FOR ROBOT DESIGN AND CONTROL

By

Jianguo Zhao

A DISSERTATION

Submitted to
Michigan State University
in partial fulfillment of the requirements
for the degree of

Electrical Engineering - Doctor of Philosophy

2015

ABSTRACT

BIOLOGICALLY INSPIRED APPROACH FOR ROBOT DESIGN AND CONTROL

By

Jianguo Zhao

Robots will transform our daily lives in the near future by moving from controlled industrial lines to unstructured and uncertain environments such as home, offices, or outdoors with various applications from healthcare, service, to defense. Nevertheless, two fundamental problems remain unsolved for robots to work in such environments. On one hand, how to design robots, especially meso-scale ones with sizes of a few centimeters, with multiple locomotion abilities to travel in the unstructured environment is still a daunting task. On the other hand, how to control such robots to dynamically interact with the uncertain environment for agile and robust locomotion also requires tremendous efforts. This dissertation tries to tackle these two problems in the framework of biologically inspired robotics.

On the design aspect, it will be shown how biologically principles found in nature can be used to build efficient meso-scale robots with various locomotion abilities such as jumping, wheeling, and aerial maneuvering. Specifically, a robot (MSU Jumper) with continuous jumping ability will be presented. The robot can achieve the following three performances simultaneously. First, it can perform continuous steerable jumping based on the self-righting and the steering capabilities. Second, the robot only requires a single actuator to perform all the functions. Third, the robot has a light weight (23.5 g) to reduce the damage from landing impacts. Based on the MSU Jumper, a robot (MSU Tailbot) with multiple locomotion abilities is discussed. This robot can not only wheel on the ground but also jump up to overcome obstacles. Once leaping into the air, it can also control its body angle using an active tail to dynamically maneuver in mid-air for safe landings.

On the control aspect, a novel non-vector space control method that formulates the problem in the space of sets is presented. This method can be easily applied to vision based control by considering images as sets. The advantage of such a method is that there is no need to extract and track features during the control process, which is required by traditional methods. Based on the non-vector space approach, the compressive feedback is proposed to increase the feedback rate and reduce the computation time. This method is ideal for the control of meso-scale robots with limited sensing and computation ability.

The bio-inspired design illustrated by the MSU Jumper and MSU Tailbot in this dissertation can be applied to other robot designs. Meanwhile, the non-vector space control with compressive feedbacks lays the foundation for the control of high dynamic meso-scale robots. Together, the biologically inspired method for the design and control of meso-scale robots will pave the way for next generation bio-inspired, low cost, and agile robots.

ACKNOWLEDGMENTS

First and foremost, I would like to thank and express my great appreciation and gratitude to my advisor Dr. Ning Xi. Without his support, I would not be able to initiate my PhD study in US. Moreover, without his guidance, it was impossible for me to finish the research presented this dissertation. His insightful vision and high standard for research also made me a qualified researcher.

I would like to thank my dissertation committee members: Dr. Xiaobo Tan, Dr. Matt W Mutka, Dr. Li Xiao, and Dr. Hassan Khalil. I greatly appreciate their valuable feedback and discussions throughout my entire PhD process.

My many thanks go to my lab members: Dr. Yunyi Jia, Yu Cheng, Bo Song, Liangliang Chen, Dr. Ruiguo Yang, Dr. Erick Nieves, Dr. Hongzhi Chen, Dr. Chi Zhang, Dr. Yong Liu, Dr. Bingtuan Gao, Dr. Jing Xu, Dr. King W.C. Lai, Dr. Carmen K.M. Fung, and Dr. Yongliang Yang. I was fortunate to collaborate with many of them for various projects which widely broadened my view. Many professors spent their time as visiting scholars in our lab in the past few years. I want to thank them for many extracurricular activities, which provide many joys besides research.

I would also like to thank undergraduate students who worked with me on various parts of this dissertation. Among them are Tianyu Zhao, Chenli Yuan, Weihan Yan, Hongyi Shen, and Zach Farmer. By working with them, I also gained experiences on how to supervise students for various projects.

Finally, I thank my parents and my wife for their endurance and support for such a long commitment for the PhD study.

TABLE OF CONTENTS

LIST OF TABLES

LIST OF FIGURES

Chapter 1

Introduction

1.1 Background

Animals employ various methods to move in different environments. On land, worms and snakes can crawl or burrow, frogs and flea can hop or jump, horses and cheetah can walk or run. In addition, squirrels can climb on vertical tree trunks, while geckoes can even run on ceilings. In the air, birds can glide without flapping their wings or soar for sustained gliding with the use of air movements. Many insects such as bees and hummingbirds can hover to stay stationary. And of course birds and insects can fly elegantly by flapping their wings. In water, most fish can swim by undulation. Some of them such as scallops and squids can swim by jet propulsion. Besides, some insects such as water striders and fish spiders can move on the surface of water by surface tension force [31].

Recently, many robotic systems have been built based on how animals move, which is termed as biologically inspired robots [32, 33]. Such robots have similar locomotion abilities found in animals such as climbing robots, fish robots, flying robots, walking robots, and jumping robots. Among them, meso-scale robots with sizes of a few centimeters are very attractive because they have several advantages compared with large size bio-inspired robots. First, due to their small size, they only have a small number of components. Therefore, they can be built with a low cost by using current fabrication technology such as 3D printing. Second, they can access narrow environments where large robots cannot go. Third, also due to their small sizes, they are not noticeable which makes them ideal platforms for applications such as military surveillance.

With the advantages for meso-scale robots, they can be used for many applications. A particular example is search and rescue. In natural disasters such as earthquakes, many victims are trapped under the disaster site. However, it would be dangerous to directly send humans to search those survivors. In this case, many low cost small robots can be thrown into the area from aerial or terrestrial vehicles. With multiple locomotion capabilities, they can move around in the area. With various sensors such as cameras, they can also cooperatively search the area and locate the position of survivors. Based on the information provided by them, we can rescue those survivors more effectively and safely.

Besides search and rescue, many other applications also exist. These small robots can be used for mobile sensor nodes to form mobile sensor networks, which can be used for environmental monitoring and surveillance. They are especially suitable platforms to verify and study cooperative control of many robots due to their low costs. With their repeatable locomotion capability, they can also be used for experiments to test fundamental biological hypothesis when it is impossible or not reliable to use animals for those experiments. For example, Chen, Zhang, and Goldman used small legged robots to investigate how small animals can locomote in granular media such as sands and proposed the theory of terradynamics [34].

Due to their advantages and applications, many meso-scale robots have been built in the last decade. For example, the Biomimimetic Millisystems Lab has built several meso-scale terrestrial robots. DASH is a 16 gram hexapedal robot that can run fast and still work after fall from a 10m height [35]. MEDIC, also a hexapedal robot, can overcome obstacles [36]. OctoRoACH can use a tail for dynamic and fast turning [37]. VelociRoACH can run at a very fast speed (2.7 m/s) by considering the aerodynamic effect [38].

Besides the meso-scale terrestrial robots, many other robots of similar sizes have been built as well. The robobee built by the Microrobotics group at Harvard University is a particular example [39]. The 100 mg robot that can fly with an external power supply [40] is fabricated by a novel manufacturing method called pop-up book MEMS [41]. Small robots that are used to study the swarm behavior of many robots are also developed such as the Kilobot which is a low cost robot system [42].

1.2 Challenges and Objectives

Centimeter scale robots discussed in the previous section will locomote in natural environments. Since natural environments are unstructured and uncertain, these robots should satisfy two basic requirements in order for successful locomotion in such environments. On one hand, due to their small size, there is no single universal and energy efficient locomotion method for unstructured environments. Therefore, these robots should have multiple locomotion methods or multi-mode locomotion. On the other hand, they should be able to dynamically interact with uncertain environments to respond to different situations. In this case, real time onboard control with sensing, computation, and control capabilities is necessary for those meso-scale robots.

To address these two basic requirements, two challenges exist. First, with a small size, there is only a limited design space, and we can only used a limited number of actuators. Therefore, it is difficult to achieve the multi-mode locomotion within a small size. Second, with a small size, the robot can only have limited computation power and limited sensing capability using embedded systems. As a result, it is difficult to achieve real time onboard control within a small size.

The objectives for the research presented in this dissertation are to investigate how biological principles can be used to address the previous two challenges, i.e., how biological inspirations can be employed for the design and control for meso-scale robots so that they can achieve multi-mode locomotion with real time onboard control to travel and interact with unstructured and uncertain environments. The specific focuses on the design and control are briefly described in the following.

On the design side, we first focus on how can meso-scale robots jump efficiently with biological inspirations. The detailed requirements can be summarized in three aspects. First, to make jumping a valid locomotion method, the robot should be able to perform continuous steerable jumping. Towards this goal, the robot should have multiple functions including jumping, self-righting from the landing position, and changing the jumping direction—steering. Second, we aim to accomplish the multiple functions with the minimum number of actuators. Minimum actuator design can reduce the robot's weight, thereby improving the robot's jumping performance. Third, the robot's weight should be small. Specifically, the mass should be less than 30 grams. With a light weight, each jump consumes less energy for the same jumping height, which can increase the jumping times due to the robot's limited energy supply. Moreover, a lightweight robot is less susceptible to the damage from the landing impact.

The second focus on the design side is to achieve the aerial maneuvering capability once the robot jumps into the air. Although a robot that satisfies the previous objective can jump repetitively, it cannot control its mid-air orientation. Orientation control, however, can ensure a safe landing posture for the robot to protect it from damage, especially for landing on hard surfaces. Moreover, as a sensing platform, we need to control the mid-air orientation for airborne communication towards a desired direction [43]. Based on these two reasons, it is critical that the robot's mid-air orientation can be controlled effectively. Additionally, it is more energy efficient to use wheeled locomotion when no obstacle exists. Therefore, we further require the robot to be able to wheel on the ground.

On the control side, we focus on the vision based control for meso-scale robots since vision is adopted by almost all insects or animals for dynamic interaction with uncertain environment. For example, a bee can use vision to land on arbitrary surfaces without knowing its distance to that surface and its current speed [44].

Nevertheless, traditional vision based control approaches need to extract features and track those features during the control process. Feature extraction and tracking are difficult, especially for natural environments. Therefore, we use a control approach that considers sets as the state of the system as apposed to traditional control which considers vectors as the state. Since the linear structure of the vector space is not available in this space, this method is called the non-vector space control in this dissertation. It can be readily applied to vision based control by considering images as sets.

Moreover, since miniature robots, with limited computation power, cannot deal with the large amount of information from images, we propose the idea of compressive feedback: instead of feedback the whole image for feedback control, only an essential portion of the image is used for feedback. This method is incorporated to the non-vector space approach, which can increase the feedback rate and decrease the computation time, making vision based control possible for meso-scale robot with a limited computation power.

1.3 Literature Review

1.3.1 Biological Inspired Robot Locomotion

In recent years, roboticists build many robots that can mimic the locomotion abilities found in animals. Due to the large amount of existing literature, a comprehensive review is impossible. Therefore, we focus on the review of robots that have jumping ability, which is the main focus of the research presented in this dissertation.

Many robots with the jumping ability have been built in the past decade, and there exist several doctoral dissertations for this topic [45, 46, 47]. All of the existing designs accomplish jumping by an instant release of the energy stored in the robot. As a result, we can classify all of the robots with the jumping ability by their energy storage methods.

The most popular method to store energy is based on traditional springs such as compression, extension, or torsion springs. The frogbot stores and releases the energy in an extension spring through a geared six bar mechanism [1]. The old surveillance robot has a jumping mechanism similar to the frogbot [2], while the new one switches to a torsion spring actuated four bar mechanism [3]. The intermittent hopping robot also employs a geared six bar mechanism for jumping [4]. The mini-whegs utilizes a slip gear system to store and release the energy in an extension spring via a four bar mechanism [5]. With torsion springs, a jumping robot for Mars exploration is designed with a novel cylindrical scissor mechanism [48]. The old Grillo robot employs a motor driven eccentric cam to charge a torsion spring that actuates the rear legs [49]; the new prototype switches to two extension harmonic-wire springs [6, 7]. The wheel-based stair-climbing robot with a soft landing ability is based on four compression springs [8]. The EPFL jumper V1 can achieve a jumping height about 1.4 meter with torsion springs charged and released by a motor driven cam system [9]. This robot is later improved to add the self-recovery capability [10] and the jumping direction changing ability [11]. The multimodal robot can jump up to 1.7 meter based on two symmetrical extension spring actuated four bar mechanisms [12]. Our first generation jumping robot relies on compression springs [13], and the second one employs torsion springs [14].

The elastic elements, or customized special springs, are the second method for energy storage. The scout robot employs a motor driven winch to charge a single bending plate spring and release it to directly strike the ground for jumping [15]. The compact jumping robot utilizes an elastic strip to form closed elastica actuated by two revolute joints [50, 16]. The MIT microbot charges the energy to two symmetrical carbon fiber strips with dielectric elastomer actuators (DEA) [51, 17]. The Jollbot, with a spherical structure formed by several metal semi-circular hoops, deforms the spherical shape to store energy [18]. A similar idea is utilized in the deformable robot, but the hoop material is replaced by shape memory alloy (SMA) [19, 52]. The flea robot also uses SMA to actuate a four bar mechanism for jumping [20]. The mesoscale jumping robot employs the SMA as a special spring to implement the jumping mechanism as well [53].

The third method to store energy for jumping is based on compressed air. In this method, the robot carries an air tank and a pneumatic cylinder. The sudden release of air in the tank forces the cylinder to extend. The rescue robot [21, 22] and the patrol robot [23] employ the cylinder's extension to strike the ground for jumping. Instead of striking the ground, the quadruped Airhopper accomplishes jumping with several cylinder actuated four bar mechanisms [54, 24]. With a biped structure, the Mowgli robot—different from other pneumatic-based jumping robots—uses several pneumatic artificial muscles for jumping [25].

In addition to the above three methods, several other approaches exist. The pendulum jumping machine generates energy for jumping from the swing of arms [26]. The jumping

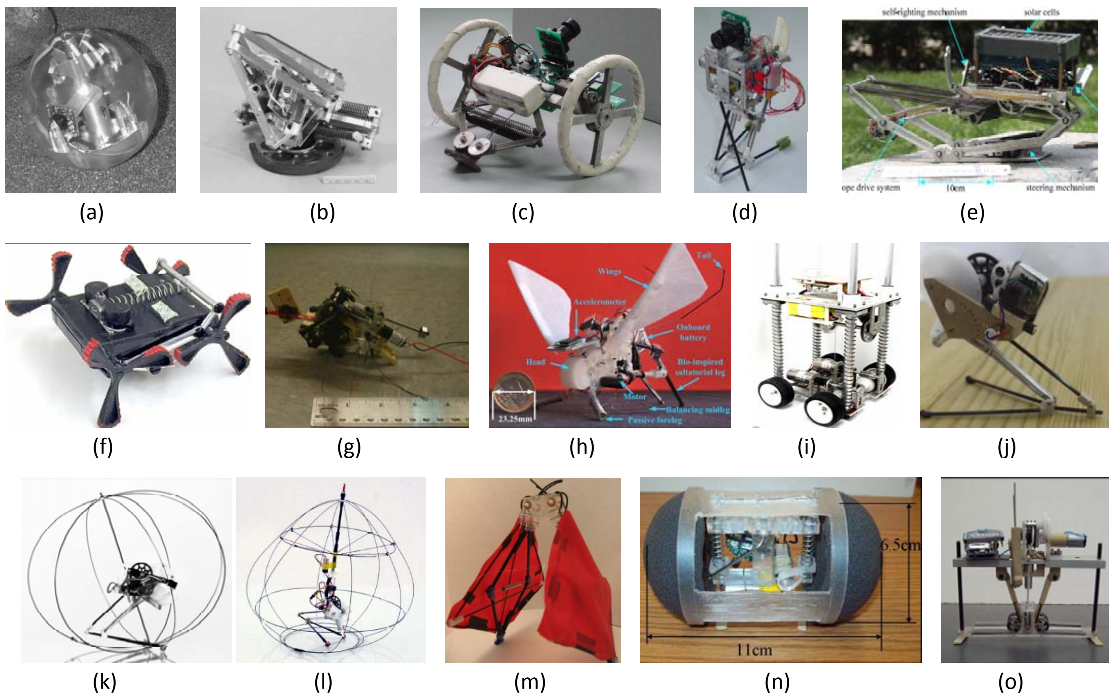

Figure 1.1 Existing jumping robots based on traditional springs: (a) the first generation of frogbot [1]; (b) the second generation of frogbot [1]; (c) the old surveillance robot [2]; (d) the new surveillance robot [3]; (e) the intermittent hopping robot [4]; (f) the MiniWhegs [5]; (g) the old Grillo robot [6]; (h) the new Grillo robot [7]; (i) the wheel-based stair-climbing robot [8]; (j) the EPFL jumper V1 [9]; (k) the EPFL jumper V2 [10]; (l) the EPFL jumper V3 [11]; (m) the multimodal robot [12]; (n) the first generation MSU jumper [13]; (o) the second generation MSU jumper [14].

robot developed by the Sandia National Labs [27] and recently improved by Boston Dynamics [28] uses the energy from hydrocarbon fuels and can achieve the largest jumping height to date. The robot based on microelectromechanical technology is the smallest jumping robot in literature [55, 29]. The voice coil actuator based robot charges energy into an electrical capacitor instead of a mechanical structure [30].

Although jumping is effective in overcoming obstacles, when no obstacle exists, the wheeled locomotion is the most energy efficient method [56]. Therefore, researchers have built hybrid wheeled and jumping robots as well. Examples include the scout robot [57], the mini-whegs [5], the rescue robot [21], the scoutbot [23], the stair climbing robot [8], and the

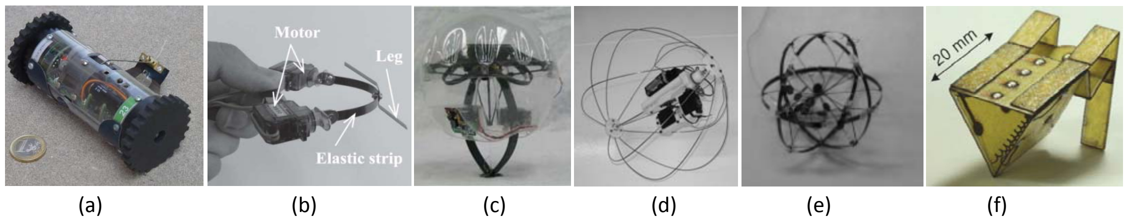

Figure 1.2 Existing jumping robots based on customized springs: (a) the scout robot [15]; (b) the compact jumping robot [16]; (c) the MIT microbot [17]; (d) the Jollbot [18]; (e) the deformable robot [19]; (f) the flea robot [20].

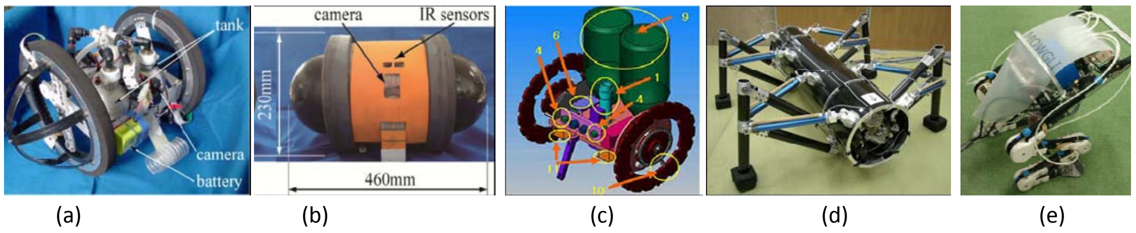

Figure 1.3 Existing jumping robots based on compressed air: (a) the old rescue robot [21]; (b) the new rescue robot [22]; (c) the patrol robot [23]; (d) the quadruped Airhopper [24]; (e) the Mowgli robot [25].

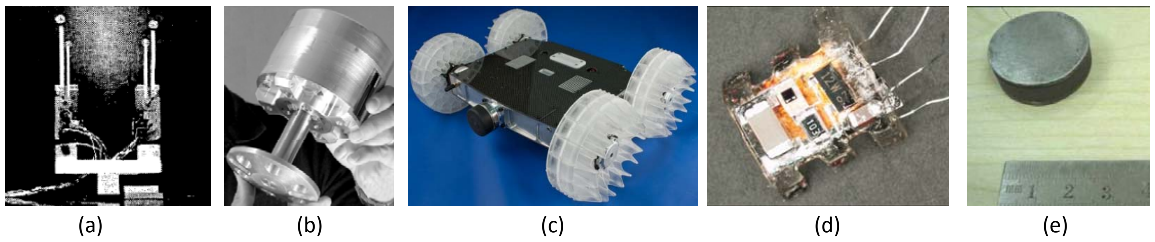

Figure 1.4 Other existing jumping robots: (a) the pendulum jumping machine [26]; (b) the old sand flea [27]; (c) the new sand flea [28]; (d) the jumping microrobot [29]; (e) the voice coil based jumper [30].

recent sand flea robot [28]. Note that some of the robots listed here are already discussed before for robots with jumping capability.

Besides the hybrid wheeled and jumping locomotion, the mid-air orientation control or aerial maneuvering ability can make the robot land on the ground with a desired safe posture. Many animals are able to perform aerial maneuvering for various purposes. For example, a cat can always land on the ground with its foot whatever initial posture it may have by twisting its body in mid-air [58]. Recently, researchers find that geckoes can use tails to maneuver their postures during free fall [59]. Moreover, the tails can assist the rapid vertical climbing and gliding process. Also with the tails, a lizard can actively control its pitch angle after leaping into the air [60]. In fact, lizards without tails tend to rotate in the air much more than those with tails [61].

In recent years, inspired by the tail's functions in animals [59, 60], researchers built robots to investigate the merits of tails for dynamic and rapid maneuvering. Chang-Siu *et al.* added a tail to a wheeled robot to control the robot's pitch angle during free fall [62]. Johnson *et al.* also appended a tail to a legged robot to control the robot's pitch angle for safe landing from some height [63]. Demir *et al.* found that an appendage added to a quadrotor could enhance the flight stabilization [64]. Briggs *et al.* added a tail to a cheetah robot for rapid dynamic running and disturbance rejection [65]. Kohut *et al.* studied the dynamic turning of a miniature legged robot using a tail on the ground [66]. Casarez *et al.* also performed similar study for small legged robots [67].

1.3.2 Biological Inspired Robot Control

Biological inspirations are also used to control robots since animals can dynamically interact with the environment in elegant ways. A comprehensive review for bio-inspired robot control is also impossible. Therefore, we focus on the vision based control since vision is the most sophisticated and universal feedback mechanism in insects or animals.

In biological society, researchers try to unravel how small insects such as fruit flies or honeybees use vision as a perception method to achieve marvelous aerial maneuvering such as landing control or obstacle avoidance. Breugel and Dickinson used a high speed 3D tracking system to record the landing process for fruit flies and found the landing process could be divided into three steps [68]. Later, they proposed a distance estimation algorithm that might be used by insects during the landing process [69]. However, Baird *et al.* found a universal landing strategy for bees without knowing the current distance to the landing surface from extensive experiments [44]. Different from landing, Fuller *et al.* found that flying Drosophila combined vision feedback with antennae sensor to stabilize its flight motion and was robust to perturbations [70]. Muijres *et al.* also studied how flies would escape from potential predators or evasive maneuvers using vision as feedback [71].

Recently, to create robots that can achieve similar feats found in such insects or small flying animals, researchers performed extensive research in both hardware and algorithms for biologically inspired vision based control of miniature robots. On the hardware side, various bio-inspired vision sensors that have large field of view have been built. A biomimetic compound eye system is engineered with a hemispherical field of view for fast panoramic motion perception [72]. An arthropod-inspired camera is fabricated by combining elastomeric optical elements with deformable arrays of silicon photodetectors [73].

On the algorithm side, many researchers studied the vision based control using the traditional optical flow approach. For example, the optical flow algorithm is utilized to avoid obstacles [74]. Nonlinear controllers are designed with the optical flow information to land a unmanned aerial vehicle on a moving platform [75]. The optical flow algorithm is implemented to control the altitude of a $101mg$ flapping-wing microrobot on a linear guide [76]. Besides the methods based on optical flow, extensively studies are performed on how bees exploited visual information to avoid obstacle, regulate flight speed, and perform smooth landings. Moreover, these observations are verified on terrestrial and airborne robotic vehicles [77].

Vision based control belongs to a general problem called visual servoing, where the visual information is used to control the motion of a mechanical system [78]. In recent years, different from traditional visual servoing approach with feature extraction and tracking, researchers also tried to use all the intensities or illuminance from an image to perform the so called featureless visual servoing. This approach eliminates the feature extraction and tracking, and is especially suitable for embedded applications with limited computation power. The image moments are used as a generalized feature to perform visual servoing [79]. A featureless servoing method is created by applying a Gaussian function to the image, and then define the error in the transformed domain [80]. Each illuminance is directly used as a feature point to derive the control law [81]. The mutual information between two images is utilized to formulate the servoing problem [82]. All the intensities in an image are also used to devise a bio-plausible method to study the hovering problem for small helicopters [83] .

1.4 Contributions

The contributions for this dissertation can be summarized into two aspects: design and control. For the design aspect, the bio-inspired design approach can be applied to other meso-scale robot designs. On the control aspect, the non-vector space approach can used for any control system where the state can be considered as a set.

Based on biological inspirations, the designed MSU Jumper can achieve the following three performances simultaneously, which distinguishes it from the other existing jumping robots. First, it can perform continuous steerable jumping based on the self-righting and the steering capabilities. Second, the robot only requires a single actuator to perform all the functions. Third, the robot has a light weight (23.5 grams) to reduce the damage resulting from the landing impact. Experimental results show that, with a 75° take-off angle, the robot can jump up to 87cm in vertical height and 90cm in horizontal distance. The latest generation can jump up to 150cm in height [84].

Based on the jumping robot, the MSU tailbot can not only wheel on the ground but also jump up to overcome obstacles. Once leaping into the air, it can control its body angle using an active tail to dynamically maneuver in mid-air for safe landings. We derive the mid-air dynamics equation and design controllers, such as a sliding mode controller, to stabilize the body at desired angles. To the best of our knowledge, this is the first miniature (maximum size 7.5 cm) and lightweight (26.5 g) robot that can wheel on the ground, jump to overcome obstacles, and maneuver in mid-air. Furthermore, this robot is equipped with on-board energy, sensing, control, and wireless communication capabilities, enabling tetherless or autonomous operations.

On the control side, this dissertation presents a non-vector space control approach that can be applied to vision based control. Considering images obtained from image sensors as sets, the dynamics of the system can be formulated in the space of sets. With the dynamics in the non-vector space, we formulate the stabilization problem and design the controller. The stabilization controller is tested with a redundant robotic manipulator, and the results verify the proposed theory. The non-vector space method, unlike the traditional image based control method, we do not need to extract features from images and track them during the control process. The approach presented can also be applied to other systems where the states can be represented as sets.

Based on the non-vector space controller, compressive feedback is proposed to address the large amount of data from the image. Instead of feedback the full image, only a compressed image set is employed for feedback. To the best of our knowledge, directly using the compressive feedback for control without recovery has never been studied before. The compressive feedback is applied to the non-vector space control for visual servoing. With the compressive feedback, the amount of data for control can be reduced. The stability for the compressive feedback based non-vector space control is investigated. Moreover, experimental results using the redundant manipulator verify the theoretical results.

1.5 Outline of This Dissertation

The dissertation is divided into two parts: design and control. Chapter 2 and 3 discuss the bio-inspired design, while Chapter 4 and 5 present the bio-inspired control. Chapter 6 discusses the preliminary experimental results to verify the bio-inspired control using the MSU tailbot. Chapter 7 concludes the dissertation and outlines future research work. The specific contents for each chapter are discussed as follows.

Chapter 2 presents the design of MSU Jumper. The mathematical model of the jumping process will be firstly discussed. After that, the mechanical design for the four mechanisms will be elaborated. Then an optimal design is performed to obtain the best mechanism dimensions. Finally, we present the implementation details, experimental results, and comparison with existing jumping robots.

Chapter 3 discusses the design of MSU tailbot. First, the detailed robot design is presented. Then, the dynamics modeling for aerial maneuvering is elaborated and the problem is formulated in the standard nonlinear control form. Based on the dynamics model, a sliding mode controller is designed. Finally, we present experimental results for aerial maneuvering and demonstrate the multi-modal locomotion abilities of the robot.

Chapter 4 introduces the non-vector space control. First of all, the dynamics in the non-vector space is introduced with tools from mutation analysis. After that, the stabilization problem in the non-vector space is introduced, where the stabilizing controller is designed. Finally, the experimental results using a redundant manipulator are given to validate the theory.

Chapter 5 discusses the idea of compressive back. First of all, the basics of compressive sensing are reviewed. After that, the stabilizing controller design based on full feedback and compressive feedback are discussed. With the designed controller, the stability analysis is performed for sparse and approximate sparse feedback. Then, the theory is applied to vision based control. Finally, we present the testing results using the redundant robotic manipulator.

Chapter 6 shows the experimental setup to validate the non-vector space theory using the tailbot. It also shows the preliminary experimental results by letting the robot fall from some height, and use the vision feedback from a miniature camera to control its body orientation.

Chapter 7 summarizes the dissertation and outlines future works.

Chapter 2

MSU Jumper: A Biologically Inspired Jumping Robot

2.1 Introduction

In nature, many small animals or insects such as frog, grasshopper, or flee use jumping to travel in environments with obstacles. With the jumping ability, they can easily clear obstacles much larger than their sizes. For instance, a froghopper can jump up to 700 mm—more than one hundred times its size (about 6.1 mm) [85].

There are three reasons to employ jumping as a locomotion method for mobile robots. First, jumping enables a robot to overcome a large obstacle in comparison to its size. In fact, the ratio between the jumping height and the robot size can be 30 [20]. In contrast, wheeled locomotion on land cannot overcome obstacles larger than the wheel diameter. For example, the Mars rover, even with a special rocker-bogie suspension system, can only overcome obstacles with sizes at most 1.5 times the wheel diameter [1]. Second, jumping provides the best tradeoff between the locomotion efficacy (height per gait) and the energy efficiency (energy per meter) among various locomotion methods such as walking, running, or wheeled locomotion [86]. Third, the wireless transmission range increases when a robot jumps into the air [87]. As shown in [43], when one robot is elevated one meter above the ground, the communication range is about six times the range when both robots are placed on the ground. Based on the above reasons, we investigate how to equip robots with the jumping ability in this chapter.

The design requirements of our robot are summarized in three aspects. First, to make jumping a valid locomotion method, the robot should be able to perform continuous steerable jumping. Towards this goal, the robot should have multiple functions including jumping, self-righting from the landing position, and changing the jumping direction—steering. Second, we aim to accomplish the multiple functions with the minimum number of actuators. Minimum actuator design can reduce the robot's weight, thereby improving the robot's jumping performance. Third, the robot's weight should be small. Specifically, the mass should be less than 30 grams. With a light weight, each jump consumes less energy for the same jumping height, which can increase the jumping times due to the robot's limited energy supply. Moreover, a lightweight robot is less susceptible to the damage from the landing impact.

Initially, we chose good jumping performances as a design priority instead of the minimum number of actuators. After further investigation, however, we switched to minimizing the number of actuators as a priority because it will lead to better jumping performances. Suppose the design for each mechanism in the robot is fixed. Compared with the case of actuating each mechanism with one motor, the robot's weight decreases if a single motor is employed to actuate all of the mechanisms. As a result, the jumping performance improves.

The robot in this chapter—with the prototype and solid model shown in Fig. 2.1—can fulfill the three design goals. First, it can perform continuous steerable jumping with four mechanisms for four functions. In fact, the robot can achieve the motion sequence shown in the upper row of Fig. 2.2. After the robot lands on the ground, it steers to the desired jumping direction. Then it charges the energy and performs the self-righting at the same time. After the energy is fully charged, the robot releases the energy and leaps into the

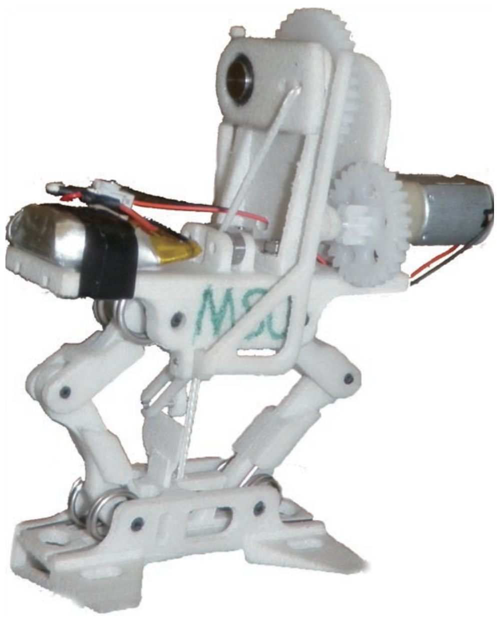

(a)

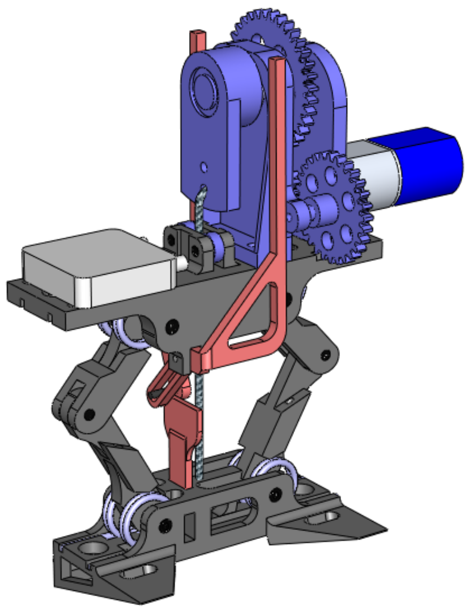
(b)

Figure 2.1 MSU jumper: (a) prototype; (b) solid model.

air. Second, a single motor is employed to achieve the motion sequence in Fig. 2.2. The motor's two direction rotations (clockwise (CW) and counter clockwise (CCW)) actuate different functions as shown in the bottom row of Fig. 2.2. Third, the goal of small weight is accomplished with the robot having a mass 23.5 grams.

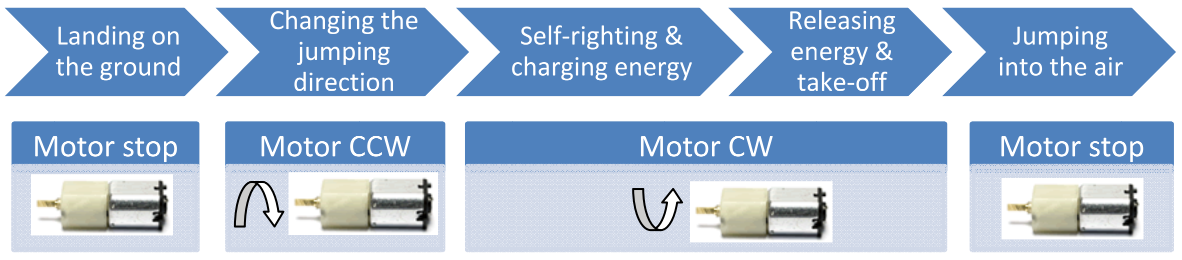
Landing on the ground
Changing the jumping direction
Self-righting & charging energy
Releasing energy & take-off
Jumping into the air
Motor stop
Motor CCW
Motor CW
Motor stop

Figure 2.2 Jumping motion sequence with the corresponding motor rotation directions.

The most relevant research in existing jumping robots is the frogbot [1] for celestial exploration. It can achieve continuous steerable jumping with a single motor. Moreover, the robot has impressive jumping performances: 90cm in height and 200cm in distance. Nevertheless, the major difference between the frogbot and our robot is the different targeting weight ranges. The frogbot has a mass 1300 grams, while our robot is designed to be less than 30 grams. The smaller weight constrains the mechanism design for each function; consequently, the designs for all of the mechanisms are different. We will discuss such differences for each mechanism in detail in section 2.3.

The EPFL jumper V3 is another close research [11]. It can perform continuous steerable jumping with a small mass: 14.33 grams. With the light weight, good jumping performances can still be achieved: 62cm in height and 46cm in distance. The major difference between our robot and the EPFL jumper V3 is that the minimum actuation strategy is pursued in our robot, leading to different designs for each mechanism that will be discussed in section 2.3 as well.

The robot in this chapter is based on our previous design in [88], but it is improved in all of the four mechanisms. For the jumping mechanism, we minimize the required torque to obtain the optimal link lengths. For the energy mechanism, we redesign the gear train to provide enough torque for the energy charge. For the self-righting mechanism, the two legs are relocated close to the gear train to protect them from damage. We also redesign the steering mechanism to increase the steering speed from $2^\circ/s$ to $36^\circ/s$. Besides the above improvements, this chapter also surveys existing jumping robot designs and models the jumping process.

The major contribution of this chapter is the design and development of a new jumping robot satisfying the three design requirements: continuous steerable jumping, minimum actuation, and light weight. Although some robots can fulfill two of the three requirements, no robot can satisfy all of the three requirements to the best of our knowledge.

The rest of this chapter is organized as follows. We discuss the mathematical model of the jumping process in section 2.2. After that, we elaborate the mechanical design for the four mechanisms in section 2.3. Then we perform the optimal design to obtain the best mechanism dimensions in section 2.4. Finally, we present the implementation details, experimental results, and comparison with existing jumping robots in section 2.5.

2.2 Modeling of the Jumping Process

Animals with the jumping ability utilize the same jumping principle. At first, their bodies accelerate upward while their feet remain on the ground. Once the bodies reach some height, they bring the feet to leave the ground, and the animals thrust into the air [31]. With the same principle, a simplified robotic model can be established as shown in Fig. 2.3(a). The robot contains an upper part and a lower part connected by an energy storage medium shown as a spring in the figure. In this section, the theoretical jumping performance will be analyzed based on this model.

With the simplified model, the jumping process can be divided into two steps as shown in Fig. 2.3. The first step, spanning from (a) to (b), starts once the energy stored in the spring is released and ends before the robot leaves the ground. In this step, the upper part first accelerates upward due to the spring force, while the lower part remains stationary. Once the upper part moves to a specific height, a perfect inelastic collision happens between the two parts if the spring constant is large [13]. After the collision, both parts have the same velocity, which is the robot's take-off velocity.

Let the mass for the upper and lower part be m_2 and m_1, respectively. In the ideal case, all the energy E_0 stored in the spring is converted to the kinetic energy of the upper part. Therefore, the speed of the upper part before the inelastic collision is $v_2 = \sqrt{2E_0/m_2}$. Let the take-off velocity be v_0, we have $m_2 v_2 = (m_1 + m_2) v_0$ by the conservation of momentum, and v_0 can be solved as:

$$v_0 = \frac{m_2}{m_1 + m_2} v_2 = \frac{\sqrt{2 m_2 E_0}}{m_1 + m_2} \tag{2.1}$$

Thus, the kinetic energy at take-off is:

$$E = \frac{1}{2}(m_1 + m_2) v_0^2 = \frac{m_2}{m_1 + m_2} E_0 = \frac{1}{r+1} E_0$$

where $r = m_1/m_2$ is the mass ratio between the lower and upper part.

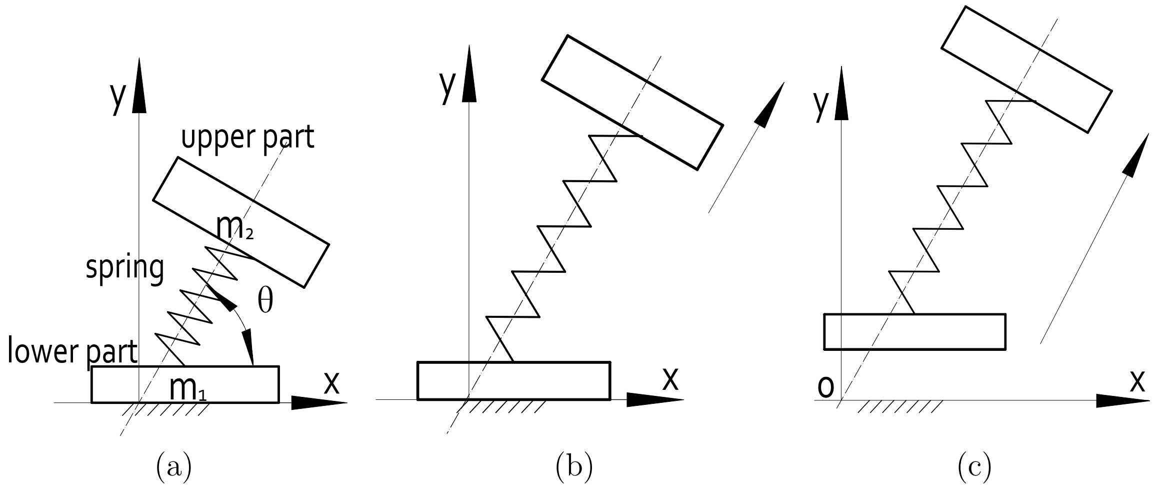

Figure 2.3 Jumping principle for spring based jumping robots.

The second step, spanning from Fig.2.3(b) to 2.3(c), begins when the robot leaves the ground with the take-off speed v_0 and ends when it lands on the ground. The robot in the air will be subject to the gravitational force and the air resistance. If the latter is negligible, then the robot performs a projectile motion. We establish a coordinate frame with the origin at the take-off point, x axis along the horizontal direction, and y axis along the vertical direction, then the robot's trajectory is:

$$x(t) = v_0 t \cos\theta, \quad y(t) = v_0 t \sin\theta - \frac{1}{2} g t^2 \tag{2.2}$$

where θ is the take-off angle and g is the gravitational constant. Based on the trajectory, the jumping height h and distance d can be obtained as:

$$h = \frac{v_0^2}{2g}\sin^2\theta = \frac{E_0 \sin^2\theta}{(1+r)mg} \tag{2.3}$$

$$d = \frac{v_0^2}{g}\sin 2\theta = \frac{2E_0 \sin 2\theta}{(1+r)mg} \tag{2.4}$$

where $m = m_1 + m_2$ is the robot's total mass. From these equations, we see that in order to maximize the jumping height and distance, the mass ratio r and the total mass m should be minimized, while the stored energy E_0 should be maximized. In addition, the jumping height and distance vary with the take-off angle.

If the air resistance is not negligible, then an additional drag force should be considered. The drag force for a rigid body moving with velocity v and frontal area A is: $F_{drag} = C_d \rho A v^2/2$, where C_d is the drag coefficient related to the robot's shape, and ρ is the air density [89]. Therefore, the equation of motion for the robot is:

$$m\ddot{x}(t) + \frac{1}{2}C_d \rho A_x(t)\dot{x}(t)^2 = 0 \tag{2.5}$$

$$m\ddot{y}(t) + \frac{1}{2}C_d \rho A_y(t)\dot{y}(t)^2 + mg = 0 \tag{2.6}$$

where $A_x(t)$ and $A_y(t)$ are the frontal areas perpendicular to the x and y axis, respectively. $A_x(t)$ and $A_y(t)$ vary with time since the robot may change its orientation in the air. The detailed investigation of such a change, however, is quite complicated because it depends on the robot's unknown angular momentum during take-off [90]. For simplicity, we assume $A_x(t) = A_x$ and $A_y(t) = A_y$ are constants, which will not affect the final results much since the drag force is usually very small.

Given the initial condition as $x(0) = 0$, $y(0) = 0$, $\dot{x}(0) = v_0 \cos\theta$, and $\dot{y}(0) = v_0 \sin\theta$, the robot's trajectory is governed by the solution to Eqs. (2.5) and (2.6) as follows [45]:

$$x(t) = \frac{1}{M} \ln(1 + v_0 M t \cos\theta) \tag{2.7}$$

$$y(t) = \frac{1}{N} \ln[\cos(\sqrt{Ng}t) + L \sin(\sqrt{Ng}t)] \tag{2.8}$$

where $M = C_d \rho A_x/(2m)$, $N = C_d \rho A_y/(2m)$, and $L = v_0 \sin\theta \sqrt{N/g}$. The jumping performance with the air resistance can be derived from $x(t)$ and $y(t)$ as [45]:

$$h = \frac{1}{N} \ln(\sqrt{1 + L^2}) \tag{2.9}$$

$$d = \frac{1}{M} \ln[1 + v_0 \cos\theta \frac{M}{\sqrt{Ng}} \arccos(\frac{1 - L^2}{1 + L^2})] \tag{2.10}$$

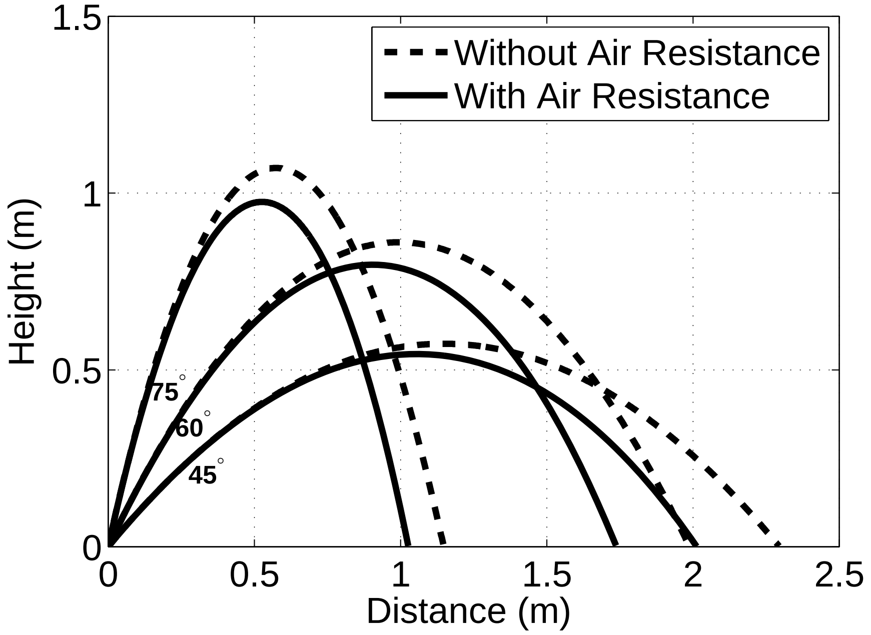

Figure 2.4 Theoretical jumping trajectories for different take-off angles.

Based on the above analysis, theoretical jumping performances without and with the air resistance can be obtained. According to our previous design [88], the following parameters are used for calculation: $E_0 = 0.3$J, $m_1 = 5$g, $m_2 = 15$g, $C_d = 1.58$, $\rho = 1.2$kg/m^3, and $A_x = A_y = 2000$mm^2 for three different take-off angles: 75°, 60°, and 45°. C_d is chosen as the maximum value for the insect experiment in [91] to obtain a conservative result. With the above parameters, the theoretical jumping trajectories for the three take-off angles are obtained and plotted in Fig. 2.4. The angle 75° is chosen as the take-off angle for our robot because the jumping distance and height at this angle are approximately the same. In this case, the robot can overcome obstacles as large as possible without sacrificing the horizontal locomotion ability.

The jumping model presented in this section will also be used to derive the theoretical performance for the robot prototype to compare with the experimental results in section 2.5.

2.3 Mechanical Design and Analysis

Four mechanisms realize the jumping motion sequence in Fig. 2.2. First, the jumping mechanism transforms the stored energy into the robot's kinetic energy for take-off. Second, the energy mechanism charges the energy and releases it instantly. Third, the self-righting mechanism can have the robot stand up after it lands on the ground. Fourth, the steering mechanism changes the robot's jumping direction. The four mechanisms will be described and analyzed in detail in this section.

2.3.1 Jumping Mechanism

For the jumping mechanism, we choose springs as the energy storage medium since (1) they can be implemented with a small weight; (2) they can be obtained easily at a low cost since they are off-the-shelf components; (3) good jumping performances can be achieved [9, 12].

To accomplish jumping with springs, some robots directly strike the ground using springs such as the scout robot [15] and the MIT microbot [17]. This method, however, may lead to the robot's premature take-off from the ground before the energy stored in springs is fully released. Other robots employ spring actuated four or six bar mechanisms to achieve jumping such as the EPFL jumper V1 [9] and the frogbot [1], which can solve the premature take-off problem.

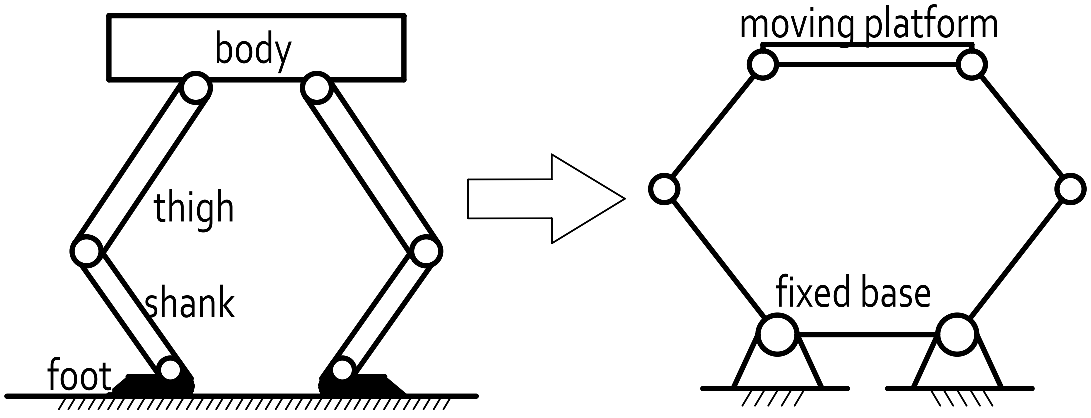

Figure 2.5 Jumping mechanism synthesis.

Various animals with the jumping ability—such as humans, frogs, locusts, or fleas—achieve jumping by extending a pair of legs. The vertical jumping can be modeled as shown on the left of Fig. 2.5, where the leg is divided into three parts: the upper leg (thigh), the lower leg (shank), and the foot [92]. We assume each pair of adjacent parts is connected by a revolute joint since they can rotate relative to each other. Moreover, since both feet stay on the ground before take-off, they can be considered as one part. Therefore, jumping can be emulated by a planar parallel mechanism with two feet as the fixed base, the body as the moving platform, and the two legs as the kinematic chains connecting the platform to the base. This mechanism, shown on the right of Fig. 2.5, is chosen as the jumping mechanism for our robot.

A detailed schematic for the jumping mechanism is shown in Fig. 2.6(a). The mechanism is symmetric with respect to the vertical line OO'. Six revolute joints are placed at A, B, C, D, E, and F. We establish a coordinate frame with X axis along $\overrightarrow{ED}$ and Y axis along $\overrightarrow{OO'}$. Denote the link length as $|AB| = l_1$, $|BC| = |AF| = l_2$, $|CD| = |FE| = l_3$, and $|DE| = l_4$. Denote the vertical distance between AB and ED as y, the angle between $\overrightarrow{BA}$ and $\overrightarrow{AF}$ as α, and the angle between $\overrightarrow{DE}$ and $\overrightarrow{EF}$ as β. Eight torsion springs with a spring constant k are placed at A, B, E, and D—two springs for each place. In this way, the springs can be charged to store energy if a vertical downward force F is applied at point O', and the energy can be released once F is removed.

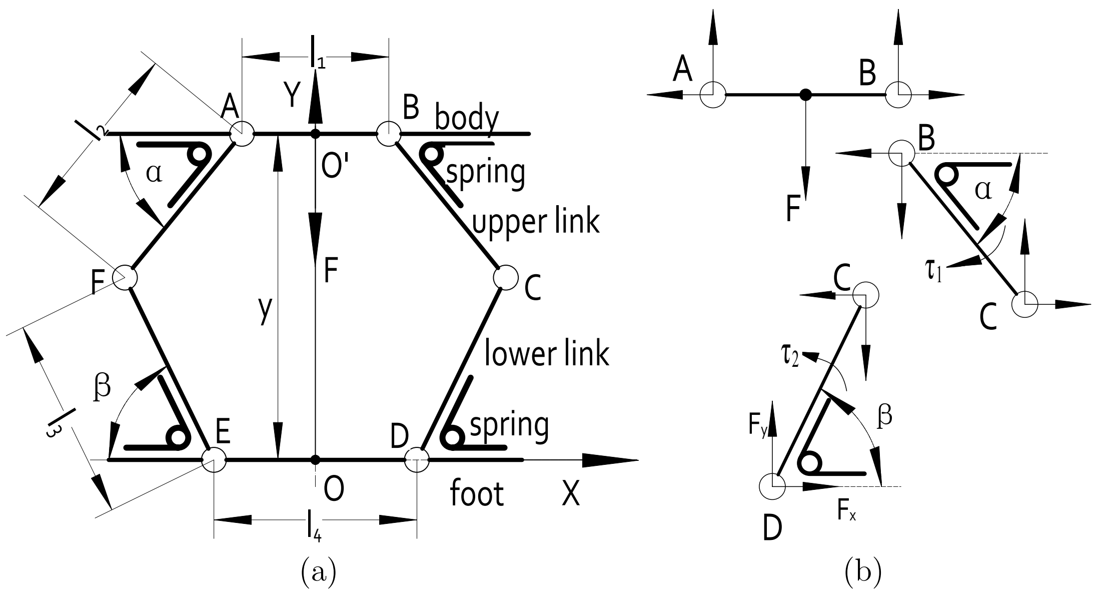

Figure 2.6 Schematic of the jumping mechanism: (a) jumping mechanism; (b) static analysis for the right side part.

The jumping mechanism is different from the one used in the frogbot [1] in two aspects, although both belong to the category of six-bar mechanisms. On one hand, a linear extension spring is employed in the frogbot, while torsion springs are used in our robot. On the other hand, different methods are utilized to make the body only move vertically with respect to the foot. The frogbot employs two pairs of gears at both the body and the foot, while our robot relies on the symmetric placement of torsion springs.

For the mechanism optimization in section 2.4, we analyze the statics for the required force F—which varies with distance y—to charge the energy. Since the mechanism is symmetric with respect to OO', analysis for the right side part is sufficient. Fig. 2.6(b) shows the free body diagrams for links AB, BC, and CD, where all forces are decomposed along the coordinate frame axes. The component forces along the same axis, except F, have the same quantity, although the directions may be opposite. Denote the same quantity as F_x and F_y along the x axis and y axis, respectively. From the figure, the static equations for the three links are:

$$F = 2F_y$$
$$\tau_1 = 2k(\frac{\pi}{2} - \alpha) = F_x l_2 \sin\alpha + F_y l_2 \cos\alpha$$
$$\tau_2 = 2k(\frac{\pi}{2} - \beta) = -F_x l_3 \sin\beta + F_y l_3 \cos\beta$$

where τ_1 and τ_2 are the torques generated by the springs. From the above equations, F can be solved as:

$$F = \frac{2kl_3(\pi - 2\alpha)\sin\beta + 2kl_2(\pi - 2\beta)\sin\alpha}{l_2 l_3 \sin(\alpha + \beta)} \tag{2.11}$$

Note that α and β are functions of y and point C's vertical coordinates y_C. Point C is the intersection point of two circles with centers at $B : (l_1/2,\, y)$ and $D : (l_4/2,\, 0)$; therefore, y_C can be solved as:

$$y_C = \frac{y}{2} - \frac{y(l_2^2 - l_3^2)}{2e} + \frac{l_d}{4e}\sqrt{[(l_2 + l_3)^2 - e][e - (l_2 - l_3)^2]} \tag{2.12}$$

where $e = l_d^2/4 + y^2$ with $l_d = l_4 - l_1$. In fact, there are two intersection points for those two circles, but the point corresponding to the configuration shown in Fig. 2.6(a) is unique. Once y_C is obtained, we can solve α and β as:

$$\alpha = \arcsin \frac{y - y_C}{l_2}, \quad \beta = \arcsin \frac{y_C}{l_3} \tag{2.13}$$

Substituting Eqs. (2.12) and (2.13) into (2.11), we can express F as a function of y by eliminating α, β, and y_C.

To facilitate the optimization in section 2.4, let y_{max} and y_{min} be the maximum and minimum value of y. The largest value for y_{max} is $\sqrt{(l_2 + l_3)^2 - l_d^2/4}$ when AF and FE, BC and CD are collinear. However, we cannot achieve this value because it corresponds to the singular configuration which we should stay clear. Meanwhile, y_{max} should be as large as possible so that the energy stored in the spring can be released thoroughly. To simplify the design process, we empirically let:

$$y_{max} = 0.95\sqrt{(l_2 + l_3)^2 - l_d^2/4} \tag{2.14}$$

2.3.2 Energy Mechanism

For the jumping mechanism, another energy mechanism is required to store energy and release it when necessary. Generally, this can be achieved in two ways. The first approach rotates the motor in one direction to charge energy and in the other direction to release energy. Examples include the scout robot [15] and our second robot [14]. The second approach rotates the motor in a single direction for energy charge and release, leading to a short cycle time. This can be achieved by a slip-gear system [2, 5], an eccentric cam [49, 9],

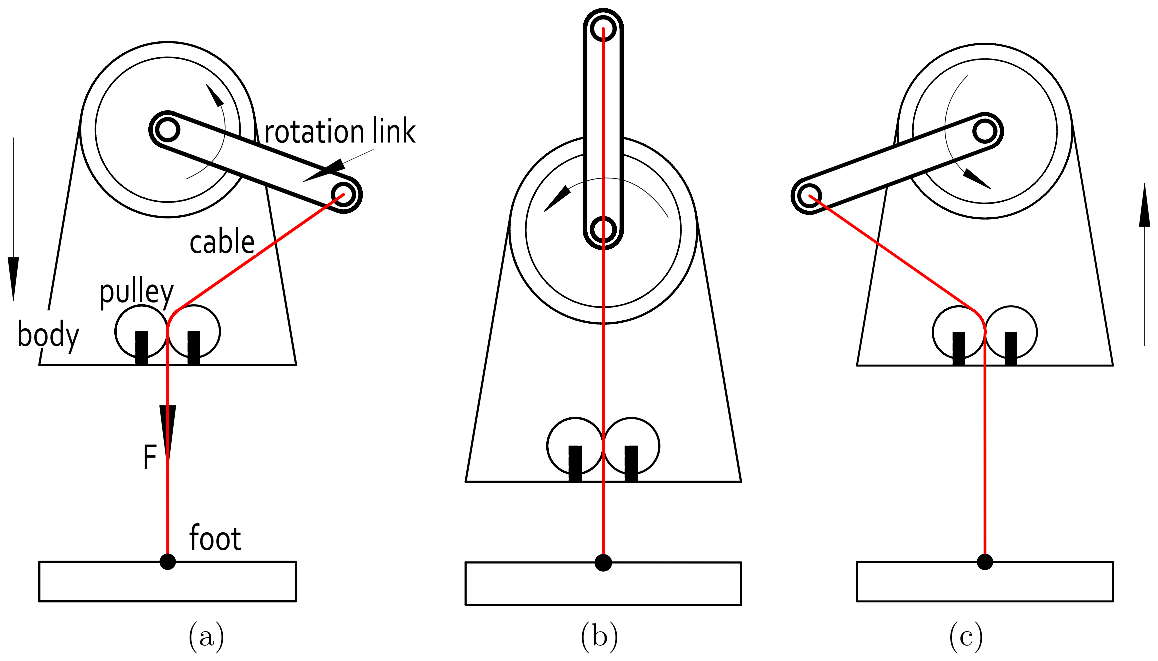

Figure 2.7 Illustration of the energy mechanism: (a) intermediate position during the charge of energy; (b) critical position; (c) intermediate position during the release of energy.

or a variable length crank mechanism [18]. To obtain a short cycle time, we propose a new energy mechanism belonging to the second approach. The key element in this mechanism is a one way bearing.

Fig. 2.7 illustrates the energy mechanism. A rotation link is connected to the output shaft of a speed reduction system via a one way bearing not shown in the figure. Due to the one way bearing, the rotation link can only rotate in the counterclockwise direction. A cable, guided by two pulleys, connects the end of rotation link to the robot's foot. If the rotation link rotates from the bottom vertical initial position, the cable forces the body to move towards the foot (Fig. 2.7(a)). The rotation link's top vertical position (Fig. 2.7(b)) is a critical position since the torque resulted from the cable will switch its direction. Once the link passes this position, the energy is released, and the body accelerates upward (Fig. 2.7(c)). The body and foot in Fig. 2.7 are the same parts in the jumping mechanism shown in Fig. 2.6(a), but the links are not shown for a clear view.

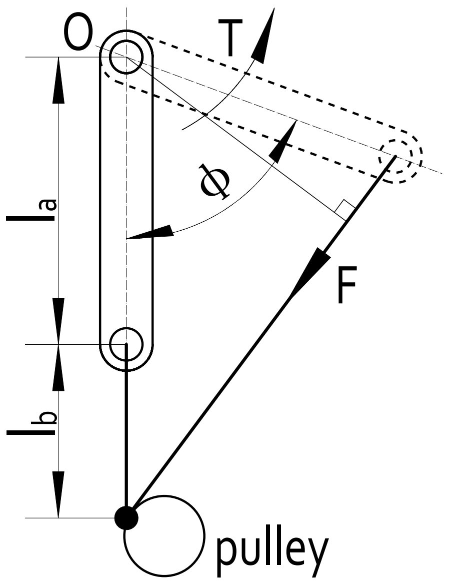

Figure 2.8 Statics for the energy mechanism.

With such a mechanism, the force F in Fig. 2.6(a) can be applied for energy charge. For the optimization in section 2.4, we perform the static analysis for the rotation link to relate this force to the torque generated by the speed reduction system. As shown in Fig. 2.8, l_a is the length of the rotation link, and l_b is the vertical distance from the end of the rotation link to the pulley's center. If the link is rotated to a new position shown as the dashed line in the figure with a rotation angle $\phi \in [0, \pi]$, then the required torque T is equal to the torque generated by F with respect to pivot point O:

$$T = \frac{F l_a (l_a + l_b) \sin\phi}{\sqrt{l_a^2 + (l_a + l_b)^2 - 2 l_a (l_a + l_b) \cos\phi}} \tag{2.15}$$

For the optimization in section 2.4, we also represent the vertical distance y between the body and the foot shown in Fig. 2.6(a) as:

$$y = y_{max} - \left(\sqrt{l_a^2 + (l_a + l_b)^2 - 2 l_a (l_a + l_b) \cos\phi} - l_b\right) \tag{2.16}$$

2.3.3 Self-righting Mechanism

With the jumping and energy mechanisms, the robot can jump if it initially stands on the ground with its foot. This case, however, seldom happens due to the landing impact. Therefore, a self-righting mechanism is needed to make the robot recover from possible landing postures.

In general, there are two methods for self-righting. The first one is the passive recovery based on the center of gravity (CoG). The robot will stand up if the CoG is sufficiently close to the foot. Examples include the EPFL jumper V3 [11], the Jollbot [18], and our first robot [13]. The second method, widely used in animals, is the active recovery with actuated parts. For instance, the beetles employ their legs for self-righting [93], while the turtles utilize the head because of their short legs [94]. The active recovery is implemented in the frogbot [1] and the new surveillance robot [3]. For our robot, we adopt the active self-righting to achieve a small robot size.

Fig. 2.9 illustrates the working principle for our self-righting mechanism. The robot has a rectangular shape with two surfaces significantly larger than the other four. As a result, the robot will contact the ground with one of these two large surfaces most of the time after landing. Without loss of generality, we assume a landing posture as shown in Fig. 2.9(a). Two self-righting legs on the body are initially parallel to the two large surfaces. Once actuated, they can rotate simultaneously in opposite directions. After a certain amount of rotation, the robot can stand up for the next jump. The final position when both legs are fully extended is shown in Fig 2.9(b).

The detailed mechanism is shown in Fig. 2.10, where the whole mechanism is shown on the left and a partial enlargement is shown on the right. Note that the foot is not shown for

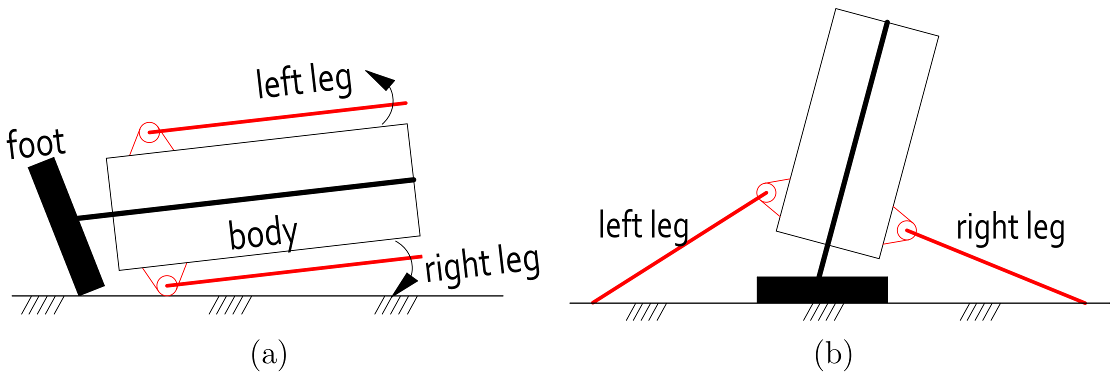

Figure 2.9 Illustration of the self-righting mechanism: (a) initial position after the robot lands on the ground; (b) final position when the robot stands up.

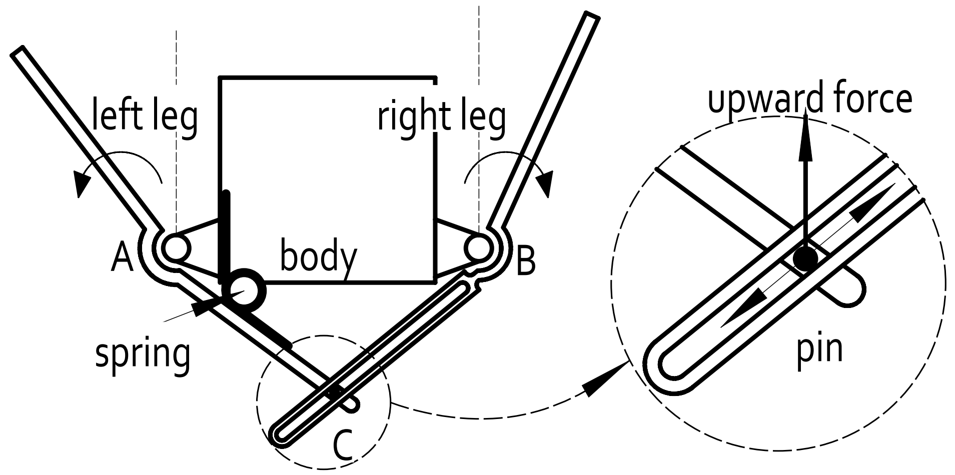

Figure 2.10 Details of the self-righting mechanism.

a clear view. A revolute joint connects each leg to the body. A pin (shown as a solid circle in the enlargement) fixed to the left leg can slide along a groove in the right leg. In this way, if we apply an upward force on the pin, both legs will rotate, but in opposite directions. A small torsion spring—with one end fixed to the body and the other end attached to the left leg—will make both legs return to their original positions if the upward force is removed.

We apply the upward force in Fig. 2.10 using the same actuator for energy charge. In fact, the body moves towards the foot during the energy charge process. With this motion, if a protrusion is attached to the foot and beneath the pin, the upward force will be generated once the protrusion contacts the pin. If the energy is released, the body will move away from the foot; consequently, the upward force is removed when the body is a certain distance away from the foot.

From the above discussions, the energy charge and the self-righting can be performed simultaneously, leading to a short cycle time. Furthermore, all the motion can be accomplished with the motor's one directional rotation. Note that the frogbot also employs a single motor for the energy charge and the self-righting. The self-righting process, however, is divided to two phases due to the shape of the robot [1].

2.3.4 Steering Mechanism

The final mechanism to realize the motion sequence in Fig. 2.2 is the steering mechanism, which can change the jumping direction. A review of steering methods for jumping robot can be found in [11]. Based on our robot's rectangular shape, we propose a steering method without extra actuators.

The steering mechanism is illustrated in Fig. 2.11. Two steering gears are placed symmetrically about the motor gear. Both gears are a certain distance away from the robot's centerline. Since the robot contacts the ground with one of its two large surfaces after landing, one of the two steering gears will touch the ground. Therefore, if the motor rotates, the robot will change its heading direction.

The same motor for the other three mechanisms actuates the steering mechanism. In fact, the steering mechanism is driven by the motor's one directional rotation, while the other three mechanisms are actuated by the other directional rotation. One steering gear is also used in the speed reduction system for energy charge. If the motor rotates in one direction, this gear is used for energy charge. If the motor rotates in the other direction, the rotation link in Fig. 2.7 will not rotate due to the one-way bearing. In this case, this gear

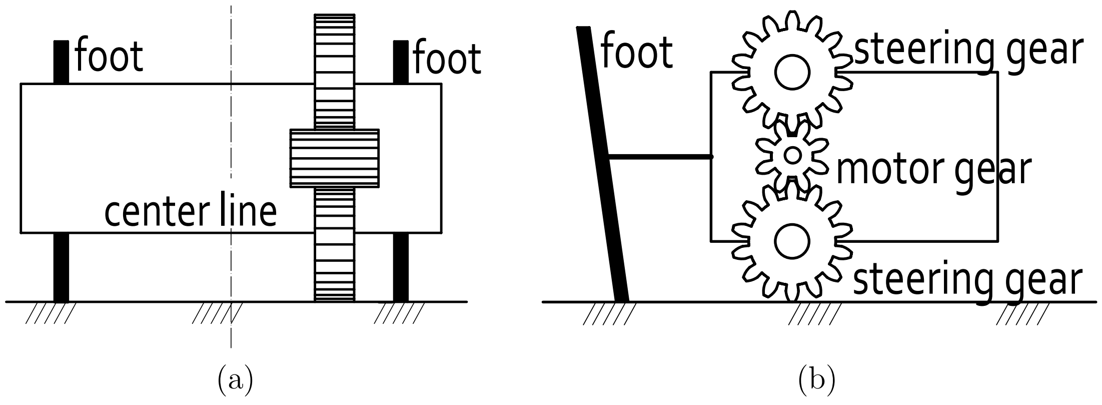

Figure 2.11 Illustration of the steering mechanism: (a) front view; (b) side view.

can steer the robot.

The steering mechanism is improved from our previous design in [88], where a single large gear at the end of speed reduction system is the steering gear. Due to its large diameter, the gear can touch the ground no matter which large surface of the robot contacts the ground. This method, although simpler, has a slow steering speed due to the large gear's small angular velocity. The new design increases the speed because the two steering gears are next to the motor gear, resulting in a large angular velocity.

2.4 Design Optimization

Based on the analysis in section 2.3, the mechanism dimensions can be determined through optimization. In this section, we optimize the jumping mechanism together with the energy mechanism to obtain the smallest peak torque for energy charge. After that, the dimensions of the self-righting mechanism are derived based on practical requirements. The steering mechanism is not discussed because it is determined by the energy mechanism.

Table 2.1 List of parameters for optimization

l_2	length of the upper link (Fig. 2.6(a))
l_3	length of the lower link (Fig. 2.6(a))
l_d	difference between the body link l_1 and the foot link l_4
l_a	length of the rotation link (Fig. 2.8)
l_b	vertical distance from the rotation link to the pulley (Fig. 2.8)
y	vertical distance between the body and the foot (Fig. 2.6(a))
α	angle between the body link and the upper link (Fig. 2.6(a))
β	angle between the foot link and the lower link (Fig. 2.6(a))
ϕ	angle between the rotation link and the vertical line (Fig. 2.8)
E_0	total energy stored in the spring
k	torsion spring constant

2.4.1 Jumping Mechanism and Energy Mechanism

With the jumping and energy mechanisms, if the same energy can be charged with a small peak value of torque T generated by the speed reduction system, then the weight and size for the robot can be reduced. Therefore, optimization is needed to minimize the peak value of T.

In the following, we perform the optimal design in four steps: identifying the optimization variables, formulating the objective function, obtaining the constraints, and solving the constrained optimization problem. For easy reference, the parameters used in the optimization are listed in Table 2.1.

To identify the optimization variables, we substitute the force equation (2.11) into the torque equation (2.15):

$$T = \frac{2kl_a(l_a + l_b)\sin\phi[l_3(\pi - 2\alpha)\sin\beta + l_2(\pi - 2\beta)\sin\alpha]}{l_2 l_3 \sin(\alpha+\beta)\sqrt{l_a^2 + (l_a + l_b)^2 - 2l_a(l_a + l_b)\cos\phi}} \tag{2.17}$$

from which there are eight parameters: k, l_a, l_b, α, β, l_2, l_3, and ϕ. Since α and β can be written as a function of y, l_2, l_3, and l_d by substituting Eq. (2.12) into Eq. (2.13), the true parameters are k, l_a, l_b, y, l_2, l_3, l_d, and ϕ.

Among the eight parameters, the variables will be only l_b, l_2, l_3, l_d, and ϕ because k, l_a, and y are either constants or dependents on the variables. First, according to our previous design [88], the torsion springs are chosen to have a constant $k = 58.98$Nmm/rad. Second, l_a can be obtained from l_2, l_3, and l_d. In fact, from the geometrical relation of the energy mechanism, we have $l_a = (y_{max} - y_{min})/2$. If l_2, l_3, and l_d are given, y_{max} can be derived using Eq. (2.14). With y_{max} known, y_{min} can also be determined to ensure a desired initial energy E_0 can be stored in the springs. Third, once y_{max} and l_a are known, y can also be derived through Eq. (2.16) based on l_b and ϕ. From the above arguments, T is only a function of l_b, l_2, l_3, l_d, and ϕ, and we denote it as $T(l_b, l_2, l_3, l_d, \phi)$. The optimization variables are only l_b, l_2, l_3, and l_d because ϕ will run from 0 to π during each energy charge cycle.

The initial energy E_0 is determined based on the simulations in section 2.2. To achieve one meter jumping height with a 75° take-off angle, the initial energy should be 0.3J. But to leave enough margin, we let $E_0 = 0.4$J. In addition, the zero energy configuration for the jumping mechanism corresponds to the configuration when $y = y_{max}$. The α and β angles for such a configuration depend on the link lengths and can be derived using Eqs. (2.12) and (2.13).

Having identified the optimization variables, we formulate the objective function. Given l_b, l_2, l_3, and l_d, a torque curve as ϕ running from 0 to π can be plotted. The goal is to find the optimal l_b, l_2, l_3, and l_d such that the peak torque in the curve is the minimum among all possible curves. Therefore, the objective function is the peak torque in the curve:

$$g(l_b, l_2, l_3, l_d) = \max_{\phi \in [0, \pi]} T(l_b, l_2, l_3, l_d, \phi) \tag{2.18}$$

The next step is to obtain the constraints for the optimization variables. The lengths of l_2 and l_3 should be large enough to hold the torsion springs. But they cannot be too large due to the size limit of the robot. Therefore, with practical considerations, assume 15mm $\leq l_2, l_3 \leq$ 20mm. With similar implementation reasons, we can have other linear constraints for l_b and l_d, and the optimization can be formulated as:

$$\begin{aligned} \text{minimize} \quad & g(l_b, l_d, l_2, l_3) \\ \text{subject to} \quad & 7 \leq l_b \leq 12, \, -5 \leq l_d \leq 5, \\ & 15 \leq l_2 \leq 20, \, 15 \leq l_3 \leq 20 \end{aligned} \tag{2.19}$$

where the omitted length unit is millimeter.

To solve the constrained optimization problem, we apply the numerical method because the analytical expression for $g(l_b, l_d, l_2, l_3)$ cannot be obtained. The optimization is realized by a dense discretization of ϕ and value evaluations at the resulting points [95]. The constrained nonlinear multivariable function in the Optimization Toolbox of Matlab is employed to find the optimal value. Since the method can only obtain the local minimum, we choose various random initial points to run the optimization. The smallest objective function among these local minima is the optimal value, and the optimal dimensions are l_b = 7mm, l_d = 1.2mm, l_2 = 15mm, and l_3 = 20mm. The other parameters can be calculated accordingly: y_{max} = 33.3mm, y_{min} = 11.7mm, and l_a = 10.8mm. To avoid interference between the two revolute joints at the foot, let l_1 = 18mm, then $l_4 = l_1 + l_d$ = 19.2mm.

To investigate how the variables affect the objective function, we plot the graphs showing the objective function and the variables. Since it is impossible to include the four variables into one graph, we divide them into two groups: l_b and l_d, l_2 and l_3. Fig. 2.12(a) shows how

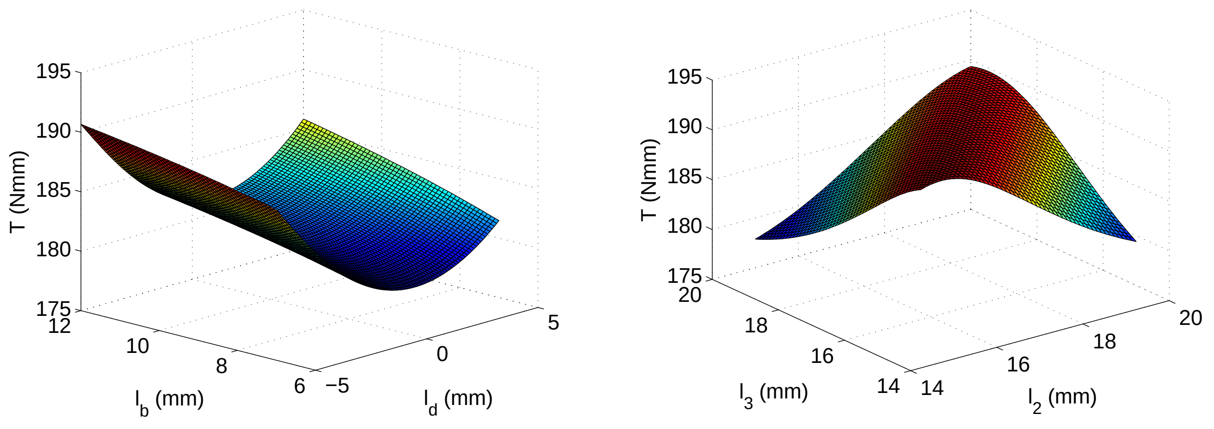

Figure 2.12 Objective function varies with optimization variables: (a) variation of $g(l_b,\, l_d,\, l_2,\, l_3)$ with fixed l_2 and l_3; (b) variation of $g(l_b,\, l_d,\, l_2,\, l_3)$ with fixed l_b and l_d.

the objective function changes with respect to l_b and l_d by fixing l_2 and l_3 to the optimal value. As seen in the figure, the minimum value happens when l_b is the smallest and l_d is in the middle part. Fig. 2.12(b) shows how the objective function varies with respect to l_2 and l_3 by fixing l_b and l_d to the optimal value. In this figure, the minimum value happens at the left corner. From these two figures, we see that the optimal dimensions obtained from the optimization are correct.

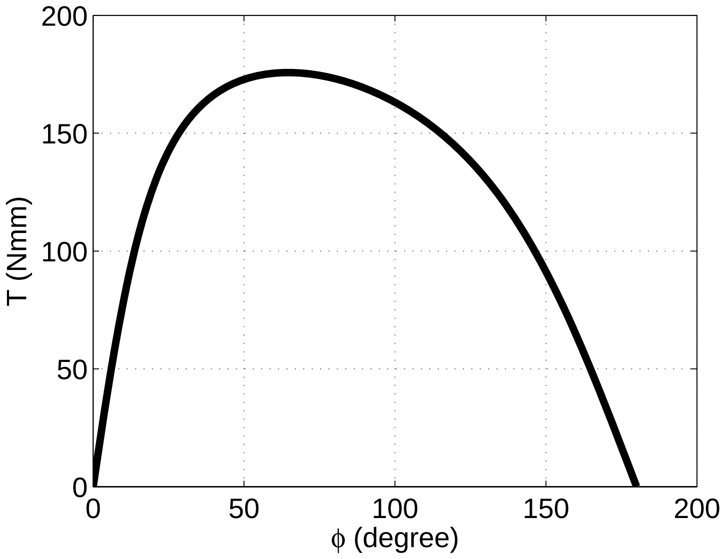

Figure 2.13 Torque profile with the optimal dimensions.

With the optimal design, we can obtain the torque curve with respect to the angle ϕ as shown in Fig. 2.13. From the figure, the torque profile is nonlinear with the peak value happening at $\phi = 66^\circ$. Furthermore, the torque is zero when the energy is about to be released ($\phi = 180^\circ$), which means the release of the energy requires the minimal torque. With the small torque during the release, the mechanism can reduce the probability of premature take-off [1]; consequently, it is highly possible that all the energy stored in the spring can be converted to the kinetic energy for take-off.

2.4.2 Self-righting Mechanism

The dimensions for the self-righting mechanism are critical for successful recovery from possible landing postures. The design variables include the leg length and the range of leg rotation angle. The initial and final positions for both recovery legs are shown in Fig. 2.14(a). The initial positions, AM and BN, are parallel to the body, and the final positions, AM' and BN', contact the ground with leg ends M' and N'. The ranges of leg rotation angle are denoted by μ and ν for the left and right leg, respectively. O is the middle point for AB. Moreover, we have $AB \perp OD$ and $\angle ODN' = \theta = 75^\circ$, which is the robot take-off angle. The relation between the leg length and the range of leg rotation angle can be obtained using the law of sines in $\triangle AM'E$ and $\triangle BN'F$:

$$\frac{|AM'|}{\sin(\pi - \theta)} = \frac{|OD| + |AO| \tan(\pi/2 - \theta)}{\sin(\mu - \pi + \theta)} \tag{2.20}$$

$$\frac{|BN'|}{\sin\theta} = \frac{|OD| - |BO| \tan(\pi/2 - \theta)}{\sin(\nu - \theta)} \tag{2.21}$$

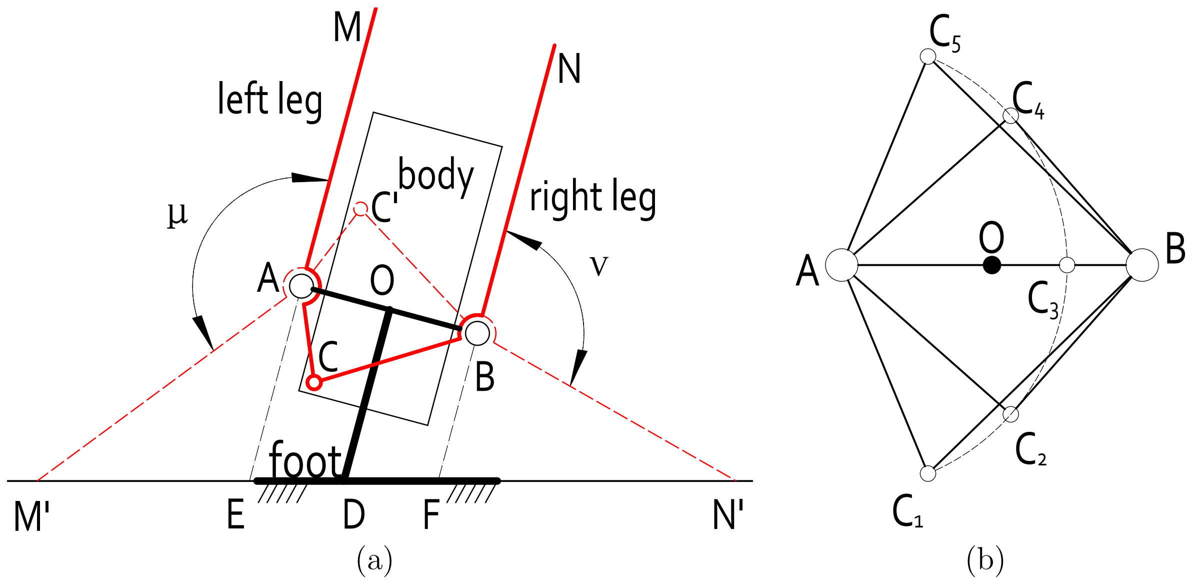

Figure 2.14 Dimension design of the self-righting mechanism: (a) mechanism with initial and final positions for both self-righting legs; (b) simplification of the mechanism to determine the length for link AC.

From Eqs. (2.20) and (2.21), if μ or ν is large, then the leg length AM' or BN' can be small. To simplify the design, we fix $\mu = 135^\circ$ and $\nu = 105^\circ$ to let $\mu - \angle ODM' = \nu - \angle ODN' = 30^\circ$. With μ and ν fixed, $|AM'|$ and $|BN'|$ can be solved from Eqs. (2.20) and (2.21) given $|AO| = |BO|$ and $|OD|$, which are determined from the implementation.

The next step is to design the length of AC shown in Fig. 2.14(a) to achieve the desired angle ranges. Without the body, the foot, the part AM in the left leg, and the part BN in the right leg, the mechanism can be simplified as shown in Fig. 2.14(b). In the figure, C_1 to C_5 are different locations for the end point C of link AC. C_1 and C_5, symmetric with respect to AB, are the limit position for link AC; therefore, $\angle C_1AC_5 = \mu = 135^\circ$. C_2 and C_4, symmetric with respect to AB as well, are the tangent points from point B to the circle formed by link AC. Since BC_2 and BC_4 are the limit positions for link BC, $\angle C_2BC_4 = \nu = 105^\circ$. From right-angled $\triangle ABC_4$, we have $|AC| = |AB| \sin(\nu/2)$. The parameters for the right leg can also be derived accordingly.

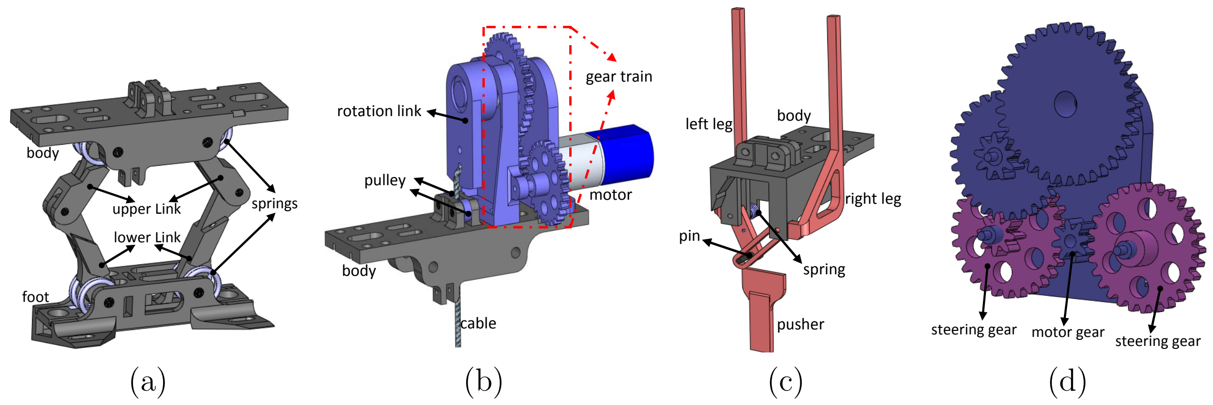

Figure 2.15 Solid model for each mechanism (a) jumping mechanism (principle shown in Fig. 2.6(a)); (b) energy mechanism (principle shown in Fig. 2.7); (c) self-righting mechanism (principle shown in Fig. 2.10); (d) steering mechanism (principle shown in Fig. 2.11).

2.5 Fabrication and Experimental Results

2.5.1 Fabrication and Development

The solid model for the robot is shown in Fig. 2.1(b), and the individual mechanisms are shown from Fig. 2.15(a) to Fig. 2.15(d). Some parts appear in multiple figures because they are used in different mechanisms. We elaborate the implementation for each mechanism in this sub section.

For the jumping mechanism shown in Fig. 2.15(a), both the left-hand (9287K77 from McMaster-Carr) and the right-hand (9287K26 from McMaster-Carr) torsion springs are required. We use a pin-hole structure to implement the revolute joints. The torsion springs are held in place by the pins of the revolute joints. The bottom of the foot is designed with a tilted angle 15° to provide the 75° take-off angle.

The major part of the energy mechanism, shown in Fig. 2.15(b), is the motor actuated gear train or speed reduction system. The gear train has three stages consisting of a motor gear (8 teeth), a compound gear (28/8 teeth), another compound gear (28/9 teeth), and a spur gear (35 teeth). Therefore, the total speed reduction ratio is 47.6. Based on this ratio and the required peak torque (178Nmm) in Fig. 2.13, the motor (GH810136V3 from Gizmoszone) with a stall torque 8Nmm is chosen. For this motor, a sufficient margin has been left to overcome the friction in the gear train. The one-way bearing (kit8637 from VXB bearings) cannot be shown in Fig. 2.15(b) because it is inside the rotation link.

Fig. 2.15(c) shows a section view of the self-righting mechanism. The revolute joints connecting the two legs to the body are achieved by the pin-hole structure as well. The pusher attached to the foot—not shown in Fig. 2.15(c)—can provide the upward force in Fig. 2.10. The small torsion spring (9287K12 from McMaster-Carr) is held in placed by the pin in the left revolute joint.

The steering mechanism, shown in Fig. 2.15(d), comes from the energy mechanism. All of the gears in the gear train of Fig. 2.15(b) are shown in Fig. 2.15(d). Only the right steering gear does not belong to the energy mechanism, and the left steering gear is part of the gear train to charge energy.

We obtain the robot parts from three sources. First, some parts are off-the-shelf components such as springs and bearings. Second, most of the other parts are fabricated using the selective laser sintering with the DuraForm HST material. It has a density only 1.20g/cm^3, yet it can be used for functional prototypes. Third, the aluminum shafts in the gear train are manufactured using traditional machining methods.

The robot is powered by a FullRiver 50mAh LiPo battery with an average 3.7V voltage output. Since the energy mechanism is placed on the right side of the body, the battery—shown in Fig. 2.1(b)—is placed on the left side to balance the robot's weight.

Depending on the obstacle size the robot needs to overcome, we can adjust the robot's parameters in two ways to achieve different jumping performances. First, the take-off angle can be modified by using feet with different tilted angles. In this way, the ratio between the jumping height and distance varies according to Eqs. (2.3) and (2.4). Second, the torsion springs in the jumping mechanism can be replaced by those with smaller constants. In this case, the initial stored energy in the robot can be changed, leading to different jumping performances.

For the robot, the mass and the initial stored energy are needed to obtain the theoretical performances. The lower part of the robot contains the components below the revolute joint connecting the lower link to the upper link, while the upper part includes all of the other components above that joint. The mass for each part is $m_1 = 5.4g$ and $m_2 = 18.1g$. The initial energy E_0 is designed to be 0.4J, but the true energy cannot be this much because the minimum distance y_{min} for y cannot be the designed value due to the cable's elasticity. Therefore, the true y_{min} is measured to calculate the energy stored in the spring. In fact, $y_{min} = 14$mm and the resulting $E_0 = 0.34$J.

2.5.2 Experimental Results

Jumping experiments are conducted to determine the jumping performances. To eliminate the slippage during the robot's take-off, we place the robot on a high coefficient of friction surface (fine grained sand paper with a grit designation 320). To obtain the performances, we also place the robot in front of a board with small holes. The distance between neighboring holes, either horizontal or vertical, is one inch (2.54cm). When the robot jumps, a video is recorded by a Casio Exilim EX-FH25 high speed camera with a frame rate 240 frame-per-second. After that, the jumping height is obtained off-line from the video by comparing the robot's highest position with the vertical holes, while the jumping distance is obtained by comparing the landing position with the horizontal holes.

Five jumps are carried out to obtain the average jumping performance. The average jumping trajectory for these five jumps is plotted with the solid line in Fig. 2.16. Note that the robot jumps from the right to the left, and only half of the trajectory is shown due to the symmetry of the trajectory. The average performance is listed in Table 2.2, where the robot can jump 87.2cm in height and 89.8cm in distance. The standard deviations for these jumps are 2.2cm and 4.0cm for the height and distance, respectively. The take-off velocity can also be obtained as 4.3m/s. Therefore, the jumping efficiency—defined as the ratio between the kinetic energy before robot's take-off E and the initial stored energy E_0—is 63.0%.

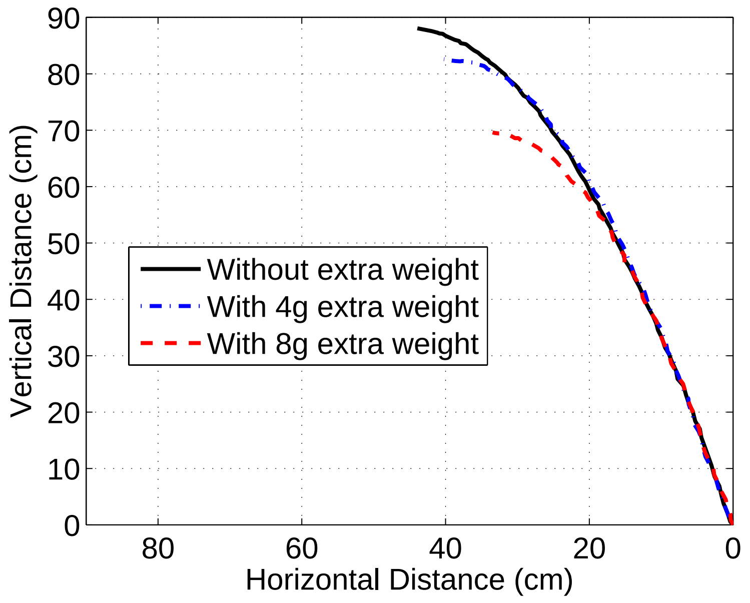

Figure 2.16 Jumping experimental results: average trajectories for three sets of experiments.

The sensor network application requires the robot to be able to carry payloads for extra sensors. Therefore, experiments are conducted to investigate the jumping performance with an extra weight. The extra weight is placed on the opposite side of gear train to balance the robot's weight. The average performances for five jumps are listed in Table 2.2 as well, and the average trajectories are also shown in Fig. 2.16. For an extra four gram mass, the average jumping height and distance are 82.1cm and 80.6cm, respectively. If an extra eight gram mass is added, the average jumping height and distance become 69.5cm and 67.8cm,

Table 2.2 Experimental and Theoretical Jumping Performances

Extra Weight	Experimental Height (cm)	Experimental Distance (cm)	Estimated Height (cm)	Estimated Distance (cm)
$0g$	87.2 ± 2.2	89.8 ± 4.0	97.9	103.4
$4g$	82.1 ± 1.2	80.6 ± 1.6	88.9	94.2
$8g$	69.5 ± 2.2	67.8 ± 2.8	81.1	86.1

respectively. The small decreases in both the jumping height and distance are not large indicates the robot can carry some payloads without degrading its performance significantly.

The theoretical performances with the air resistance are also listed in Table 2.2. From the table, the experimental results are worse than the theoretical calculations. The major reason for such a discrepancy is the friction in the jumping mechanism. In particular, the friction exists in all of the revolute joints since they are built using the pin-hole structure. Due to the friction, only part of the stored energy is converted to the kinetic energy for take-off. Additionally, some energy is also transformed to the robot's rotation energy in the air. This energy loss, however, is negligible because of the robot's small moment of inertia and angular velocity.

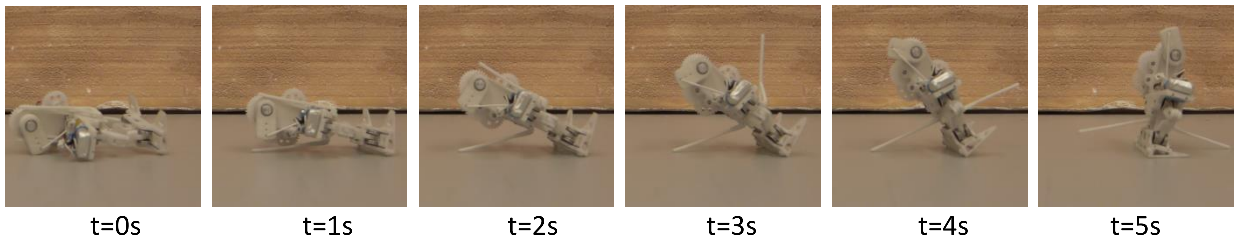

Figure 2.17 Self-righting experimental result: six individual frames extracted from a self-righting video.

Table 2.3 Comparison with existing robots with the jumping ability

Robot Name	Mass [g]	Size [cm]	Charge time [s]	Jump height [cm]	Jump distance [cm]	Normalized jump height [cm]	Height per mass and size [10·cm·/(g·cm)]	Self-right	Steer	Onboard energy	Actuator
Flea robot [20]	1.1	2	15	64	70	68.8	312.73	no	no	no	3 SMA
Frogbot [1]	1300	15	30	90	200	117.8	0.06	yes	yes	yes	1 motor
Surveillance robot [3]	150	12.2	60	105	60	107.1	0.59	yes	no	yes	2 motors
Grillo III [7]	22	5	8	10	20	12.5	1.14	no	no	yes	1 motor
EPFL jumper V1 [9]	6.98	5	3.5	138	79	140.8	40.34	no	no	yes	1 motor
EPFL jumper V2 [10]	9.8	12	3.5	76	81	81.4	6.92	yes	no	yes	1 motor
EPFL jumper V3 [11]	14.33	18	3.5	62	46	64.1	2.49	yes	yes	yes	2 motors
Multimodal robot [12]	72	×	×	170	0	170	×	no	no	yes	×
Compact jumping robot [16]	18	11	0.3	15	95	52.6	2.66	no	no	no	2 motors
MIT microbot [17]	46	10	×	38	0	38	0.83	no	no	no	1 DEA
Jollbot [18]	465	30	1.44	18.4	0	18.4	0.01	yes	yes	yes	2 motors
Deformable robot [19]	5	9	45	18	0	18	4	yes	no	no	4 SMA
MSU jumper	**23.5**	**6.5**	**10**	**87.2**	**89.8**	**93.0**	**6.09**	**yes**	**yes**	**yes**	**1 motor**

× Data are not available from the reference

The self-righting experiments are also carried out. One of the results is shown in Fig. 2.17, where six frames from a video recording the self-righting process are presented. The robot needs five seconds for self-righting as seen from the time under each picture. Since the self-righting process is performed simultaneously with the energy charge process, the cycle time does not increase.

The steering experiments are performed on the ground as well. Four frames from a video are shown in Fig. 2.18. In this experiment, the robot changes its direction in the counterclockwise direction. From the video, the robot can rotate 360° in about 10 seconds; therefore, the rotation speed is about $36°/s$, which is much faster than the $2°/s$ for our previous design [88].

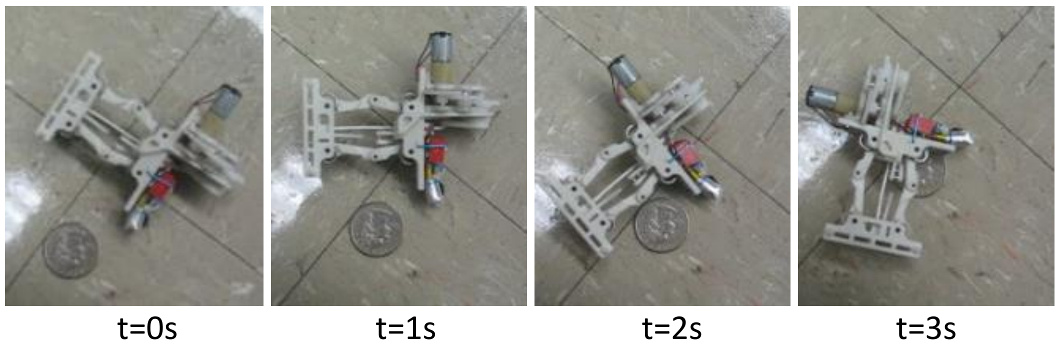

Figure 2.18 Steering experimental result: four individual frames extracted from a steering video.

2.5.3 Comparison with Other Robots

Comparisons with other jumping robots are listed in Table 2.3. Since robots with different energy storage methods have different characteristics, only the robots based on traditional and customized springs are listed. Furthermore, some robots are not included because they use wheels as the primary locomotion method such as the mini-whegs [5], the stair climbing robot [8], and the scout robot [15].

To make the comparison fair, appropriate indices should be chosen. The mass, size, jumping height, and jumping distance are usually selected for comparison [18]. In Table 2.3, these four indices are listed in column two, three, five, and six, respectively. Note that the size is the maximum dimension among the length, width, and height. For spring based robots, the charge time—fourth column in the table—is also an important index since more energy can be stored with a longer charge time provided the other conditions are the same. Since the jumping height and distance vary with take-off angles, the normalized jumping height with a 90° take-off angle is calculated from the jumping height and distance using Eqs. (2.3) and (2.4). This index is the seventh column in the table. To compare the obstacle height the robot can overcome given its size and weight [47], the height per mass and size is listed in the eighth column. It is obtained from dividing the normalized jumping height by the mass and the size. The subsequent three columns indicate whether the robot has self-righting, steering, and onboard energy, respectively. Finally, the type and the number of actuators are listed in the last column.

Compared with the robots in Table 2.3, the MSU jumper has a good overall performance among those robots with continuous steerable jumping ability. The overall performance is indicated by the height per mass and size index (the eighth column in Table 2.3). Besides the good overall jumping performance, the MSU jumper employs a single motor for continuous steerable jumping. Except the frogbot and those robots with different actuation methods, all of the other robots need extra motor to achieve either self-righting or steering as indicated in the last column of Table 2.3.

Compared with the MSU jumper, the other jumping robots have their own merits as well. First, the robots with wheels can run faster if no obstacle exists [5, 15]. Second, the robots with a sphere structure for self-righting can roll passively on the ground. Moreover, the enclosed sphere protects the robot from damage [10, 11, 18]. Third, some robots have the embedded sensing, control, and communication system [1, 3]. With such a system, the control, navigation, and motion planning can be investigated for the jumping locomotion [96].

2.6 Conclusions

To facilitate the locomotion for mobile sensors in environments with obstacles, this chapter presents the mechanical design of a miniature steerable jumping robot. Different from existing designs, the robot can satisfy three design requirements: continuous steerable jumping, minimum actuation, and light weight. Moreover, optimal design is performed to obtain the best mechanism dimensions. Experimental results show that the robot has a good overall jumping performance compared with existing jumping robots. The jumping robot in this chapter can be potentially used in mobile sensor networks for various applications. Furthermore, the design method presented in this chapter may also be applied to other miniature robot designs.

Chapter 3

MSU Tailbot: A Biologically Inspired Tailed Robot

3.1 Introduction

Many animals use multiple locomotion methods to travel in natural environments under different situations [31]. For example, a lizard can rapidly jump up to seize small insects or escape from predators; it can also walk slowly in other non-emergent situations. Further, once leaping into the air, it can use the tail to control its body angle for safe landing [60]. The various locomotion abilities found in animals inspire many novel robot designs with multi-modal locomotion [97].

Robots with multi-modal locomotion abilities are required as the deployment of robots in natural environments becoming more widespread. Consider the scenario of using many miniature robots to monitor an environment with obstacles. The energy efficient way is to employ wheeled locomotion if there is no obstacle. Encountering a large obstacle, the robot can jump to cross it. Moreover, to protect the robot from damage during the landing, it is desirable that the robot can perform aerial maneuvering to control its body angle to land on the ground with a safe posture.

In this chapter, we present the design, control, and experimentation of a robot that can accomplish the above multi-modal locomotion. The detailed motion cycle for the robot is

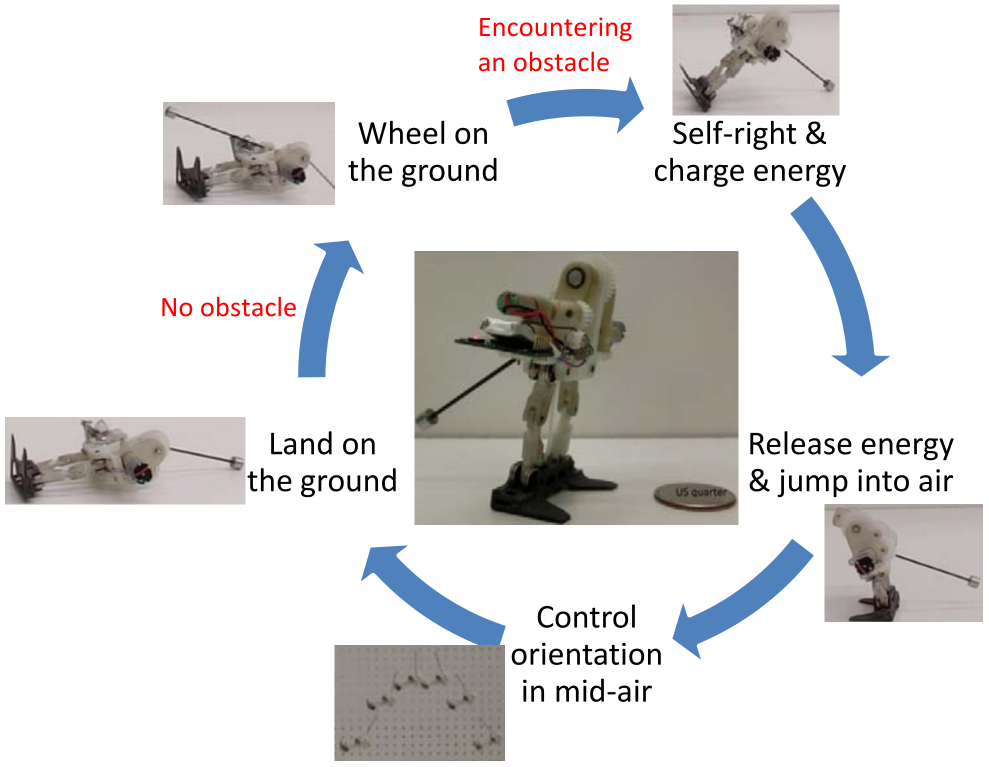
Encountering an obstacle
Self-right & charge energy
Wheel on the ground
No obstacle
Land on the ground
Release energy & jump into air
Control orientation in mid-air
US quarter

Figure 3.1 The robot motion cycle with the robot prototype in the center.

shown in Fig. 3.1 with the robot prototype in the center of the figure. The robot can jump up to 80 cm with a mass of 26.5 grams and a maximum body size 7.5 cm. Moreover, the robot has onboard energy, sensing and control, and wireless communication abilities, which make it an ideal mobile sensor platform for wireless sensor networks. To the best of our knowledge, this is the first miniature, lightweight, and tetherless robot that has all of the wheeling, jumping, and aerial maneuvering abilities.

Two main challenges exist for developing such a robotic platform. First, it is difficult to perform real time onboard control for aerial maneuvering since the jumping time only lasts for less than one second and the robot needs to perform real time sensing, computation, and control. Second, it is challenging to design a robot with a small size and a light weight yet having all the jumping, wheeling, and aerial maneuvering capabilities.

The major contributions of the robot presented in this chapter can be summarized into two aspects. First, based on our previous robot with a tail [98], we present the design and development of a miniature robot that has three locomotion capabilities: wheeling, jumping, and aerial maneuvering. Although there exists robots having two of them, none has all of the three. Second, we present the detailed dynamic analysis and controller design for the aerial maneuvering using an active tail. Although the dynamics model has been obtained before [60, 62], only the PD controller is adopted for the stabilization control. In this chapter, however, we transform the dynamics model into the standard nonlinear form and design advanced controllers such as nonlinear feedback controller and sliding mode controller.

The remainder of this chapter is organized as follows. First, the detailed robot design is presented in section 3.2. Then, we elaborate the dynamics modeling for aerial maneuvering and optimize the design of the tail to obtain the best dynamic performance in section 3.3. Based on the dynamics model, controllers are designed including a sliding mode controller and a PD controller in section 3.4. Finally, we present simulation and experimental results for aerial maneuvering and demonstrate the multi-modal locomotion abilities of the tailbot.

3.2 Robot Design

The robot design, including mechanical and electrical design, will be elaborated in this section.

3.2.1 Mechanical Design

The solid model and the working principle of the tailbot are illustrated in Fig. 3.2. The whole robot can be divided into two parts: the tail part and the body part as shown in Fig. 3.2(a).

For the tail part, we implement a tail with one degree of freedom to control the body's pitch angle. Fig. 3.2(c) illustrates the detailed design of the tail part. The tail and the body are connected by a revolute joint actuated by a DC motor—labeled as tail motor in the figure. A motor gear is directly attached to the shaft of the motor, and a tail gear meshes with the motor gear. A carbon fiber rod with a steel block shown in Fig. 3.2(a) is fixed to the tail gear. Note that only part of the rod is shown in Fig. 3.2(c). Two teeth of the tail gear are removed to avoid the interference between the tail and the body at limit positions. This is also useful for the wheeling part that will be discussed later.

The tail can also be utilized for mode transition: from wheeling mode to jumping mode and vice versa. On one hand, when the robot wheels on the ground, the tail can push the ground to have the robot stand up and be ready for the next jump. On the other hand, when the robot stands for jumping, the tail can also push the ground to make the robot lie down for wheeling. The detail process can be found in the experimental part for mode transition.

The design for the tail part should ensure rapid control of the body's orientation since the jumping process lasts for a short time (less than one second for a one meter jumping height). Therefore, an optimal design will be performed to obtain the optimal parameters for the tail based on the dynamics model in the next section.

The body part comes from the MSU jumper. It consists of two major components: the jumping mechanism and the energy mechanism. Since the detailed design is already discussed in the previous chapter, we omit them here. However, the working principles for these two mechanisms are illustrated in Fig. 3.2(e) and (f), respectively.

The foot has a tilted angle of 15° to make it take off at an angle of 75°. However, since the revolute joints in the jumping mechanism are realized by a pin-hole structure, the takeoff angle may vary within $\pm 5^\circ$ as demonstrated in our previous experiments [99].

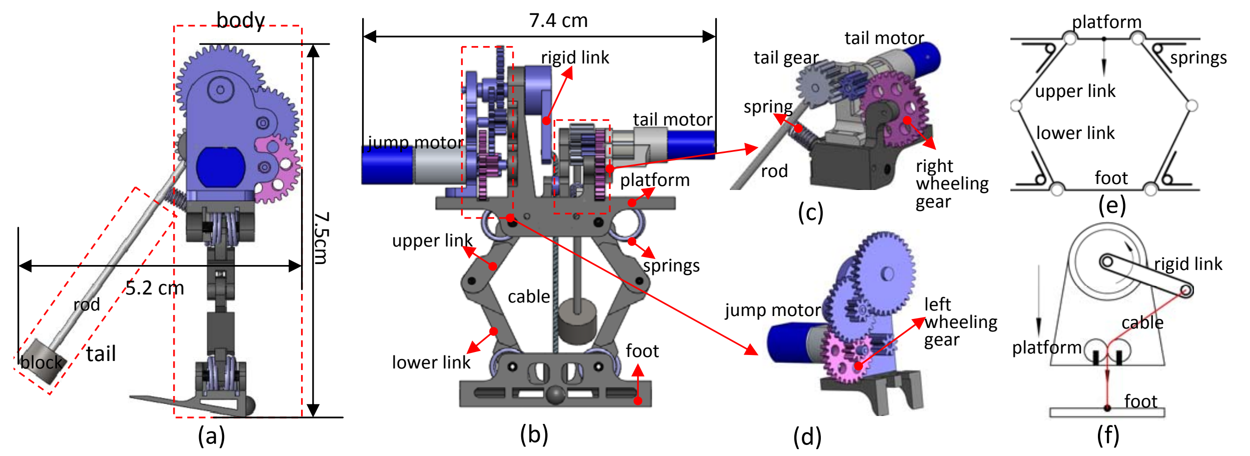

Figure 3.2 Mechanical design of the tailbot: (a) Left view with height and width, and the robot is divided into the body and tail part encircled by two rectangles; (b) Front view with length, and two major parts encircled by two rectangles are shown in (c) and (d), respectively; (c) Section view of the tail part; (d) Section view of the gear train part for the energy mechanism; (e) Working principle of the jumping mechanism; (f) Working principle of the energy mechanism.

In addition to the jumping mechanism and energy mechanism, the robot has two wheeling gears as shown in Fig. 3.2(c) and (d), which are employed for differential drive on the ground. Note that the robot's wheeling posture, once it lands on the ground, can be guaranteed. In fact, the robot has a rectangular shape with two sides much larger than the other four; therefore, it will land on the ground with one of the two large sides. It can wheel if it lands with the side having the two wheeling gears on the ground. If it lands with the other large side, the tail can rotate to turn the robot upside down so that the robot can still wheel on the ground.

The wheeling part does not require extra actuation. The left wheeling gear is part of the gear train for the energy mechanism as shown in Fig. 3.2(d). If the jump motor rotates in one direction, the rigid link will rotate to charge and release the energy. But if the motor rotates in the opposite direction, the rigid link will stay still due to the one-way bearing. In this case, the left wheeling gear is used for the wheeling motion.

The right wheeling gear is actuated by the tail motor as shown in Fig. 3.2(c). Since the tail gear has two teeth removed, once the tail reaches the left limit position shown in Fig. 3.2(c), the counterclockwise rotation of the motor gear cannot actuate the tail. In this case, the right wheeling gear can be used for the wheeling motion. To switch from wheeling mode to jumping mode, a small extension spring placed perpendicular to the tail at the left limit position can re-engage the tail gear and motor gear if the tail motor rotates clockwisely.

The turning motion is realized by actuating one wheeling gear while keeping the other one still. Therefore, the robot can turn in both counterclockwise and clockwise directions.

3.2.2 Electrical Design

A miniature embedded system is designed to enable tetherless or autonomous operation of the tailbot. It is implemented by a printed circuit board with a dimension of $2.5cm \times 2.5cm$ and a mass of 1.3 g. The system has four parts: the central processing unit, the sensing unit, the actuation unit, and the power supply unit. Fig. 3.3 illustrates the architecture of the system.

A microcontroller (ATmega128RFA1 from Atmel) serves as the central processing unit, which has an integrated 2.4GHz Zigbee transceiver. It enables the two-way data transmission between a computer and the robot. Moreover, multiple robots are able to communicate with each other to form a mobile sensor network.

The sensing elements contain a tri-axis accelerometer, a tri-axis gyroscope, and a tri-axis magnetic compass. We use a single chip for the former two sensors (MPU-6050 from Invensense) and another chip for the compass (HMC5883L from Honeywell). The accelerometer can detect the free fall, while the gyroscope can feedback the body's angle and angular velocity to the microcontroller. The compass can feedback the heading direction when the

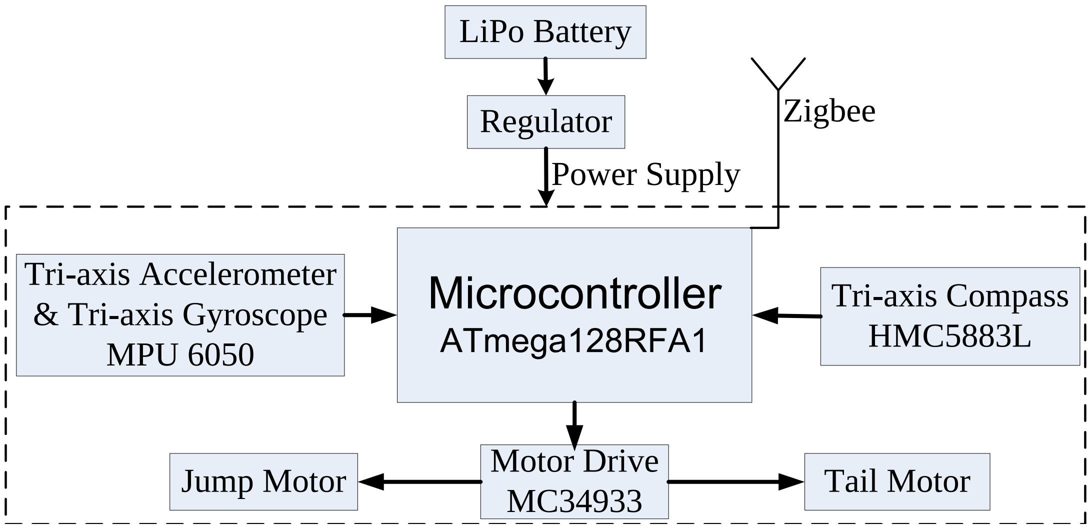
LiPo Battery
Regulator
Power Supply
Zigbee
Tri-axis Accelerometer & Tri-axis Gyroscope MPU 6050
Microcontroller ATmega128RFA1
Tri-axis Compass HMC5883L
Jump Motor
Motor Drive MC34933
Tail Motor

Figure 3.3 The architecture of the embedded control system.

robot wheels on the ground.

The actuation unit is a dual H-Bridge motor driver with pulse width modulation ability (MC34933 from Freescale) to control both the jump motor and tail motor. A FullRiver 50mAh LiPo battery—after being regulated to 3.3 V—powers the whole robotic system. The charging time for such a battery is less than 15 minutes. However, the battery can power the robot's jump for more than 50 times.

The embedded system and the battery are sandwiched between the platform and the tail motor (Fig. 3.2(b)). With such a system, the robot can perform thetherless operations. Commands can be sent to the robot through Zigbee to control its working mode such as jumping or wheeling. Moreover, the robot can also perform autonomous aerial maneuvering once it leaps into the air. The details will be discussed in the experimental section.

3.3 Dynamics Model and Tail Optimization

3.3.1 Dynamics Model

Successful aerial maneuvering requires the robot's mid-air dynamics model, which belongs to the dynamics for coupled rigid bodies during free fall. Early efforts emphasized theoretical analysis such as controllability and optimality. Li and Montgomery studied the orientation control of a planar legged robot with active joints [100]. Berkemeier and Fearing investigated the flight control of a two-link robot with only one active revolute joint [101]. Chen and Sreenath examined the controllability of a spatial two-body system with zero angular momentum [102].

In the last decade, researchers designed controllers for two coupled rigid bodies during free-fall. Mather and Yim investigated the controlled fall for modular robots [103]. Yang *et al.* [104] modeled two rigid bodies connected by a spherical joint in three dimensional space and designed controllers using input-output linearization. Later, they studied the control of two rigid bodies connected by a universal joint [105]. Agrawal and Zhang utilized differential flatness to control two rigid bodies connected by a revolute joint [106]. Most recently, Chang-Siu *et al.* [107] studied the nonlinear control of a two link tailed robot with two degree-of-freedom actuation.

The tailbot shown in Fig. 3.2(a) can be abstracted as shown in Fig. 3.4, where the body is connected to the tail via an actuated revolute joint at point C. Suppose the center of mass for the tail, body, and whole robot be at point A, B, and O, respectively. We attach a frame $OXYZ$ to the robot's center of mass O with X axis along the horizontal direction, Y axis along the vertical direction, and Z axis determined by the right hand rule. The body's three orientation angles—roll, pitch, and yaw—are shown at the lower right part of Fig. 3.4.

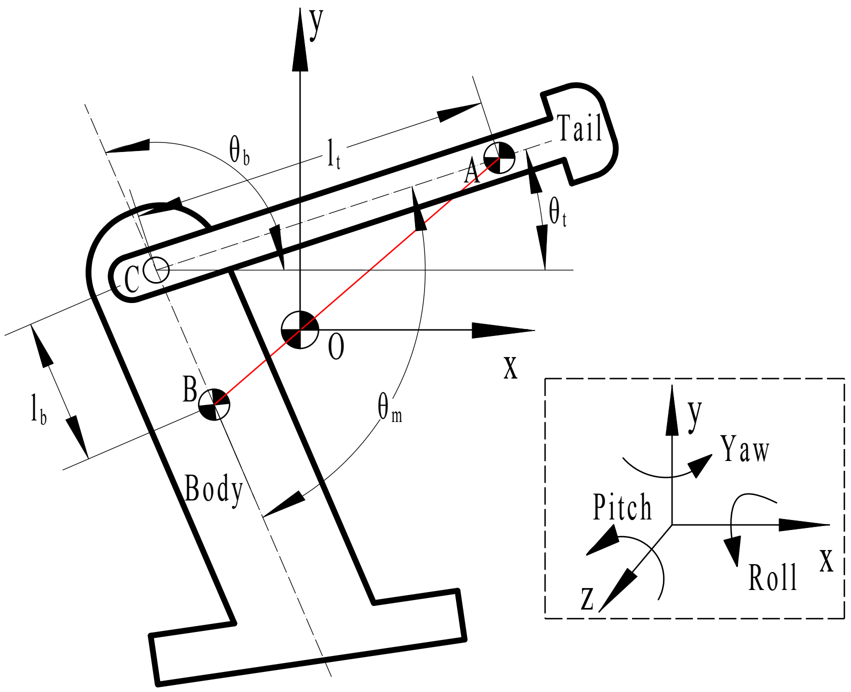

Figure 3.4 The schematic of the tailbot in mid-air for dynamics modeling, where the body and the tail are connected by a revolute joint at point C (Fig. 3.2(a) shows the tail and body part with solid models).

Note that the angles are defined with respect to frame $OXYZ$ that will move with the robot. By actively swinging the tail, the body's pitch angle can be controlled. In this section, we obtain the system's dynamics equation and transform it into a standard nonlinear system.

Table 3.1 List of parameters for dynamics modeling

m_b	body mass
m_t	tail mass
l_b	length of link BC
l_t	length of link AC
θ_b	body angle with respect to the horizontal line
θ_t	tail angle with respect to the horizontal line
I_b	body moment of inertial
I_t	tail moment of inertial

For the system in Fig. 3.4, we use the parameters listed in Table 3.1 in the following discussions. Denote the coordinates for point A and point B in frame $OXYZ$ as $\vec{A}$ and $\vec{B}$, respectively. They can be obtained using the relation $|AO|/|BO| = m_b/m_t$ and trigonometric equations in $\triangle ABC$.

The Euler-Lagrange method is used to obtain the dynamic equations. For this method, the Lagrangian for the system should be first derived. Because frame $OXYZ$ is fixed with the robot, its translational motion decouples from the rotational motion once it jumps into air [100]. Since the translational motion is a simple projectile motion [99], we only consider the rotational motion for aerial maneuvering. Without the translational motion, the robot's potential energy is zero. Therefore, the Lagrangian is just the system's kinetic energy:

$$\begin{aligned}\mathcal{L} &= \frac{1}{2}I_t\dot{\theta}_t^2 + \frac{1}{2}m_t||\dot{\vec{A}}||_2^2 + \frac{1}{2}I_b\dot{\theta}_b^2 + \frac{1}{2}m_b||\dot{\vec{B}}||_2^2 \\ &= \frac{1}{2}[I_t\dot{\theta}_t^2 + I_b\dot{\theta}_b^2 + \frac{m_t m_b(l_t^2\dot{\theta}_t^2 + l_b^2\dot{\theta}_b^2 - 2l_t l_b\dot{\theta}_t\dot{\theta}_b\cos\theta_m)}{m_t + m_b}]\end{aligned}$$

where $\theta_m = \pi + \theta_t - \theta_b$, shown in Fig. 3.4, is the actuator's rotation angle. Neglecting the air resistance and applying the Euler-Lagrange method, we obtain the dynamics equation as:

$$M\ddot{\theta}_t - L\cos\theta_m\ddot{\theta}_b - L\sin\theta_m\dot{\theta}_b^2 = \tau \tag{3.1}$$

$$N\ddot{\theta}_b - L\cos\theta_m\ddot{\theta}_t + L\sin\theta_m\dot{\theta}_t^2 = -\tau \tag{3.2}$$

where

$$M = I_t + \frac{m_t m_b l_t^2}{m_t + m_b}, \quad N = I_b + \frac{m_t m_b l_b^2}{m_t + m_b}, \quad L = \frac{m_t m_b l_t l_b}{m_t + m_b}$$

τ is the actuation torque from the motor. Note that we only have one τ for external forces since only one actuator is used at the revolute joint.

For the system described by Eqs. (3.1) and (3.2), if both θ_t and θ_b should be controlled to desired values, then the system is underactuated since only one input τ exists. In this chapter, however, we only care about the robot's body angle θ_b. To control θ_b, Eqs. (3.1) and (3.2) should be transformed into a single equation by eliminating θ_t, but this is impossible due to the nonlinear coupling between θ_t and θ_b. Nevertheless, Eqs. (3.1) and (3.2) can be converted to a new equation with θ_m and $\dot{\theta}_m$ as the state variable using the following steps.

First, we solve $\ddot{\theta}_t$ and $\ddot{\theta}_b$ from Eqs. (3.1) and (3.2):

$$\ddot{\theta}_t = \frac{-SL\dot{\theta}_t^2 \cos\theta_m + SN\dot{\theta}_b^2 + R\tau}{T} \tag{3.3}$$

$$\ddot{\theta}_b = \frac{-SM\dot{\theta}_t^2 + SL\dot{\theta}_b^2 \cos\theta_m - Q\tau}{T} \tag{3.4}$$

where

$$Q = M - L\cos\theta_m \qquad R = N - L\cos\theta_m \tag{3.5}$$

$$S = L\sin\theta_m \qquad T = MN - L^2\cos^2\theta_m \tag{3.6}$$

Since $T \geq MN - L^2 > 0$, there is no singularity for using T as the denominator in Eqs. (3.3) and (3.4). From (3.4) – (3.3) and $\ddot{\theta}_m = \ddot{\theta}_t - \ddot{\theta}_b$, we have:

$$\ddot{\theta}_m = \frac{SQ\dot{\theta}_t^2 + SR\dot{\theta}_b^2}{T} + \frac{Q+R}{T}\tau \tag{3.7}$$

Second, we utilize the conservation of angular momentum to eliminate both $\dot{\theta}_t$ and $\dot{\theta}_b$ in Eq. (3.7) by expressing them as a function of $\dot{\theta}_m$. In fact, the angular momentum for the total system can be obtained as:

$$H_0 = (M - L\cos\theta_m)\dot{\theta}_t + (N - L\cos\theta_m)\dot{\theta}_b = Q\dot{\theta}_t + R\dot{\theta}_b$$

If the air resistance is negligible, then H_0 is a constant. Since $\dot{\theta}_m = \dot{\theta}_t - \dot{\theta}_b$, $\dot{\theta}_t$ and $\dot{\theta}_b$ can be solved as follows:

$$\dot{\theta}_t = \frac{R\dot{\theta}_m}{Q+R} + \frac{H_0}{Q+R} \tag{3.8}$$

$$\dot{\theta}_b = \frac{-Q\dot{\theta}_m}{Q+R} + \frac{H_0}{Q+R} \tag{3.9}$$

Finally, plugging Eqs. (3.8) and (3.9) into (3.7), we obtain:

$$\ddot{\theta}_m = \frac{QRS\dot{\theta}_m^2 + SH_0^2}{T(Q+R)} + \frac{Q+R}{T}\tau \tag{3.10}$$

Let $x = [\theta_m, \dot{\theta}_m]^T$ and $u = \tau$. Then from Eqs. (3.10), the system can be written as:

$$\dot{x} = f(x) + g(x)u \tag{3.11}$$

with

$$f(x) = \begin{bmatrix} x_2 \\ \dfrac{QRSx_2^2 + SH_0^2}{T(Q+R)} \end{bmatrix}, \quad g(x) = \begin{bmatrix} 0 \\ \dfrac{Q+R}{T} \end{bmatrix} \tag{3.12}$$

Since the initial angular momentum is difficult to measure, the case of zero angular momentum ($H_0 = 0$) will be considered in this chapter.

Based on the state space model, controllers can be designed to stabilize the body angle θ_b at a desired constant angle θ_b^*. However, since the embedded control system attached to the robot body can only feedback body's angular velocity $\dot{\theta}_b$ and consequently the output $y = \theta_b$, the state $x = [\theta_m, \dot{\theta}_m]^T$ is unavailable. Therefore, we cannot design state feedback controllers for the system, and we need to transform the system with θ_b as the state variable.

Let the new state $z = [\theta_b, \dot{\theta}_b]^T$ and the output $y = \theta_b$, then the system can be transformed to the following:

$$\dot{z} = A_c z + B_c \left[-\frac{Q}{T} u - \frac{Q^2RS + ST(R-Q)}{TQ^2} z_2^2 \right] \tag{3.13}$$

$$y = C_c z \tag{3.14}$$

where

$$A_c = \begin{bmatrix} 0 & 1 \\ 0 & 0 \end{bmatrix}, \quad B_c = \begin{bmatrix} 0 \\ 1 \end{bmatrix}, \quad C_c = \begin{bmatrix} 1 & 0 \end{bmatrix}$$

If we want to stabilize the output—the body angle θ_b—at a constant angle θ_b^*, which requires $z^* = [\theta_b^*, 0]^T$. Let $\bar{z} = z - z^* == [\bar{z}_1, \bar{z}_2]^T$. Since $A_c z^* = [0, 0]^T$, Eq. (3.13) can be rewritten as

$$\dot{\bar{z}} = A_c \bar{z} + B_c \left[-\frac{Q}{T} u - \frac{Q^2RS + ST(R-Q)}{TQ^2} \bar{z}_2^2 \right] \tag{3.15}$$

Therefore, regulating θ_b to θ_b^* is equivalent to stabilize the system in Eq. (3.15) to the origin. Eq. (3.15) can be written out as

$$\dot{\bar{z}}_1 = \bar{z}_2, \quad \dot{\bar{z}}_2 = pu + q \tag{3.16}$$

where

$$p = -\frac{Q}{T}, \quad q = -\frac{Q^2RS + ST(R-Q)}{TQ^2} \bar{z}_2^2$$

Note that p and q are functions of $\bar{z}$ and $x_1 = \theta_m$, although explicit forms are not written out.

The same dynamics in Eqs. (3.1) and (3.2) has been obtained before using Newtonian mechanics [60, 62, 63]. Nevertheless, none of them tries to formulate the problem in the standard form shown in Eqs. (3.11), which facilities the controller design in the next section.

3.3.2 Tail Optimization

With the dynamics model, the tail can be optimally designed to achieve the best dynamic performance in mid-air. The performance can be measured by indices such as rising time, settling time, or steady state error, etc. Such indices depend on the designed controller and the robot's parameters such as those listed in Table 3.1. Therefore, the general optimization problem can be formulated as:

$$\text{max or min} \quad \mathcal{M} = f(u(t), p)$$

where $\mathcal{M}$ is a specific performance index, $u(t)$ is the control input, and p represents the robot's parameters.

This optimization represents a new problem in optimal design since it blends both the controller and the robot's parameters, and we need to solve them together. As our first step, however, we focus on the mechanism optimization by solving a simplified version without the controller. Specifically, we aim to obtain an optimal tail design that maximizes the change of body angle θ_b for a given short time with the tail motor actuated by a constant rated voltage supply.

With a constant rated voltage supply, the torque τ is related to its angular speed $\dot{\theta}_m$ by $\tau = \tau_s(1 - \dot{\theta}_m/\omega_0)$, where τ_s is the motor's stall torque and ω_0 is the no-load angular speed. In this case, Eq. (3.10) becomes a second order ordinary differential equation for θ_m:

$$\ddot{\theta}_m = \frac{QRS\dot{\theta}_m^2}{T(Q+R)} + \frac{Q+R}{T}\tau_s(1 - \frac{\dot{\theta}_m}{\omega_0}) \tag{3.17}$$

From Eq. (3.17), we can solve $\theta_m(t)$. With $\theta_m(t)$, the body angle's trajectory can be derived from Eq. (3.9).

$$\theta_b = \int \frac{-Qx_2 + H_0}{Q + R} + \theta_b(0) \tag{3.18}$$

where $\theta_b(0)$ is the initial angle for θ_b.

Using Eq. (3.17), we perform the optimal design in four steps: identifying optimization variables, formulating the objective function, obtaining the constraints, and solving the constraint optimization problem.

The parameters for the tail part design include m_t, l_t, I_t, and the speed reduction ratio r between the motor gear and the tail gear (Fig. 3.2(c)). Since the carbon fiber rod in the tail part has a negligible mass compared with the steel block, the tail's moment of inertial I_t can be approximated as $I_t = m_t l_t^2$. Therefore, the optimization variables are m_t, l_t, and r. Note that m_b, l_b, and I_b are known based on our previous jumping robot [99]. To simplify the design, we choose the tail motor empirically (GH6123S from Gizmoszone) by estimating the required torque and speed.

The objective function for the optimization problem is chosen to be the change of θ_b. Specifically, an optimal design is one that maximizes the change of θ_b for a small fixed time period (0.1 s) under a given constant rated voltage. To achieve this goal, we consider θ_b as a function of m_t, l_t, and r from Eq. (3.17), and denote this function as $\theta_b(t) = f(m_t, l_t, r)$.

The optimization constraints are derived as follows. Since a large weight decreases the jumping performance and increases the landing impact, we let $m_t \le 0.15 m_b$. On the other hand, since m_t cannot be too small to perform effective aerial maneuvering, we constrain $m_t \ge 0.05 m_b$. With similar practical reasons, let $0.75 L_b \le l_t \le 1.5 L_b$ and $0.1 \le r \le 10$ with $L_b = 7.5$ cm being the maximum body length (L_b is different from l_b in Fig. 3.4).

Based on the previous discussions, the optimal design problem is formulated as:

$$\begin{aligned} \max \quad & \theta_b(0.1) = f(m_t, l_t, r) & & \\ \text{subject to} \quad & 0.05 m_b \leq m_t \leq 0.15 m_b, & & 0.1 \leq r \leq 10 \\ & 0.75 L_b \leq l_t \leq 1.5 L_b, & & \theta_b(0) = \mathit{constant} \end{aligned}$$

The optimization problem is solved using the Optimization toolbox in Matlab. Specifically, the *fmincon* function with the interior point algorithm is adopted. To avoid local minima, we run the optimization algorithm 50 times with random initial points. For all of them, the optimal result is $m_t = 1.3$ g, $l_t = 6.8$ cm, and $r = 2.2$. With the optimal parameters, θ_b can change 80 degrees in 0.1 s. To accommodate the available off-the-shelf gears, we choose $r = 2$. In this case, the value of $\theta_b(0.1)$ only decreases about 0.1%.

Based on the optimal design, the tail's parameters are chosen as follows. The length of the carbon fiber rod is $l_t = 6.8$ cm, and the mass for the steel block is $m_t = 1.3$ g. For the gear train that actuates both the tail and the right wheeling gear (Fig. 3.2(c)), the motor gear has 8 teeth, the tail gear has 16 teeth since $r = 2$, and the right wheeling gear has 28 teeth which is the same with the left wheeling gear.

3.4 Controller Design

In this section, a sliding mode controller is designed to regulate θ_b to θ_b^*. Additionally, we also discuss a special case to design a PD controller.

3.4.1 Sliding Mode Controller

Sliding mode control attains the control goal in two steps. First, the system's trajectory undergoes a reaching phase to a sliding surface. Second, the trajectory is constrained to the sliding surface to approach the equilibrium during the sliding phase [108]. Let the sliding surface be $s = a\bar{z}_1 + \bar{z}_2$ with $a > 0$ a constant which determines the convergent speed during the sliding phase.

As shown in the following, we have $Q > 0$ and the following two items are upper bounded with the bounds denoted by k_1 and k_2, respectively:

$$\left|\frac{T}{Q}\right| \leq k_1, \quad \left|\frac{Q^2RS + ST(R-Q)}{Q^3}\right| \leq k_2$$

First we show that $Q > 0$. In fact,

$$Q = M - L\cos\theta_m \geq M - L = I_t + \frac{m_t m_b l_t (l_t - l_b)}{m_t + m_b} > 0$$

since l_t is much larger than l_b in our implementations. The bound for the first item $|T/Q|$ can be obtained as:

$$\left|\frac{T}{Q}\right| = \frac{MN - L^2\cos^2\theta_m}{M - L\cos\theta_m} \leq \frac{MN}{M-L} := k_1$$

The bound for the second item is:

$$\begin{aligned}\left|\frac{Q^2RS + ST(R-Q)}{Q^3}\right| &= \frac{|Q^2RS + ST(R-Q)|}{Q^3} \leq \frac{Q^2|R||S| + T|S||R-Q|}{Q^3} \\ &\leq \frac{(N+L)L}{M-L} + \frac{LMN|N-M|}{(M-L)^3} := k_2\end{aligned}$$

Based on the above results, we have the following theorem:

Theorem 1 *The following controller can asymptotically stabilize the system represented by Eq.* (3.15) *at the origin:*

$$u = (ak_1|\bar{z}_2| + k_2\bar{z}_2^2 + k_3)\ sgn(a\bar{z}_1 + \bar{z}_2) \tag{3.19}$$

where $k_3 > 0$ is a constant and $sgn(\cdot)$ is the sign function.

Proof 1 *We first show that the system will reach the sliding surface. Define a Lyapunov function as $V = s^2/2$, then:*

$$\dot{V} = s\dot{s} = s(a\dot{\bar{z}}_1 + \dot{\bar{z}}_2) = s(a\bar{z}_2 + q) + pus$$

Since

$$\left|\frac{a\bar{z}_2 + q}{p}\right| = \left|-\frac{aT}{Q}\bar{z}_2 + \frac{Q^2RS + ST(R-Q)}{Q^3}\bar{z}_2^2\right| \le ak_1|\bar{z}_2| + k_2\bar{z}_2^2$$

we have

$$\dot{V} \le |s||a\bar{z}_2 + q| + pus \le -p(ak_1|\bar{z}_2| + k_2\bar{z}_2^2)|s| + pus = k_3p|s|$$

Since $p = -Q/T < 0$, we have $\dot{V} < 0$ for any $s \neq 0$. Therefore, the system will reach the sliding surface in finite time. After that, it will be governed by $\dot{\bar{z}}_1 = -a\bar{z}_1$ to make the state approach the origin.

The sliding mode controller in Eq. (3.19) only needs the feedback of transformed state $z_1 = \theta_b$ and $z_2 = \dot{\theta}_b$, which are available from the gyroscope. Moreover, during the implementation, we can use a simplified controller

$$u = k\ \mathrm{sgn}(a\bar{z}_1 + \bar{z}_2) \tag{3.20}$$

with $k > ak_1|\bar{z}_2| + k_2\bar{z}_2^2 + k_3$. The stability for the system using this controller can also be verified by showing $\dot{V} < 0$.

3.4.2 Proportional-Derivative (PD) Controller

Besides the sliding mode controller, we examine the controller design for a special case when $l_b = 0$, which is detailed in [63]. This special case approximates the situation when the robot has a very small l_b such as the robots in [62] and [63]. In this case, since $L = m_t m_b l_t l_b/(m_t + m_b) = 0$, the dynamics equation (3.2) is simplified to $N\ddot{\theta}_b = -\tau$. Since $N = I_b$, the simplified system in state space form is thus:

$$\dot{\bar{z}} = A_c\bar{z} - B_c u/I_b \tag{3.21}$$

For this system, a PD controller can be designed as:

$$u = I_b K\bar{z} \tag{3.22}$$

where $K = [K_p,\ K_d]$ is designed to make $A_c - B_c K$ Hurwitz.

Similar to the sliding mode controller, the PD controller only needs the feedback of the transformed state. Therefore, we will include experimental results for the PD controller in the next section since l_b for our robot is close to zero.

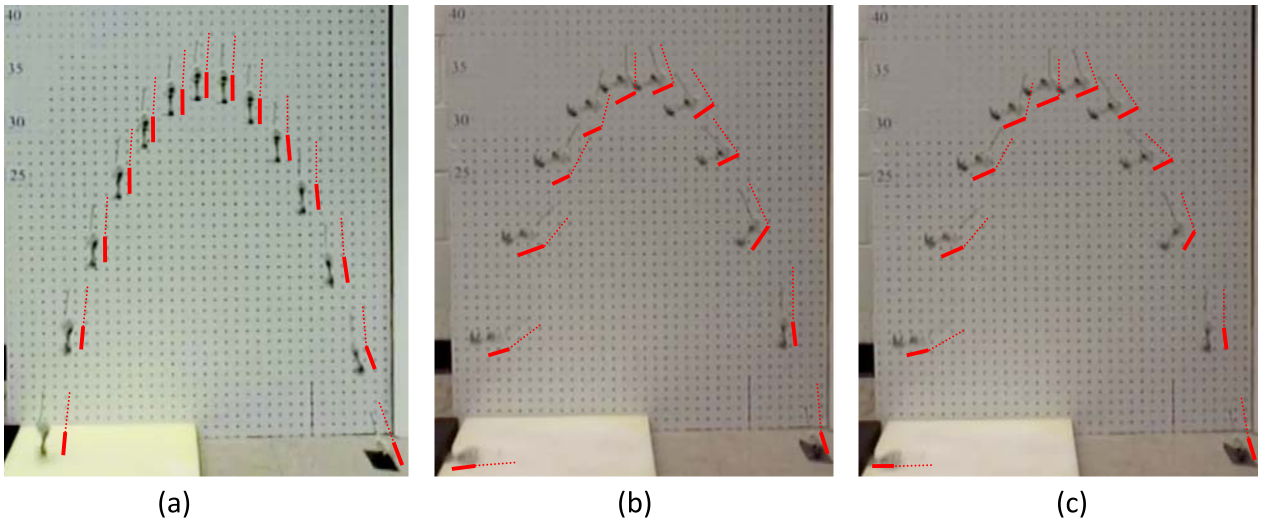

Figure 3.5 Aerial maneuvering results from video frames show the robot trajectory in a single image for three cases. A schematic view for each robot in all the three images is added for illustration purposes. The dashed lines represent the tail, while the solid lines represent the body. (a) the tail is not actuated; (b) the tail is controlled by the PD controller; (c) the tail is controlled by the sliding mode controller. Note that the robot jumps from right to left in the figure.

3.5 Testing Results

With the designed robot, we first simulate the designed controllers and then conduct experiments for aerial maneuvering. In addition, we also perform experiments for mode transitions.

3.5.1 Simulation Results for Aerial Maneuvering

We simulate the aerial maneuvering using Matlab/Simulink to validate the dynamics model and controller design. Based on our robot design, the following parameter values are chosen for the simulation: $m_t = 1.3 \times 10^{-3} kg$, $m_b = 25.2 \times 10^{-3} kg$, $l_t = 6.8 \times 10^{-2} m$, $l_b = 1.0 \times 10^{-2} m$, $I_t = 5.8 \times 10^{-6} kg \cdot m^2$, and $I_b = 1.0 \times 10^{-5} kg \cdot m^2$.

The initial value for θ_b is chosen as 105°, which means the robot takes off at an angle of 75°. The initial value for θ_m is chosen as 180°, which corresponds to the setup in experiments. We let the desired body angle $\theta_b^* = 30°$ to make the robot land on ground with one of the two largest sides.

For the PD controller, we choose $K = [240,\ 20]^T$ to make the system approach θ_b^* within 0.2 second. With all the parameters and the dynamics model, the trajectory of θ_b with respect to time is obtained and shown by the solid line in Fig. 3.6.

For the sliding mode controller, we first calculate the bounds for the two items as: $k_1 = 2.2 \times 10^{-5}$ and $k_2 = 1.96 \times 10^{-6}$. The controller with saturation function is employed to reduce the chattering

$$u = (ak_1|\bar{z}_2| + k_2\bar{z}_2^2 + k_3)\ \mathrm{sat}(\frac{a\bar{z}_1 + \bar{z}_2}{\mu}) \tag{3.23}$$

where sat$(\cdot)$ is the saturation function and μ a positive constant [108]. Let $a = 10$, $k_3 = 5 \times 10^{-4}$, and $\mu = 1$, which are chosen to make the response have a similar profile compared with the PD controller. The trajectory of θ_b for the sliding mode controller is shown as the dash line in Fig. 3.6.

Based on the simulation results, performances of the two controllers are compared and major metrics are listed in Table 3.2. The sliding mode controller has a larger rising time 0.31s compared with 0.21s for the PD controller. However, if we consider the settling time as when θ_b gets and stays within 10% of θ_b^*, then the sliding mode controller settles faster. The steady state errors for both controllers are zero, which verifies the stability of the system. In addition, the PD controller has a larger percent of overshoot compared with the sliding mode controller.

Table 3.2 Simulation results comparison for the two controllers

Metric	PD controller	Sliding mode controller
Rising time (s)	0.21	0.31
Settling time (s)	0.37	0.26
Steady state error (degree)	0	0
Percent of overshoot (%)	18.66	4.56

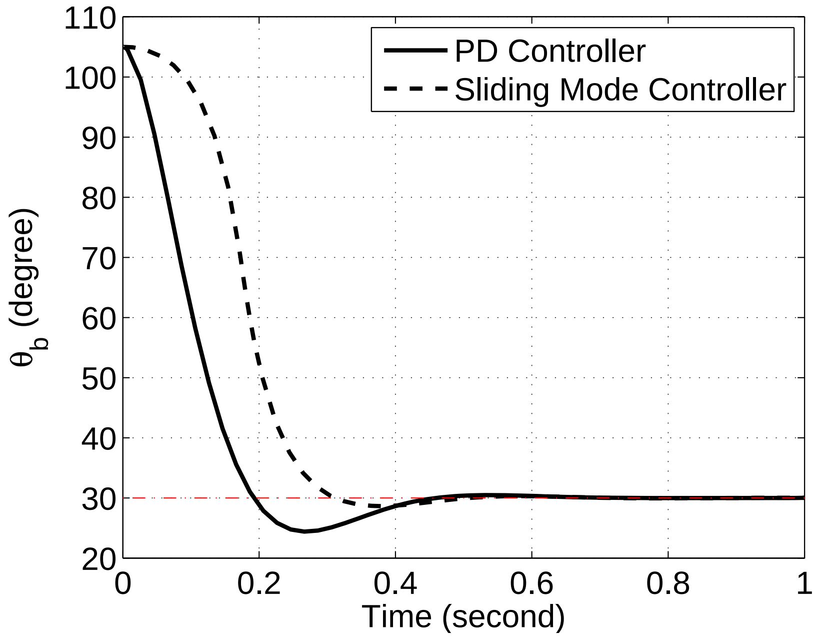

Figure 3.6 Simulation results for the PD controller and the sliding mode controller. Each curve shows the trajectory for θ_b with resect to time for each controller.

3.5.2 Experimental Results for Aerial Maneuvering

Based on the design presented in section 3.2, the robot prototype is built. With the prototype and designed controllers, we conduct aerial maneuvering experiments to test the robot's performance.

The experiments are set up as follows. We let the robot jump in front of a white board with height marks. To minimize the slippage during takeoff, the robot is placed on a sand chapter to provide sufficient friction. Furthermore, the initial position of the tail is carefully adjusted onto the top of the body so that the initial angular momentum can be minimized at takeoff. Note that, however, the initial angular momentum cannot be eliminated as will be explained in the experimental results.

All the sensing, computation, and control are implemented by C programming in the embedded system discussed in section 3.2-B. The microcontroller, ATmega128RFA1, runs at a speed of 8MHz. In each control loop, the microcontroller first samples raw angular velocities from the gyroscope. Then it obtains the current roll, pitch, and yaw angle by numerically integrating the angular velocity using the Runge-Kutta method. Based on the current pitch angle, the control input is computed and the tail motor is actuated using the computed control command. The time for one control loop is three millisecond, and the system can achieve a bandwidth of 333Hz, which is sufficient for feedback control as will be seen in the experimental results. Note that we neglect the drift problem for the gyroscope since the control time for our experiment is less than one second.

Three sets of experiments are conducted. First, to compare with results under active tail control, five jumping experiments with the tail disabled are performed. Second, five experiments with active tail control using the PD controller are conducted. Third, another five experiments using the sliding mode controller are carried out.

During each experiment, we use a Casio Exilim EX-ZR400 high-speed camera with a frame rate of 240 frames/s to record the entire motion. Meanwhile, the body's instantaneous pitch, roll, and yaw angles—defined in Fig. 3.4—are recorded by the embedded control system, which are sent back to a computer wirelessly after landing. The initial pitch angle is obtained using the accelerometer. Since the roll and yaw angle cannot be controlled, we only measure the change for each angle starting from an initial zero angle.

3.5.2.1 Jumping without Tail Actuation

For the five experiments without tail actuation, Fig. 3.5(a) shows the robot's moving trajectory for one of them (jump 2). In the trajectory, the time between each robot is 0.0625s. Referring to the height marked on the left side of the white board, we visualize that the robot jumps 32 inches (81.3 cm). Without actuating the tail, the robot's pitch angle only changes slightly due to a small initial angular momentum. The landing posture of the robot is bad since landing on its feet may cause the robot to bounce severely on the ground, increasing the probability of damage.

For jumping with the tail disabled, if there is no initial angular momentum and the air resistance is neglected, the pitch, roll, and yaw angles should be constants all the time. Fig. 3.7 shows the robot's mid-air orientation for the five jumps, where the pitch, roll, and yaw angles are plotted with respect to time. For all the jumps, the pitch angles do not change too much since only a small initial angular momentum affects the pitch angles. In this case, the pitch angles should change linearly; however, this is not the case in Fig. 3.7 because the tail can slightly rotate even though it is not actuated due to the backlash between the tail gear and the motor gear. From plot (b) and (c) in Fig. 3.7, the roll and yaw angles change almost linearly in random manners. These imply that rotations about other axes are affected by random initial angular momentums that the robot might have after takeoff. Nevertheless, the changes in roll and yaw are relatively small, and they will not cause the robot to flip around in mid-air to affect its landing posture significantly.

3.5.2.2 Aerial Maneuvering with the PD Controller

Experiments for tail actuated jumping are conducted as follows. Initially, the robot stands on the ground, and the accelerometer obtains the initial pitch angle. Once the robot jumps up, the accelerometer detects the free fall and triggers the controller to regulate the body's pitch angle to a desired value by swinging the tail. In mid-air, the gyroscope measures the body's instantaneous angular velocity, and the microcontroller calculates the body's current angle by numerical integrations. With the current angle, current angular velocity, and the desired angle, the controller computes a voltage output for the tail motor to perform controlled aerial maneuvering.

For the PD controller, we tune the values for K_p and K_d by letting the robot fall from a given height since the dynamics is the same as the case when the robot jumps. Using the Ziegler-Nichols tuning method, we obtain values for the controller as $K_p = 40$ and $K_d = 0.3$.

Fig. 3.5(b) shows one of the motion trajectories (jump 1) for the robot using the PD controller. The time between each robot figure is $0.067s$ in the trajectory. Same to the simulations, the desired angle of θ_b is set to be 30°. From the trajectory, the robot rotates its tail to regulate the pitch angle to 30°. Eventually, the robot lands safely on a sponge pad with one of its two large sides.

Fig. 3.8 shows the robot's pitch, roll, and yaw angles with respect to time. Combining Fig. 3.5(b) with Fig. 3.8(a), we observe that the tail rotates counter-clockwisely to make the pitch angle θ_b approach 30°, which is the horizontal yellow solid line in Fig. 3.8(a). The system has a rising time about 0.2s, i.e., the pitch angle reaches 30° in 0.2s. After about 0.3s, it reaches a steady-state value about 28°, although a small oscillation exists. The reason for this oscillation is that the smallest voltage applied to the tail motor is set to be the minimum voltage which the motor overcomes its static friction. This means the motor will not stop running even if the body has reached the desired angle. Additionally, the roll and yaw plots in Fig. 3.8(b) and (c) provide information about rotations in uncontrolled axes. Unlike the case when the tail is disabled, some experiments have nonlinear curves such as the yaw angle for jump 3. The reason is that although the tail is only used to control the pitch angle, manufacturing or assembly error may induce the cross coupling between the tail and yaw or roll angle. Therefore, the rotation of the tail may slightly influence the change of yaw and roll angle.

3.5.2.3 Aerial Maneuvering with the Sliding Mode Controller

Aerial maneuvering with the sliding mode controller is conducted similar to the one using the PD controller. To simplify the parameter tuning process, we employ the simplified controller in Eq. (3.20) with a saturation function sat(·)

$$u = k\,\mathrm{sat}(\frac{a\bar{z}_1 + \bar{z}_2}{\mu}) \tag{3.24}$$

where μ is a positive constant. Similar to the PD controller, we tune the parameters to obtain good performances with the free-fall experiment, and the final parameters are chosen as $k = 255$, $\mu = 600$, and $a = 50$.

Five experiments are performed, and one (jump 4) of the robot's trajectory is shown in Fig. 3.5(c), with a time interval of 0.075s between each robot. As seen from the trajectory, the robot lands on the ground safely with one of its two large sides. The three body angles for five experiments are plotted in Fig. 3.9. From Fig. 3.9(a), the system has a rising time about 0.3s, and the pitch angle θ_b oscillates around 30° thereafter. Compared with results using the PD controller in Fig. 3.8, although the rising time is larger than the PD controller, the sliding mode controller has a smaller overshoot and steady state error. Furthermore, the oscillation after 0.3s is also smaller.

The robot also rotates in roll and yaw as can be seen from Fig. 3.9(b) and (c). Similar to the reason for the PD controller, some of the curves for roll and yaw angle are nonlinear. Nevertheless, these rotations do not significantly affect the landing posture of the robot.

Table 3.3 Experimental results comparison for the two controllers

Metric	PD controller	Sliding mode controller
Rising time (s)	0.19	0.39
Settling time (s)	0.27	0.24
Steady state error (degree)	2.00	0.22
Percent of overshoot (%)	18.25	4.13

3.5.2.4 Comparison of the Two Controllers

To compare the results of the two controllers, we average the results of the five jumps for each controller and plot the averaged result in Fig. 3.10. The data for important metrics are also listed in Table 3.3. For the rising time, the PD controller reaches the desired angle faster, which is the same to the simulation results shown in Table 3.2. The settling time for both controllers, using the same definition for the simulation, is almost the same. However, different from the simulation results, the PD controller has a larger steady state error, which might be due to the discrete implementation of the controller. The percent of overshoot is similar to the simulation results with the sliding mode controller having a smaller overshoot.

3.5.3 Tail Assisted Mode Transition

Besides aerial maneuvering, the tail is also designed for transition between wheeling and jumping during the locomotion. But different from aerial maneuvering, the control of mode transitions is achieved by wireless open loop control. Various commands can be sent from a desktop computer wirelessly to the embedded system, which actuates the tail motor to rotate the tail in different directions with specified speeds. Meanwhile, we visually check the robot's status to make sure it can finish the mode transition successfully.

As explained in the tail design part, the robot can utilize its tail to stand up for jumping from the wheeling mode, and to lie down for wheeling from the jumping mode. Experimental results for these two cases are elaborated in the following.

The first case is to let the robot stand up for jumping when the robot lies on the ground with its side. One experiment for this case is shown in Fig. 3.11, where four frames from a self-righting video are extracted with time labeled on the top right corner. In Fig. 3.11, the robot is first in the wheeling mode with its wheels on the ground. Then, the robot's tail rotates towards the ground to make the robot's wheels away from the ground. After that, the robot starts to store energy and lower its center of mass in order to obtain a stabilizing standing position later. At 12s, the robot is fully charged for jumping and the tail rotates to push the ground such that the robot can complete the transition to a standing position and be ready for taking off. Note that Fig. 3.11 only shows the self-righting from the side with wheels. If the robot lands on the ground with the other side, the tail can rotate in the opposite direction to perform self-righting as well.

The second case is transforming from the jumping mode to the wheeling mode. Fig. 3.12 shows one experimental result of such a transformation. Four frames are extracted from a video that records the process. As shown in the figure, the lying down process is successfully achieved by swinging the tail forward to push the ground, and the robot transforms to the wheeling mode.

3.5.3.1 Wheeling and Turning

The wheeling and turning performances are also tested. In the wheeling experiment, the robot is placed on a white board and beside a ruler in order to determine the wheeling speed. The entire wheeling experiment is recorded by a camera. From the recorded video, we obtain the instantaneous position of the robot in the horizontal direction every 0.36s to create a position plot with respect to time, as shown in Fig. 3.13(a). The black circles represent the experimental data and are connected by black dash lines between neighboring circles. The red solid line is obtained by linear regression and its slope represents the average linear speed—2.91 cm/s. The experimental data plot and the regression plot almost overlap each other, which means the robot runs at an approximately constant speed.

The robot's turning performance and the angular speed are also obtained from experiments. We place the robot on a white board marked with a black straight line as a reference position. Then the robot is controlled to turn, and we obtain the angle between the reference line and the robot's tail every 0.3s. Fig. 3.13(b) shows the plot of the body angles with respect to time for 360° turning. Similarly, the black circles are the experimental data connected by black dash lines, and the red solid line is the projected plot given by linear regression. We can see that the robot turns at a constant angular speed of $59°/s$.

3.6 Conclusions

In this chapter, we have presented the design, analysis, and experimentation of a miniature tailed jumping robot (MSU tailbot) that uses an active tail to maneuver in mid-air for safe landings. Additionally, the tailbot can wheel on the ground when no obstacle exists. The mechanical and electrical designs of the tailbot are detailed. The dynamics model for the tailbot in mid-air is established. Based on the dynamics model, the tail is optimized, and a PD controller and a sliding mode controller are designed. Both simulation and experimental results demonstrate successful aerial maneuvering using the two controllers. From the results, the two controllers have comparable performances with the sliding mode controller having a smaller steady state error in experiments. To the best of our knowledge, the tailbot is the first centimeter scale robot that has all the three capabilities: jumping, wheeling, and aerial maneuvering. With its small size and multi-mode locomotion ability, the tailbot can perform energy efficient locomotion in environments with obstacles, which has many applications such as mobile sensor networks, military surveillance, and environmental monitoring.

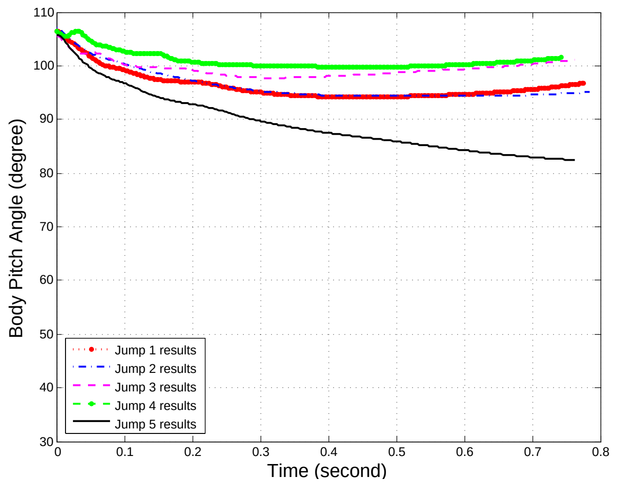

(a)

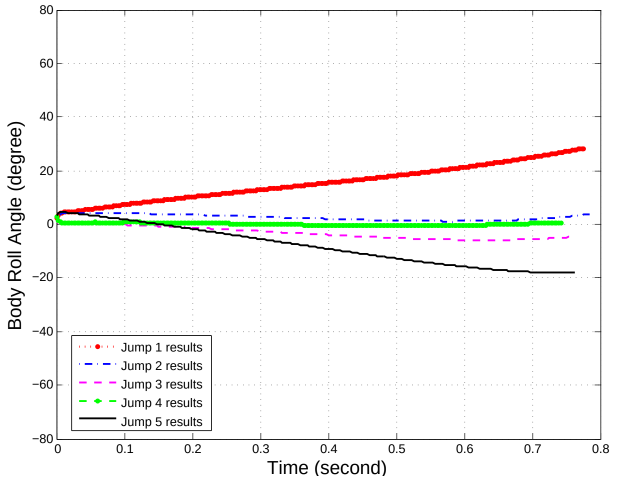

(b)

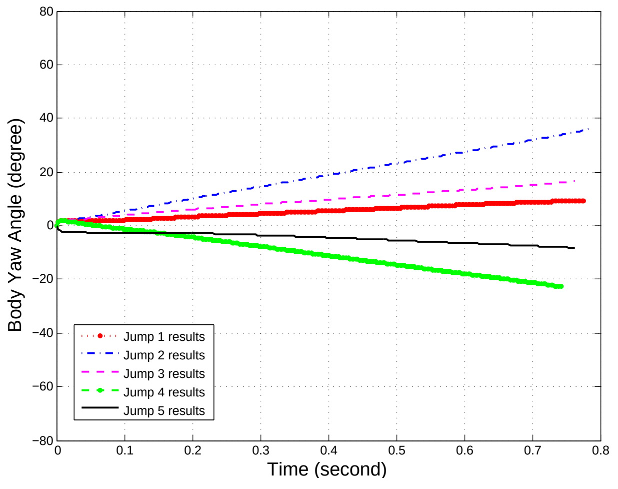

(c)

Figure 3.7 Experimental results for aerial maneuvering when the tail is not actuated: (a) the body's pitch angle with respect to time; (b) the body's roll angle with respect to time; (c) the body's yaw angle with respect to time.

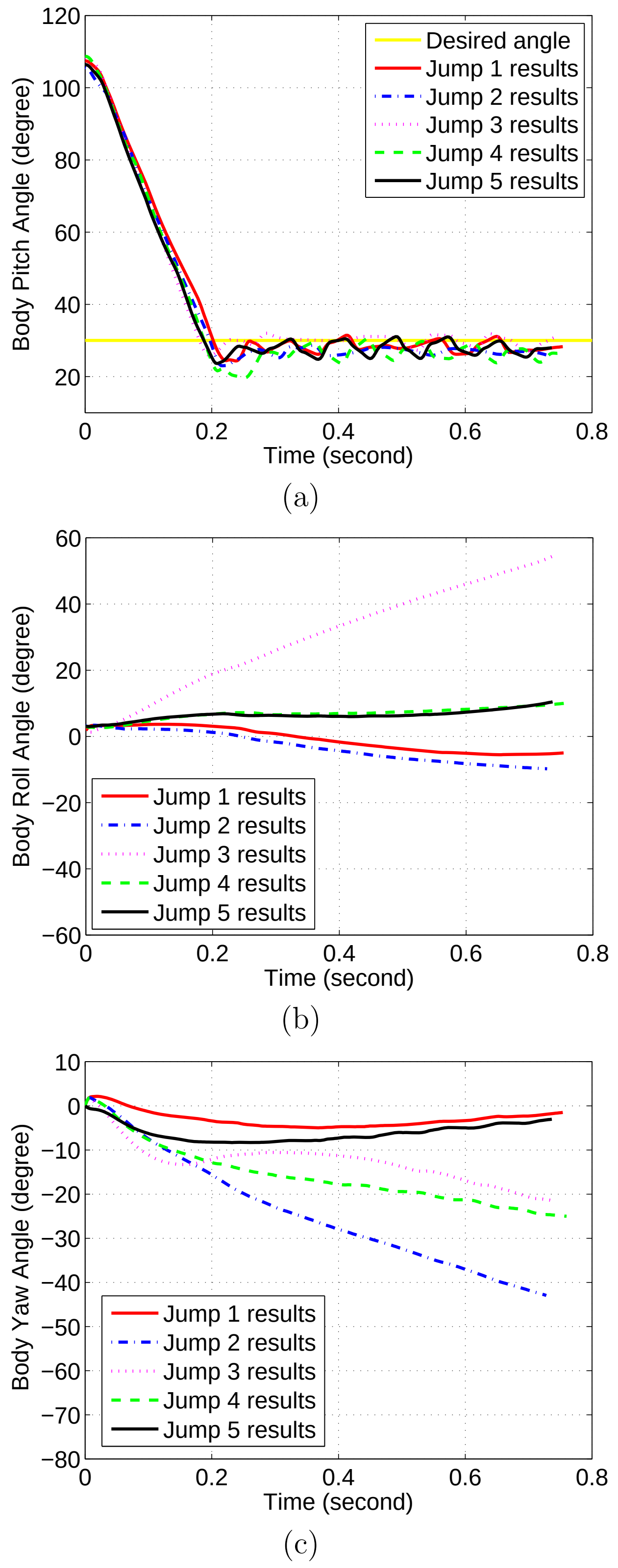

Figure 3.8 Experimental results for aerial maneuvering when the tail is controlled by the PD controller: (a) the body's pitch angle with respect to time; (b) the body's roll angle with respect to time; (c) the body's yaw angle with respect to time.

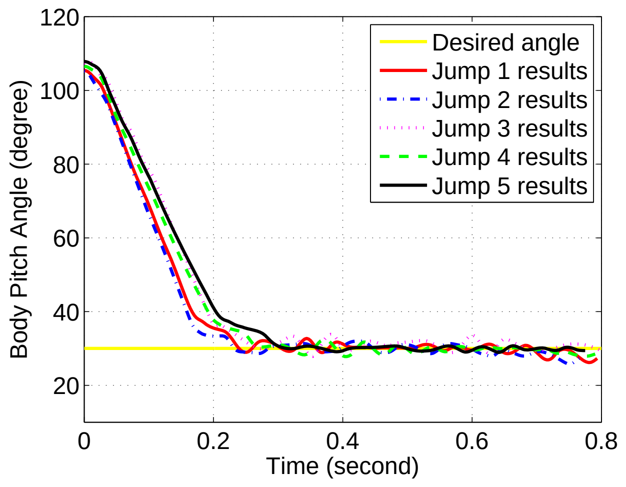

(a)

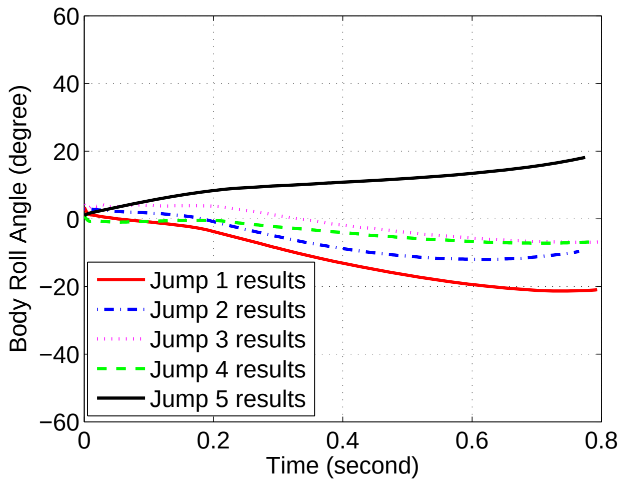

(b)

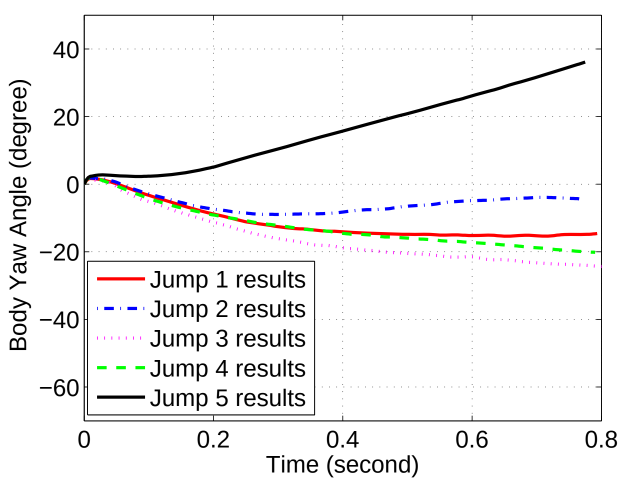

(c)

Figure 3.9 Experimental results for aerial maneuvering when the tail is controlled by the sliding mode controller: (a) the body's pitch angle with respect to time; (b) the body's roll angle with respect to time; (c) the body's yaw angle with respect to time.

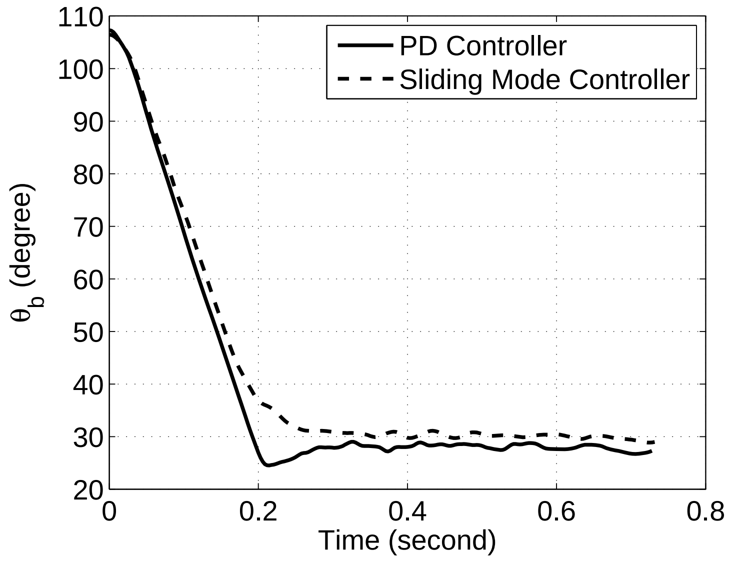

Figure 3.10 Experimental results comparison for the PD controller and the sliding mode controller. The two curves are obtained by averaging the trajectories of five jumps for each controller.

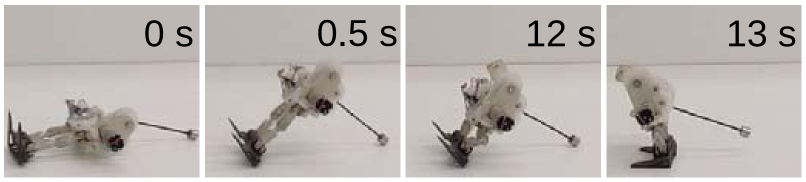

Figure 3.11 Experimental results for transition from wheeling mode to jumping mode.

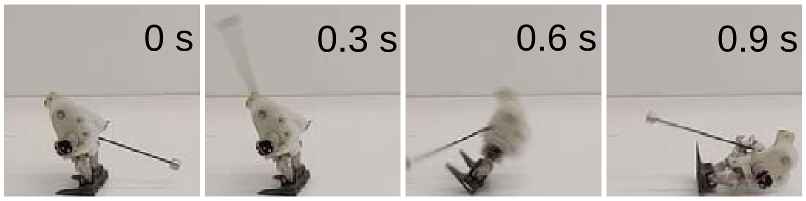

Figure 3.12 Experimental results for transition from jumping mode to wheeling mode.

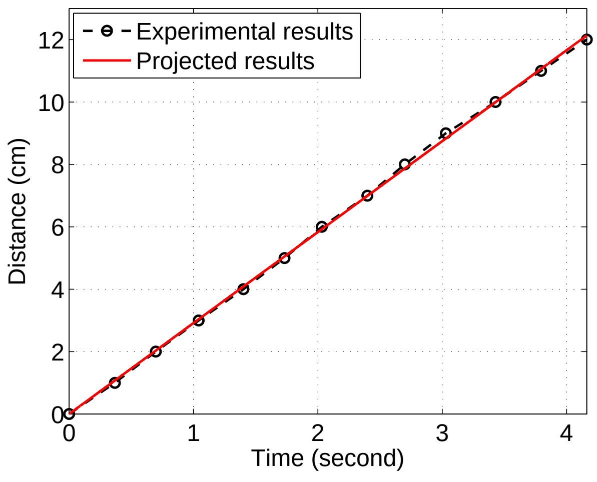

(a)

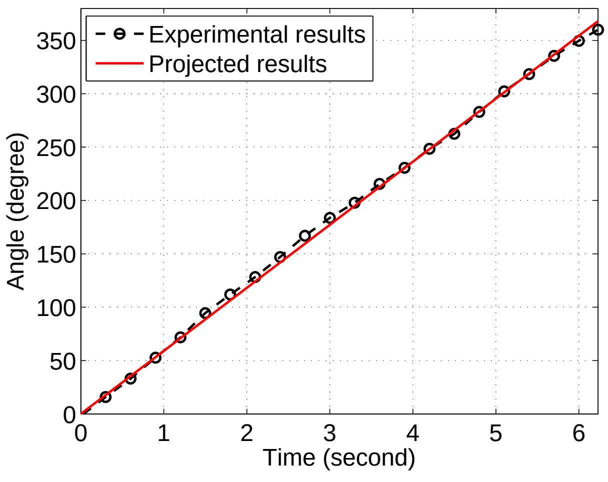

(b)

Figure 3.13 Running and turning experiments: (a) running experimental results and (b) turning experimental results.

Chapter 4

Non-vector Space Control: A Biologically Inspired Control Approach

4.1 Introduction

As discussed in the previous chapter, the MSU tailbot can use an active tail to control its mid-air orientation to land on the ground safely [98, 109]. Specifically, the robot can land with a specific orientation based on the feedback of its body angle from a gyroscope. Since the gyroscope can only feedback a relative angle, the robot's landing capability can only be used in controlled and certain environments. In reality, however, small robots need to interact with uncertain environments. For example, they may need to land on an unknown surface in a specific manner. In this case, they need to rely on vision as a feedback mechanism to achieve such a control goal.

As discussed in Chapter 1, small insects such as bees can achieve marvelous aerial maneuvering such as landing or obstacle avoidance. In this chapter, we aim to investigate vision based landing or perching on some surfaces without prior known orientation for small robots. As shown in Fig. 4.1, the ultimate goal is to make the robot land on an arbitrary surface

(a)

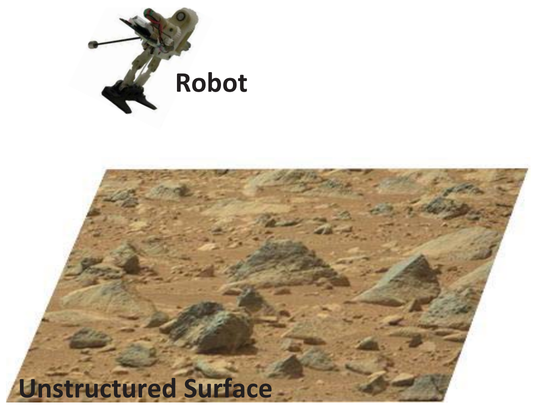

(b)

Figure 4.1 Motivation for vision based robot control: (a) bees can land on an arbitrary surface using vision feedback; (b) how can robots, with similar feedback mechanism, achieve the same feat?

with a given posture such as parallel to the surface using vision feedback. A novel non-vector space approach will be used to obtain the control law. The approach will be implemented on the MSU tailbot that can actively control the body's mid-air orientation using the tail.

The vision based control method presented in this chapter belongs to the literature of visual servoing, which utilizes vision information to control the motion of a mechanical system. For traditional image based visual servoing methods, prominent features are first extracted from the image, and then a controller is designed to make the vector of feature positions converge to a desired value [78]. Two possible issues associate with this feature based vector control method. On the one hand, robust feature extraction and tracking are difficult in natural environments. In fact, most visual servoing experiments are based on artificial fiducial markers [110]. On the other hand, feature extraction suffers from information loss because only the feature information is used for control.

Different from the vision servoing methods which rely on feature extraction and tracking during the control process, small insects perform vision based control without using features. They generate control commands only based on two consecutive images obtained from theirs eyes [44]. How could robots use such biological inspirations to achieve effective vision based control?

We propose a non-vector space control method in this chapter. The general idea is to form a set from an image and formulate the image dynamics in the space of sets. This space is called the non-vector space because the linear structure in the vector space does not exist. Based on the dynamics formulation, a controller can be designed directly on the image sets for visual servoing. This non-vector space control method is different from existing direct visual servoing methods because the problem formulation is different. Initial results for the non-vector space controller have been reported in our previous research [111, 112].

The non-vector space control comes from a general framework called mutation analysis for set evolutions, which is proposed by Aubin [113]. Mutation analysis provides a natural way to describe various physical phenomena because some objects such as shapes and images are basically sets. Since the introduction of mutation analysis, it has been investigated in both theory and applications. On the theory side, it has been recently extended to obtain the viability theorem for morphological inclusions [114] and the general morphological control problems with state constraints [115]. On the application side, it has been applied to image segmentation [116], visual servoing [117], and surveillance networks [118].

The visual servoing using mutational analysis is proposed by Doyen in [117]. Nevertheless, possibly due to its abstract nature, no further extensions are performed afterwards. In this chapter, we try to extend the results. The major extension can be summarized in two aspects. First, the general framework for the non-vector space control is established in this chapter which is not discussed in Doyen's work. Second, the original formulation only deals with binary images, while in this chapter, gray scale images are considered.

The schematic for the vision based robot control in the non-vector space is illustrated in

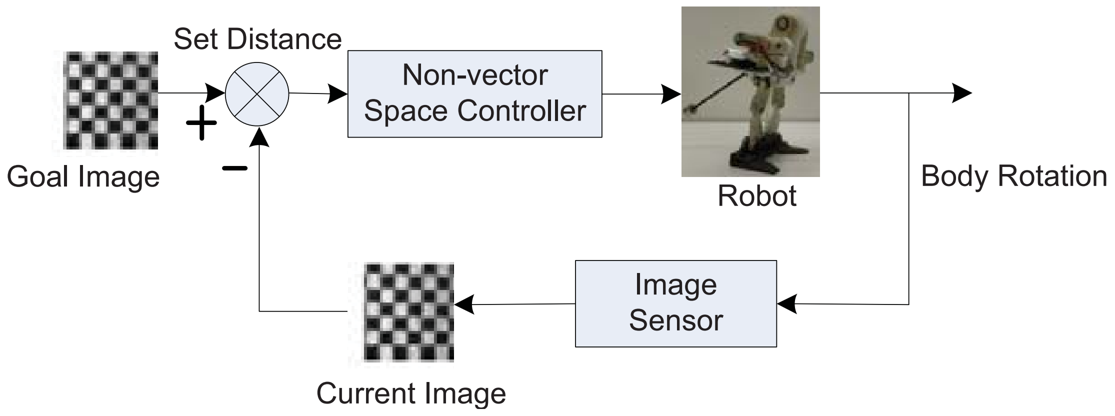

Figure 4.2 Schematic for non-vector space control with the tailbot as an example

Fig. 4.2 with the MSU tailbot as an example. A goal image set corresponding to the desired body orientation is first given. Based on the current image feedback, the non-vector space controller will generate a control signal to drive the body to a desired orientation by swinging the tail. At the new orientation, an updated current image will be obtained, and the same process can be performed repeatedly until the body reaches the desired orientation. Note that this schematic can also be applied to the general framework for visual servoing control by replacing the tailbot in the figure with other mechanical systems.

The major contribution of this chapter can be summarized in two aspects. First, to address the image based control, the direct visual servoing is implemented using the non-vector space control. In this way, no feature extraction and tracking is needed. Second, the general framework for the stabilization problem in the non-vector space is presented. The framework can also be employed to stabilize other systems if the state for the system can be represented as a set.

The rest of the chapter is organized as follows. First of all, the dynamics in the non-vector space is introduced with tools from mutation analysis in section 4.2. After that, the stabilization problem in the non-vector space is introduced in section 4.3, where the stabilizing controller is designed. Then the stabilization controller is applied to visual servoing in section 4.4. Finally, the testing results using a redundant robotic manipulator are given in section 4.5 to validate the theory.

4.2 Dynamics in the Non-vector Space

Before the study of motion control problem with the non-vector space approach, the dynamics should be first formulated. For robotic systems, the governing equation for the robot's motion can be modeled as a differential equation in the vector space. If the feedback image is considered as a set, then this set evolves with the robot's movement. In other words, the differential equation for robot motion induces the set evolution. The evolution with respect to time can be considered as the dynamics in the space of image sets. In this section, the formulation of the dynamics equation in the non-vector space induced from a given differential equation will be discussed.

The space of sets does not have the linear structure in the vector space because the absence of addition and scalar multiplication [119]. Therefore, new tools from the mutational analysis are employed [113]. With the mutation analysis, the time derivative of set evolutions can be formulated. In fact, as will be shown later, the time derivative is the differential equation inducing the set evolutions. With the time derivative, mutation equations in the non-vector space, corresponding to differential equations in the vector space, can be obtained to represent the set dynamics [113]. In the following, the detailed steps for the formulation will be presented.

First of all, the space of sets is defined to form a metric space. Generally, the space, denoted by $\mathcal{P}(\mathbb{R}^n)$, is the power set of $\mathbb{R}^n$, i.e., the collection of all subsets of $\mathbb{R}^n$. Similarly, if the dynamics is constraint to $E \subset \mathbb{R}^n$, then the space is $\mathcal{P}(E)$. In $\mathcal{P}(\mathbb{R}^n)$, we supply a metric $\mathcal{D} : \mathcal{P}(\mathbb{R}^n) \times \mathcal{P}(\mathbb{R}^n) \mapsto \mathbb{R}$ to define the distance between two sets. Any metric is valid if it satisfies the three properties: symmetry, positive definiteness, and triangle inequality [120]. For example, the Hausdorff distance can be such a metric which is defined as follows.

Definition 1 *Consider two sets $X \subset \mathbb{R}^n$ and $Y \subset \mathbb{R}^n$, the distance from a point $x \in X$ to set Y is $d_Y(x) = \inf_{y \in Y} ||y - x||$ with $|| \cdot ||$ representing the Euclidean norm. The Hausdorff distance between X and Y is:*

$$\mathcal{D}(X, Y) = \max \{ \sup_{x \in X} d_Y(x), \sup_{y \in Y} d_X(y) \} \tag{4.1}$$

The metric space supplied with metric $\mathcal{D}$ is denoted as $(\mathcal{P}(\mathbb{R}^n), D)$. We also include the definition of the projection from a point to a set for future use. The projection from $x \in \mathbb{R}^n$ to $Y \subset \mathbb{R}^n$ is defined as $P_Y(x) = \{y \in Y : ||y - x|| = d_Y(x)\}$, which includes all the points in Y that are closest to x.

The gray scale image can be considered as a three dimensional set because each pixel has two pixel index values and one intensity value. Since the cardinality of the set is finite, the Hausdorff distance between two gray scale images X and Y is:

$$\mathcal{D}(X, Y) = \max \{ \max_{x \in X} \min_{y \in Y} ||y - x||, \max_{y \in Y} \min_{x \in X} ||y - x||) \} \tag{4.2}$$

where $x, y \in \mathbb{N}^3$ are vectors formed by three natural numbers. To interpret the distance intuitively, one can consider each image as a surface in the three dimensional Euclidean space, and the above definition is the Hausdorff distance between two surfaces.

4.2.1 Transitions

The set evolution with respect to time in a metric space is called tube. Formally, the tube $K(t) \subset \mathbb{R}^n$ evolving in $(\mathcal{P}(\mathbb{R}^n), \mathcal{D})$ is defined as: $K(t) : \mathbb{R}_{\geq 0} \mapsto \mathcal{P}(\mathbb{R}^n)$ where $\mathbb{R}_{\geq 0}$ is the set of non-negative real numbers. In the case when gray scale images are the sets, the tube is the surface evolution in the three dimensional space.

The transition is required for the definition of the time derivative for tubes. Let $\varphi : E \mapsto \mathbb{R}^n$ with $E \subset \mathbb{R}^n$ be a bounded Lipschitz function. Denote the set of all such functions as $\mathrm{BL}(E, \mathbb{R}^n)$. For ordinary differential equation (ODE) $\dot{x}(t) = \varphi(x(t))$ with initial condition $x(0) = x_0$. The transition for $\varphi \in \mathrm{BL}(E,\, \mathbb{R}^n)$ at time t is defined as:

$$T_\varphi(t, x_0) = \{x(t) : \dot{x}(t) = \varphi(x(t)),\, x(0) = x_0\} \tag{4.3}$$

where $x(t)$ is the solution to $\dot{x}(t) = \varphi(x(t))$. In other words, the transition at time t is the value of solution to a given ODE at the same time. Note that a rigorous definition for transitions requires it to satisfy four conditions [119], but for simplicity, we use the above simplified definition which can be shown to satisfy those four conditions (Ch. 1, Example 3, [119]). The definition can be extended when the initial condition is a set instead of a point as stated in the following definition:

Definition 2 *The transition at time t for a function $\varphi : E \mapsto \mathbb{R}^n$ with $E \subset \mathbb{R}^n$ starting from an initial set K_0 is:*

$$T_\varphi(t, K_0) = \{x(t) : \dot{x}(t) = \varphi(x(t)),\, x(0) \in K_0\} \tag{4.4}$$

Since the initial conditions are in the set K_0 instead of a single point, $T_\varphi(t, K_0)$ is also a set. In fact, $T_\varphi(t, K_0)$ can be considered as a reachable set of points at time t according to $\dot{x} = \varphi(x)$ with the initial points in K_0. It is also a tube evolving from K_0 according to $\dot{x} = \varphi(x)$. Note that this definition also satisfies the four conditions for transitions (Ch. 1, Example 4, [119]). In addition, the transitions discussed here is induced from differential equations, and a general definition with differential inclusions can be defined as well [119].

To illustrate the idea of transitions, consider the case when $x = [x_1, x_2]^{\mathrm{T}}$ and $\varphi(x) = [2, x_1]^{\mathrm{T}}$ with the initial conditions in the set $K_0 = \{x : ||x|| < 1\}$, which includes all the points inside the circle shown in Fig. 4.3. In this case, the transition is:

$$T_\varphi(t, K_0) = \{x(t) : \begin{bmatrix} \dot{x}_1 \\ \dot{x}_2 \end{bmatrix} = \begin{bmatrix} 2 \\ x_1 \end{bmatrix}, x(0) \in K_0\}$$

Solving the ODE, we can obtain the transition set at a given time t. For example, the transition set $T_\varphi(1.5, K_0)$, shown in Fig. 4.3, contains all the points inside the ellipse. Three trajectories shown as dashed lines starting from points in K_0 and ending with points in $T_\varphi(1.5, K_0)$ are also depicted.

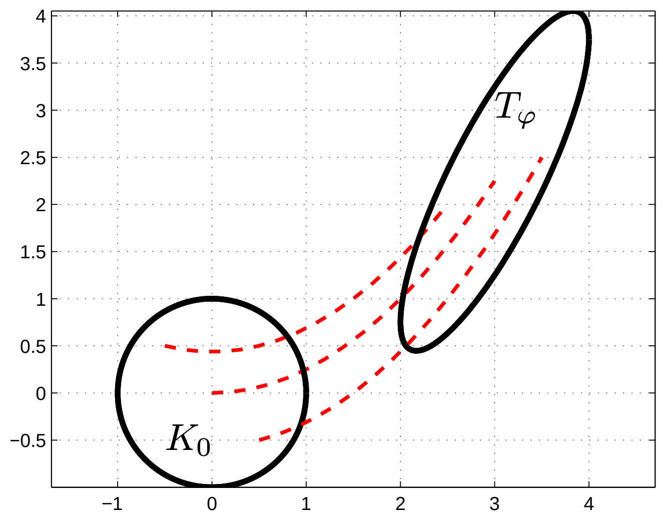

Figure 4.3 Illustration of the transition set

4.2.2 Mutation Equations

The transitions can be used to extend the time derivative of a function in the vector space to the time derivative of a tube in a general metric space. In the vector space, the time derivative for a function $f(t) : \mathbb{R}_{\geq 0} \mapsto \mathbb{R}^n$ is defined as $v = \lim_{\Delta t \to 0}[f(t + \Delta t) - f(t)]/\Delta t$. This definition can be transformed to the first order approximation form, where the time derivative v for $f(t)$ should satisfy [119]:

$$\lim_{\Delta t \to 0} \frac{1}{\Delta t} ||f(t + \Delta t) - (f(t) + v\Delta t)|| = 0 \tag{4.5}$$

where $f(t) + v\Delta t$ can be considered as a new point in $\mathbb{R}^n$ obtained by starting from $f(t)$ and moving along the direction v after Δt time. Similarly, in the metric space $(\mathcal{P}(E), \mathcal{D})$, transition $T_\varphi(\Delta t, K(t))$ can be considered as a new set in $\mathcal{P}(E)$ obtained by starting from $K(t)$ and moving along the 'direction' of $\varphi \in \mathrm{BL}(E, \mathbb{R}^n)$ after Δt time. Therefore, similar to Eq. (4.5), φ satisfies the first order approximation of a tube $K(t)$ if:

$$\lim_{\Delta t \to 0^+} \frac{1}{\Delta t} \mathcal{D}(K(t + \Delta t), T_\varphi(\Delta t, K(t))) = 0 \tag{4.6}$$

where $K(t+\Delta t)$ is the set at time $t+\Delta t$ according to the tube $K(t) : \mathbb{R}_{\geq 0} \mapsto \mathcal{P}(\mathbb{R}^n)$. Based on such an analogy from the vector space to the non-vector space, the derivative for a tube called mutation can be defined. Since there may be none or multiple φ satisfying Eq. (4.6) for a given tube, the mutation is a set defined as follows:

Definition 3 *The mutation of a tube $K(t)$, denoted as $\overset{\circ}{K}(t)$, is defined as the set of all*

$\varphi \in BL(E, \mathbb{R}^n)$ *such that Eq. (4.6) is satisfied:*

$$\overset{\circ}{K}(t) = \{\varphi(x) \in BL(E, \mathbb{R}^n) : \textit{Eq. (4.6) is satisfied}\} \tag{4.7}$$

Based on the mutation of a tube, mutation equations in the non-vector space, the analogy to differential equations in the vector space, can be defined as follows:

Definition 4 *For a given function* $f : \mathcal{P}(E) \mapsto BL(E, \mathbb{R}^n)$ *mapping from a tube to a bounded Lipschitz function, the mutation equation for the tube is defined as:*

$$f(K(t)) \in \overset{\circ}{K}(t) \quad \textit{with} \quad K(0) = K_0 \tag{4.8}$$

The solution to the mutation equation is the tube $K(t)$ such that the function $f(K(t)) \in BL(E, \mathbb{R}^n)$ satisfies Eq. (4.6) at Lebesgue-almost every time.

A special case of the general mutation equation is the one induced by differential equations. Let $\dot{x}(t) = \varphi(x(t))$ with $\varphi(x(t)) \in \mathrm{BL}(E, \mathbb{R}^n)$, then the transition $T_\varphi(t, K_0)$ can be considered as a tube $K(t)$ starting from K_0. In this case, Eq. (4.6) is automatically satisfied because $K(t + \Delta t) = T_\varphi(\Delta t, K(t))$. Therefore, the mutation equation for this case is $\varphi(x(t)) \in \overset{\circ}{K}(t)$.

Since the tube $K(t)$ is induced from $\varphi(x(t))$, it is tempted to write $\varphi(x(t)) = \overset{\circ}{K}(t)$. This is wrong because there may exist other bounded Lipschitz functions in $\overset{\circ}{K}(t)$ except $\varphi(x(t))$. For example, a stationary tube $K(t) = \{x \in \mathbb{R}^2 : ||x|| \leq 1\}$ can be considered as being induced from $\varphi = [0, 0]^{\mathrm{T}}$ with $K(0) = \{x \in \mathbb{R}^2 : ||x|| \leq 1\}$. Nevertheless, $\varphi' = [x_2, -x_1]^{\mathrm{T}}$

also satisfies $\varphi' \in \overset{\circ}{K}(t)$. This can be seen by solving the ODE as:

$$x_1 = \sqrt{x_1(0)^2 + x_2(0)^2}\sin[t + \arctan(x_1(0)/x_2(0))]$$
$$x_2 = \sqrt{x_1(0)^2 + x_2(0)^2}\cos[t + \arctan(x_1(0)/x_2(0))]$$

where $x_1(0)$ and $x_2(0)$ are the initial conditions. From the solution, any trajectory starting from $x_1(0)$ and $x_2(0)$ will stay on the circle $x_1(t)^2 + x_2(t)^2 = x_1(0)^2 + x_2(0)^2$. Therefore, the transition $T_\varphi(\Delta t, K(t))$ will be the same as $K(t)$, which indicates $\varphi' = [x_2, -x_1]^{\mathrm{T}}$ is also in the set $\overset{\circ}{K}(t)$.

The mutation equation defined in Eq. (4.8) can be modified to add the control input to the equation. Consider a map $f : \mathcal{P}(E) \times U \mapsto \mathrm{BL}(E, \mathbb{R}^n)$ where U is the set of all possible controls u. Then the controlled mutation equation can be defined as:

$$f(K(t), u(t)) \in \overset{\circ}{K}(t) \quad \text{with} \quad u(t) = \gamma(K(t)) \tag{4.9}$$

where $\gamma : \mathcal{P}(E) \mapsto U$ is the feedback map from the current set $K(t)$ to the control input. Similar to the special case of mutation equation, if the tube is induced from a controlled differential equation $\varphi(x(t), u(t)) \in \mathrm{BL}(E, \mathbb{R}^n)$, then the controlled mutation equation can be written as $\varphi(x(t), u(t)) \in \overset{\circ}{K}(t)$ with $u(t) = \gamma(K(t))$.

4.3 Stabilization Control in the Non-vector Space

With the dynamics modeling in the non-vector space, the stabilization problem can be discussed. In this section, the problem will be formulated and the stabilizing controller design will be presented.

4.3.1 Stabilization Problem

Before the design of the stabilizing controller, the stability in the non-vector space $(\mathcal{P}(E), \mathcal{D})$ should be defined. Similar to equilibrium points, the equilibrium set for mutation equation $f(K(t)) \in \overset{\circ}{K}(t)$ is defined as a set $\hat{K} \subset E$ such that $f(\hat{K}) = 0$. Based on the metric $\mathcal{D}$, the stability for a mutation equation around an equilibrium set can be defined similarly to equilibrium points in the vector space [121].

Definition 5 *Suppose in $(\mathcal{P}(E), \mathcal{D})$, the mutation equation $f(K(t)) \in \overset{\circ}{K}(t)$ with $f : \mathcal{P}(E) \mapsto BL(E, \mathbb{R}^n)$ and $K(0) = K_0$ has an equilibrium set $\hat{K} \subset E$. Then*

- *$\hat{K}$ is stable if for any $\varepsilon > 0$, there exists $\delta = \delta(\varepsilon) > 0$ such that*

$$\mathcal{D}(K_0, \hat{K}) < \delta \Longrightarrow \mathcal{D}(K(t), \hat{K}) < \varepsilon$$

- *$\hat{K}$ is unstable if it is not stable*

- *$\hat{K}$ is asymptotically stable if it is stable and there exists δ such that*

$$\mathcal{D}(K_0, \hat{K}) < \delta \Longrightarrow \lim_{t \to \infty} \mathcal{D}(K(t), \hat{K}) = 0$$

- *$\hat{K}$ is exponentially stable if there exist positive constants c, k, and λ such that:*

$$\mathcal{D}(K(t), \hat{K}) \leq k\mathcal{D}(K_0, \hat{K})e^{-\lambda t}, \forall \hat{K} \text{ with} \mathcal{D}(K_0, \hat{K}) < c$$

In the above definitions, the general norm in the vector space is replaced by the metric distance between $K(t)$ and $\hat{K}$. Based on the definitions, the stabilization problem for the controlled mutation equation (4.9) can be formulated.

Stabilization Problem: Assume a system in $(\mathcal{P}(E), \mathcal{D})$ is described by the controlled mutation equation $f(K(t), u(t)) \in \overset{\circ}{K}(t)$ with an initial set K_0. Given a goal set $\hat{K}$ in the neighborhood of K_0, design a feedback controller $u(t) = \gamma(K(t))$ based on the current set $K(t)$ such that $\hat{K}$ is stable, asymptotically stable, or exponentially stable.

The above stabilization problem cannot be addressed using existing theories in the vector space due to the lack of linear structure in the non-vector space. Nevertheless, the Lyapunov theory, if properly extended to the non-vector space, can be adopted for the stability analysis of a given system.

4.3.2 Lyapunov Function Based Stability Analysis

Since the state in the non-vector space is a set, the Lyapunov function is a function of sets instead of vectors. Such functions are also called shape functionals in the shape optimization [122]. To deal with the functionals, the Lyapunov function can be defined as bounded by a given real valued function stated as follows:

Definition 6 *For the system $f(K(t)) \in \overset{\circ}{K}(t)$ with $K(0) = K_0$ and an equilibrium set $\hat{K}$, let $V : \mathcal{P}(E) \mapsto \mathbb{R}_{\geq 0}$ be a shape functional, and $\phi : \mathbb{R} \mapsto \mathbb{R}$ be a continuous function. Then V is a ϕ-Lyapunov function for the system if the following two conditions are satisfied:*

- *$V(\hat{K}) = 0$ and $V(K(t)) > 0$ for $K(t) \neq \hat{K}$;*
- *$V(K(t)) \leq h(t)$, $\forall\, t \geq 0$ with $V(K_0) = h(0)$, where $h(t)$ is the solution to the differential equation $\dot{h} = \phi(h)$.*

From the above definition, we see that if $h(t)$ converges to zero, then $V(K(t))$ will also converge to zero. $V(K(t))$ represents the trajectory along the solution tube $K(t)$. Note that a similar definition exists in [123]; however, our definition incorporates the equilibrium set in order to discuss the stability problem systematically. With the definition of the Lyapunov function, the stability of the system in the non-vector space can be determined as stated in the following theorem:

Theorem 2 *For the system $f(K(t)) \in \overset{\circ}{K}(t)$ with $K(0) = K_0$ and an equilibrium set $\hat{K}$, if there exists a continuous function $\phi : \mathbb{R} \mapsto \mathbb{R}$ and the corresponding ϕ-Lyapunov function $V : \mathcal{P}(E) \mapsto \mathbb{R}_{\geq 0}$. Without loss of generality, let the equilibrium point for $\dot{h} = \phi(h)$ be zero, then $\hat{K}$ is*

- *stable if zero is stable for $\dot{h} = \phi(h)$;*
- *asymptotically stable if zero is asymptotically stable for $\dot{h} = \phi(h)$;*
- *exponentially stable if zero is exponentially stable for $\dot{h} = \phi(h)$.*

Proof: *Let $\mathcal{D}((K(t), \hat{K}) = |V(K(t)) - V(\hat{K})| = |V(K(t))|$. If $\hat{K}$ is fixed, then one can verify that such a definition satisfies the three metric properties. Therefore, it can be used as a metric in Definition 5 for the proof.*

Stability: for any $\varepsilon > 0$, by the stability of zero for $\dot{h} = \phi(h)$, there exists $\delta(\varepsilon) > 0$ such that $|h(0)| < \delta \Longrightarrow |h(t)| < \varepsilon$. With the same δ, we have $\mathcal{D}(K(t), \hat{K}) = |V(K(t))| = V(K(t)) \leq h(t) < \varepsilon$ for $\mathcal{D}(K_0, \hat{K}) = |V(K_0)| = |h(0)| < \delta$.

Asymptotical stability: by the asymptotical stability of zero for $\dot{h} = \phi(h)$, there exists $\delta > 0$ such that $|h(0)| < \delta \Longrightarrow \lim_{t\to\infty} |h(t)| = 0$. With the same δ, we have $\lim_{t\to\infty} \mathcal{D}(K(t), \hat{K}) = \lim_{t\to\infty} |V(K(t))| \leq \lim_{t\to\infty} |h(t)| = 0$. Therefore, we have $\lim_{t\to\infty} \mathcal{D}(K(t), \hat{K}) = 0$ for $\mathcal{D}(K_0, \hat{K}) = |V(K_0)| = |h(0)| < \delta$.

Exponential stability: by the exponential stability of zero for $\dot{h} = \phi(h)$, there exist positive constants k and λ such that $|h(t)| = k|h(0)|e^{-\lambda t}$ for any $|h(0)| < c$. With the same k

and λ*, we have* $\mathcal{D}(K(t), \hat{K}) = V(K(t)) \leq h(t) = k|h(0)|e^{-\lambda t} = k\mathcal{D}(K_0, \hat{K})e^{-\lambda t}$ *for any* $\mathcal{D}(K_0, \hat{K}) = |h(0)| < c$*.*

With the above theorem, the next question is how to find or construct the desired Lyapunov function. The answer to this question requires the definition of derivative for shape functionals.

Definition 7 *[122] Given a shape functional* $V : \mathcal{P}(E) \mapsto \mathbb{R}$*, a set* $K \in \mathcal{P}(E)$*, and a function* $\varphi \in BL(E, \mathbb{R}^n)$*. Then* V *has a Eulerian semiderivative* $\overset{\circ}{V}_{\varphi}(K)$ *at* K *in the direction of* φ *if*

$$\lim_{\Delta t \to 0^+} \frac{V(T_{\varphi}(\Delta t, K)) - V(K)}{\Delta t}$$

exists and is finite.

Note that the definition is similar to the derivative for a function in the vector space because $T_{\varphi}(\Delta t, K)$ is a new set starting from K in the direction φ after Δt time. With this definition, the Lyapunov functions in the non-vector space can be characterized by the following theorem:

Theorem 3 *[123] Consider a map* $f : \mathcal{P}(E) \mapsto BL(E, \mathbb{R}^n)$*. Let* $V : \mathcal{P}(E) \mapsto \mathbb{R}_{\geq 0}$ *be a shape functional which has a Eulerian semiderivative in the direction of* $f(K)$*. Assume* $\phi : \mathbb{R} \mapsto \mathbb{R}_{\geq 0}$ *be a continuous function. Then* V *is a* ϕ*-Lyapunov function if and only if:*

$$\overset{\circ}{V}_{f(K)}(K) \leq \phi(V(K)) \tag{4.10}$$

for any K *in the domain of* V*.*

The proof of this theorem can be found in [123]. This theorem can be applied to the controlled mutation equation to design stabilizing controllers. The general procedure is similar to the case in the vector space. First of all, a Lyapunov function candidate is found, which can be the distance function between two sets. Then the shape directional derivative for the Lyapunov function is obtained. Finally, a controller can be designed to satisfy the inequality (4.10). Depending on the function ϕ for the Lyapunov function, the stability, asymptotical stability, or exponential stability can be guaranteed.

4.3.3 Stabilizing Controller Design

With the Lyapunov theory in the non-vector space, the stabilization controller can be designed for the system with image feedback described by the controlled mutation equation Eq. (4.9). In this sub section, we consider a more general case corresponding to the time invariant linear system. In this case, the mutation equation is induced from the differential equation $\dot{x} = Ax + Bu$ with $x \in \mathbb{R}^n$, $u \in \mathbb{R}^m$, $A \in \mathbb{R}^{n\times n}$, and $B \in \mathbb{R}^{n\times m}$. Therefore, the controlled mutation equation is $Ax + Bu \in \overset{\circ}{K}$. Note that the time t is omitted for clear presentation. For such a system, the following Lyapunov function candidate can be used [117]:

$$V(K) = \frac{1}{2}\int_K d^2_{\hat{K}}(x)dx + \frac{1}{2}\int_{\hat{K}} d^2_K(x)dx \tag{4.11}$$

With such a candidate, the first condition required for a Lyapunov function in Definition 2 can be verified. For the second condition, the controller should be designed for the verification. In fact, a stabilizing controller can be designed as stated in the following theorem:

Theorem 4 *For the system $Ax + Bu \in \overset{\circ}{K}(t)$ with $x \in \mathbb{R}^n$, $u \in \mathbb{R}^m$, $A \in \mathbb{R}^{n\times n}$, $B \in \mathbb{R}^{n\times m}$, and $K \subset \mathbb{R}^n$, the exponential stability for a given desired set $\hat{K}$ can be achieved by the* *following controller:*

$$u = -E(K)(\alpha V(K) + \frac{H(K)}{||E(K)||^2}) \tag{4.12}$$

where $\alpha > 0$ is a gain factor. $H(K)$ is a scalar and $E(K) \in \mathbb{R}^m$ is column vector defined by:

$$H(K) = \frac{1}{2}\int_K [d^2_{\hat{K}}(x) trace(A) + (Ax)^{\mathrm{T}}(x - P_{\hat{K}}(x))]dx - \int_{\hat{K}} (AP_K(x))^{\mathrm{T}}(x - P_K(x))dx$$
$$E(K) = B^{\mathrm{T}}[\int_K (x - P_{\hat{K}}(x))dx - \int_{\hat{K}} (x - P_K(x))dx]$$

where trace(A) is the trace for matrix A.

Note that the time t is also omitted for clear presentation. To prove this theorem, the following two lemmas for the Eulerian semi-derivative of the two components in the Lyapunov function candidate are needed.

Lemma 1 *[117] For a function $\varphi \in BL(E, \mathbb{R}^n)$, the Eulerian semiderivative for $V^1 = \frac{1}{2}\int_K d^2_{\hat{K}}(x)dx$ at K in the direction of φ is:*

$$\overset{\circ}{V}{}^1_{\varphi}(K) = \int_K [\frac{1}{2} d^2_{\hat{K}}(x) div(\varphi) + \varphi(x)^{\mathrm{T}}(x - P_{\hat{K}}(x))]dx$$

where div$(\cdot)$ is the divergence of a function.

Lemma 2 *[117] For a function $\varphi \in BL(E, \mathbb{R}^n)$, the Eulerian semiderivative for $V^2 = \frac{1}{2}\int_{\hat{K}} d^2_K(x)dx$ at K in the direction of φ is:*

$$\overset{\circ}{V}{}^2_{\varphi}(K) = \int_{\hat{K}} -\varphi(P_K(x))^{\mathrm{T}}(x - P_K(x))dx$$

Proof of Theorem 4: *The proof of this theorem is based on theorem 2, theorem 3, and* *the previous two lemmas. Let $\varphi = Ax + Bu$, then with the above two lemmas, we have:*

$$
\begin{aligned}
\mathring{V}_\varphi(K) =& \mathring{V}^1_\varphi(K) + \mathring{V}^2_\varphi(K) \\
=& \frac{1}{2}\int_K [d^2_{\hat{K}}(x) trace(A) + (Ax)^{\mathrm{T}}(x - P_{\hat{K}}(x))]dx - \int_{\hat{K}} (AP_K(x))^{\mathrm{T}}(x - P_K(x))dx + \\
& u^{\mathrm{T}}B^{\mathrm{T}}[\int_K (x - P_{\hat{K}}(x))dx - \int_{\hat{K}} (x - P_K(x))dx] \\
=& H(K) + u^{\mathrm{T}}E(K)
\end{aligned}
$$

Therefore, if $u = -E(K)(\alpha V(K) + H(K)/||E(K)||^2)$, then $\mathring{V}_\varphi(K) = -\alpha||E(K)||^2 V(K)$. From theorem 3, $V(K)$ is a Lyapunov function for $\phi(h) = -\beta h$ with β a constant satisfying $0 < \beta \leq \alpha||E(K)||^2$. Based on theorem 2, the exponential stability can be achieved since the equilibrium point zero for $\dot{h} = \phi(h) = -\beta h$ is exponential stable.

4.4 Application to Visual Servoing

The visual servoing problem can be modeled by the special system in the Theorem 4, and the controller can be readily applied. In fact, for servoing with grey scale images, each pixel can be represented by a three dimensional vector $x = [x_1, x_2, x_3]^{\mathrm{T}}$ where x_1 and x_2 are the pixel indices, and x_3 the pixel intensity. For a general visual servoing problem, the control input is the camera's spatial velocity. Therefore, the control input $u(t)$ has three translational components and three rotational components, which can be represented by a vector $u(t) = [v_x, v_y, v_z, \omega_x, \omega_y, \omega_z]^{\mathrm{T}}$.

The system in Theorem 4 is determined by $\varphi(x)$, which is further determined by the relationship between $u(t)$ and $x(t)$. The perspective projection sensing model in computer vision can be used to derive such a relationship. Under constant lighting condition, x_3 will be a constant for each pixel; therefore, $\dot{x}_3 = 0$. With a unit camera focal length, a 3D point with coordinates $P = [p_x,\, p_y,\, p_z]^T$ in the camera frame will be projected to the image plane with coordinates:

$$x_1 = p_x/p_z \qquad x_2 = p_y/p_z \tag{4.13}$$

Based on these equations, the relation between $u(t)$ and $x(t)$ can be obtained as:

$$\dot{x}(t) = L(x(t))u(t) \tag{4.14}$$

where

$$L = \begin{bmatrix} -1/p_z & 0 & x_1/p_z & x_1x_2 & -(1+x_1^2) & x_2 \\ 0 & -1/p_z & x_2/p_z & 1+x_2^2 & -x_1x_2 & -x_1 \\ 0 & 0 & 0 & 0 & 0 & 0 \end{bmatrix}$$

Note that first two rows are the same as the interaction matrix in visual servoing [78]. In Eq. (4.14), $\dot{x}(t) = \varphi(x(t), u(t)) = L(x(t))u(t)$ is linear in u; therefore, the controller in Eq. (4.12) can be applied by letting $A = 0$ and consider B as a non-constant. Specifically, we have the following theorem

Theorem 5 *[112] For the system described by the following set dynamics*

$$\varphi(z(t), u(t)) = L(z(t))u(t) \in \overset{\circ}{K}(t) \quad \textit{with} \quad K(0) = K_0 \tag{4.15}$$

where $L(z(t)) \in \mathbb{R}^{p\times q}$, $z(t) \in K(t) \subset \mathbb{R}^p$, $u(t) \in \mathbb{R}^q$, and $\varphi(z(t), u(t)) \in BL(E, \mathbb{R}^p)$, the following controller can locally asymptotically stabilize it at a desired set $\hat{K}$:

$$u = \gamma(K) = -\alpha D(K)^+ \tag{4.16}$$

where $\alpha \in \mathbb{R}_{>0}$ is a gain factor, and $D(K)^+$ is the Moore-Penrose pseudoinverse of $D(K)$, which is a column vector

$$D(K) = \frac{1}{2}\int_K d_{\hat{K}}^2(z)(\sum_{i=1}^{p}\frac{\partial L_i}{\partial z_i})^{\mathrm{T}}dz + \int_K L(z)^{\mathrm{T}}(z - P_{\hat{K}}(z))dz - \int_{\hat{K}} L(P_K(\hat{z}))^{\mathrm{T}}(\hat{z} - P_K(\hat{z}))d\hat{z} \tag{4.17}$$

where L_i $(i = 1, 2, \ldots, p)$ is the i-th row vector in matrix L, and $\partial L_i/\partial z_i$ is also a row vector with the same dimension.

The preliminary experiments for two cases will be carried out to verify the controller in the experimental part. For easy implementation, the simplified controllers for these two cases will be obtained.

4.4.1 3D Translation

In this case, the camera can only perform the translational motion. The row vector $D(K)$ can be simplified to:

$$\begin{aligned} D(K) = &\int_K \frac{1}{p_z}[0,\, 0,\, d_{\hat{K}}^2(x)]dx + \int_K \frac{1}{p_z}(x - P_{\hat{K}}(x))^{\mathrm{T}}L(x)dx \\ &- \int_{\hat{K}} \frac{1}{p_z}(x - P_K(x))^{\mathrm{T}}L(P_K(x))dx \end{aligned} \tag{4.18}$$

with

$$L(x) = \begin{bmatrix} -1 & 0 & x_1 \\ 0 & -1 & x_2 \\ 0 & 0 & 0 \end{bmatrix}$$

In general, p_z varies with different x in the set K. A special case is when the observed object is planar, then p_z will be the same for all $x \in K$, and it can be taken out from the integral.

In this case, although p_z will change during the translation along the optical axis, it only effects the magnitude of $u(t)$. Therefore, we can assume p_z to be one.

4.4.2 SE(2) Motion

In this case, the camera has three degree-of-freedom (DOF). In addition to 2D translational movement, it can also rotate about its optical axis. The row vector $D(K)$ can be simplified to:

$$D(K) = \int_K (x - P_{\hat{K}}(x))^{\mathrm{T}} L(x) dx - \int_{\hat{K}} (x - P_K(x))^{\mathrm{T}} L(P_K(x)) dx \tag{4.19}$$

with

$$L(x) = \begin{bmatrix} -1/p_z & 0 & x_2 \\ 0 & -1/p_z & -x_1 \\ 0 & 0 & 0 \end{bmatrix}$$

Note that p_z will be a constant if a planar object is used.

4.5 Testing Results

Although the ideal case is to use the tailed jumping robot for experimental results, as our initial step to validate the non-vector space control theory, we apply the approach to robotic manipulators [112]. Note that this approach has been also verified using atomic force microscope images [111].

The detail experimental framework is shown in Fig. 4.4, which is the general look-and-move structure [124]. First of all, the non-vector space controller generates a camera velocity based on the current image from the camera and the goal image. This velocity is resolved into the joint speeds via the inverse velocity kinematics. Then the robot executes this speed through the robot controller until a new joint speed command is received. Note that we use an eye-in-hand configuration with the camera attached to the manipulator's end-effector.

The key step in Fig. 4.4 is the inverse velocity kinematics, which is well discussed in standard robotics textbooks for a six DOF manipulator [125]. Nevertheless, we will use a seven DOF manipulator to provide flexibility and capacity by its redundancy. In this case, the redundancy resolution requires extra efforts which will be briefly described in this section.

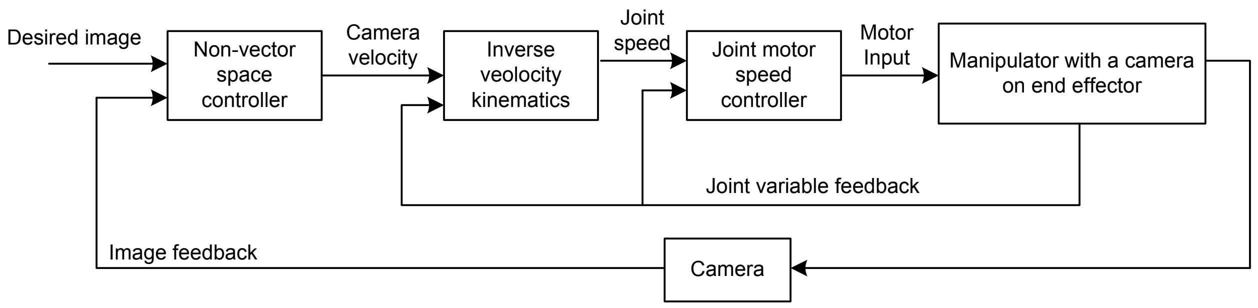

Desired image
Non-vector space controller
Camera velocity
Inverse veolocity kinematics
Joint speed
Joint motor speed controller
Motor Input
Manipulator with a camera on end effector
Joint variable feedback
Image feedback
Camera

Figure 4.4 The implementation framework to verify the non-vector space controller

The LWA3 redundant manipulator with seven revolute joints from Schunk is used for experiment. In order to resolve the redundancy, an extra variable is introduced. It is named arm angle and denoted by ϕ. It represents the configuration of the plane constructed by the elbow-shoulder link and elbow-wrist link with respect to the shoulder-wrist axis [126]. Let $\xi_{ee} \in \mathbb{R}^6$ be vector for the three linear and three angular velocities of the end-effector. Let $\theta \in \mathbb{R}^7$ denote the seven joint angles of the manipulator. Then ξ_{ee} and $\dot{\theta}$ has the following relationship:

$$\xi_{ee} = J_{ee}(\theta)\dot{\theta} \tag{4.20}$$

where $J_{ee}(\theta) \in \mathbb{R}^{6\times 7}$ is the Jacobian matrix of the end-effector. The arm angle ϕ introduced earlier is related to the seven joint angles by:

$$\dot{\phi} = J_{\phi}(\theta)\dot{\theta} \tag{4.21}$$

where $J_{\phi}(\theta) \in \mathbb{R}^{1\times 7}$ can be considered as the Jacobian matrix of the arm angle.

Eqs. (4.20) and (4.21) can be combined together to obtain:

$$Y \triangleq \begin{bmatrix} \xi_{ee} \\ \dot{\phi} \end{bmatrix} = \begin{bmatrix} J_{ee}(\theta) \\ J_{\phi}(\theta) \end{bmatrix} \dot{\theta} = J(\theta)\dot{\theta} \tag{4.22}$$

where $J(\theta) \in \mathbb{R}^{7\times 7}$ is the augmented Jacobian matrix of the full configuration. Since $J(\theta)$ is a square matrix, a unique velocity for the seven joints can be obtained if $J(\theta)$ is nonsingular. In this way, the redundancy problem is solved.

With above redundancy resolution, we can obtain the joint speed given the end-effector's velocity in the end-effector frame. But the output of the non-vector space controller is the velocity of the camera in the camera frame. Therefore, the transformation from the camera frame to the end-effector frame should be derived. Denote the camera velocity with $\xi_c \in \mathbb{R}^6$. Then we have

$$\xi_{ee} = J_{ce}\xi_c \tag{4.23}$$

where $J_{ce} \in \mathbb{R}^{6\times 6}$ is the transformation matrix which can be obtained once the spatial relationship between the camera and end-effector is known [125]. From Eqs. (4.22) and (4.23), the relationship between the joint velocity and the camera velocity is:

$$\bar{Y} \triangleq \begin{bmatrix} \xi_c \\ \dot{\phi} \end{bmatrix} = \begin{bmatrix} J_{ce}^{-1} J_{ee}(\theta) \\ J_{\phi}(\theta) \end{bmatrix} \dot{\theta} = \bar{J}(\theta)\dot{\theta} \tag{4.24}$$

where $\bar{J}(\theta) \in \mathbb{R}^{7\times 7}$ is the augmented Jacobian matrix of the new full configuration. Because the manipulator has seven DOF, the three position and three orientation movements of the camera are all achievable. Therefore, we can let camera's velocity be the output of the non-vector based controller:

$$\xi_c = u(t) \tag{4.25}$$

To achieve this output, the joint velocities of the manipulator can be obtained by the inverse velocity kinematics of Eq. (4.24):

$$\dot{\theta} = \bar{J}^{-1}(\theta)\bar{Y} \tag{4.26}$$

where the velocities of the camera are obtained from Eq. (4.25). The velocity of the arm angle is determined by the online sensors for obstacle avoidance of the manipulator links [127]. Then the joint velocities are executed by the joint motors based on joint motor speed controllers.

To validate the non-vector space controller, experiments are conducted on the LWA3 redundant manipulator. The experimental setup is shown in Fig. 4.5, where an ordinary CMOS camera is rigidly attached to the end-effector. As our preliminary experiment, a planar object with a rectangle, a circle, and a triangle printed on a white paper is placed on the ground. Note that although planar geometric shapes are used, no image feature extraction and tracking are performed in the experiments.

As the quality of the CMOS camera is poor, the image noise can be quite large. For example, with two consecutive images obtained with a still camera looking at a still environment, the variation of image intensities may be up to 12%. To address this issue, we convert grey scale images to binary images for our experiment. A 120×160 grey scale im-

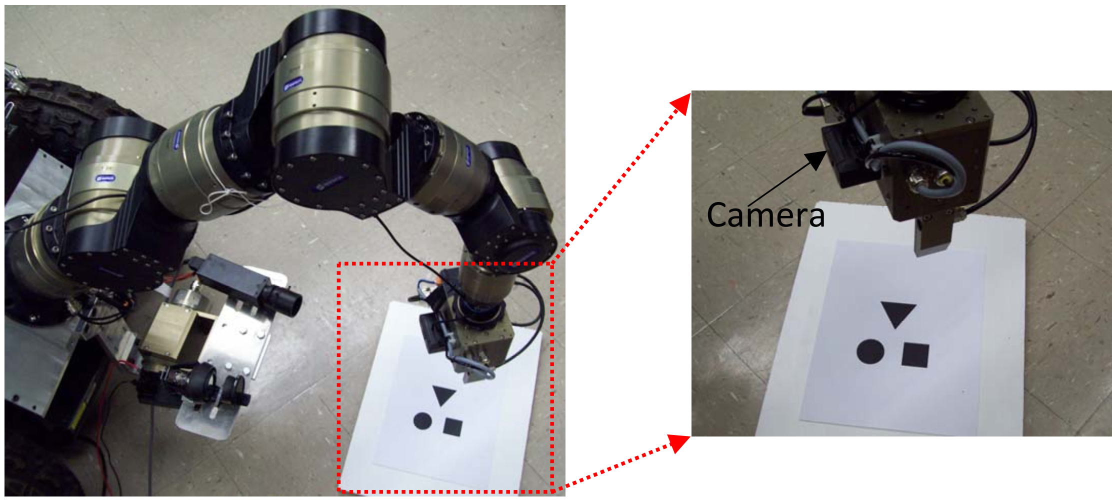

Figure 4.5 Experimental setup to verify the non-vector space controller

age is obtained, then it is converted to a binary image to retain the geometric shapes. The camera is calibrated, and the following intrinsic parameters are found: focal lengths in pixels $f_x = f_y = 204$ and principle points in pixels $u_r = 48$, and $u_c = 92$.

Experiments for two subsets of rigid motion discussed are carried out. The general process for the experiments is as follows. First of all, the manipulator is moved to a desired position, where a desired image is acquired. The desired position is obtained using the manipulator's forward kinematics. Then the manipulator is moved to some initial position, where the initial image is recorded. Then the manipulator will start moving according to the framework in Fig. 4.4. During the movement, the manipulator end-effector's positions are recorded with 5Hz frequency. In this way, the error trajectory can be obtained after the experiment.

4.5.1 3D Translational Motion

In this experiment, the manipulator is allowed to move in all the three translational directions. Four experiments are carried out, and the detail of one experiment is shown in Fig. 4.7. The meaning for each figure is the same to the 2D translation case. As discussed

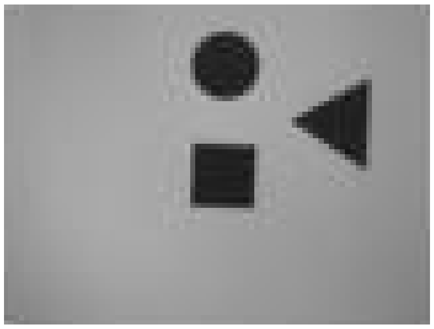
(a) Desired Image

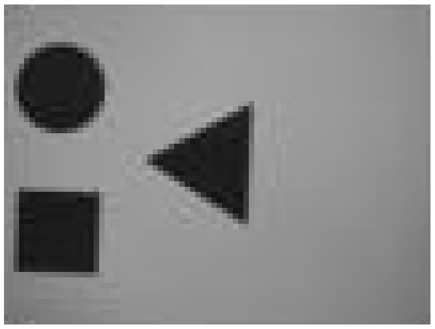
(b) Initial Image

Figure 4.6 Initial and desired image for the 3D translation

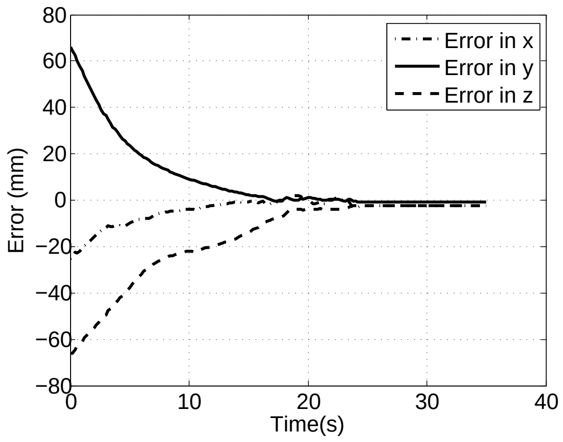

(a) Error in the task space

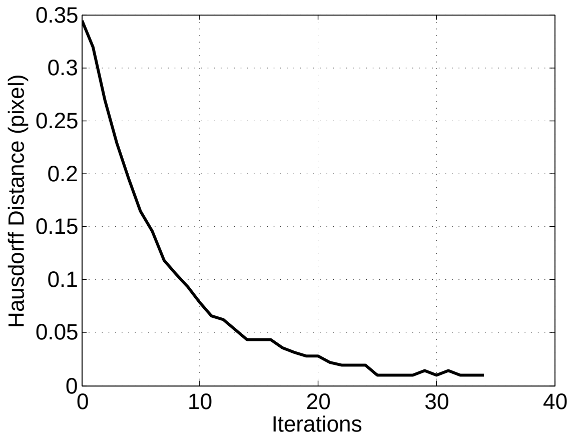

(b) Hausdorff distance

Figure 4.7 Experimental results for the 3D translation

before, we can use a constant depth p_z in the controller for planar objects. From the results, we see that the controller can make the manipulator move to the desired position.

Table 4.1 Results for 3D translation

Trial No.		1	2	3	4	average
Final Error	x (mm)	2.4	2.1	2.5	1.3	2.1
	y (mm)	0.8	1.9	1.5	2.9	1.8
	z (mm)	2.1	3.3	0.1	0.6	1.5

The final errors in three directions for the four experiments are shown in table 4.1. The average errors are also computed, and the results show performance similar to the 2D translation case.

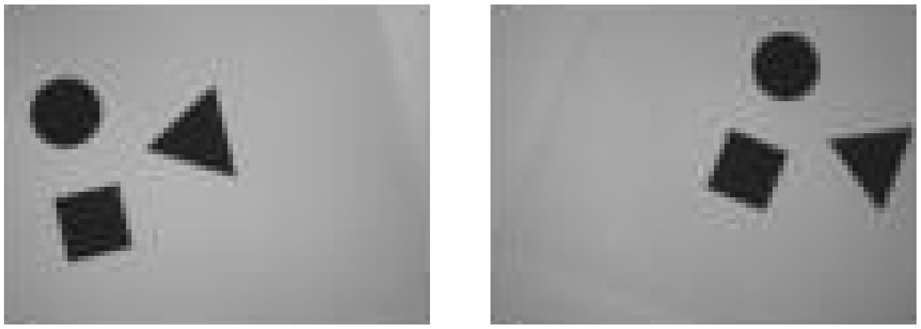
(a) Desired Image (b) Initial Image

Figure 4.8 Initial and desired image for the SE(2) motion

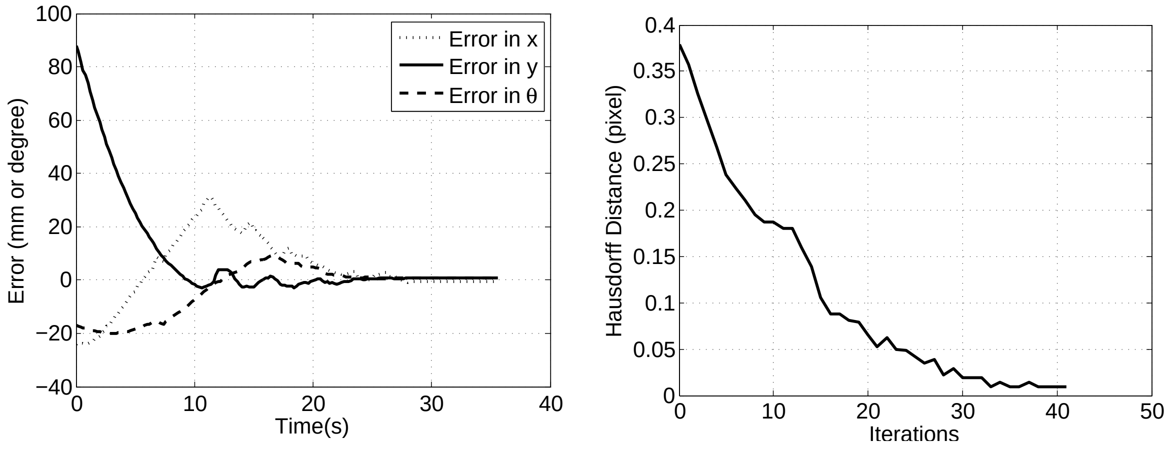

(a) Error in the task space (b) Hausdorff distance

Figure 4.9 Experimental results for the SE(2) motion

4.5.2 SE(2) Motion

In this experiment, the manipulator can perform the 2D translation and a rotation about its optical axis. Four experiments are conducted, and one result is shown in Fig. 4.9. Note that the rotation error is also plotted in Fig. 4.9(a) with degree as the unit. From the plot, there are some overshoots for the system, but the controller can still stabilize the system at the desired position.

The final errors for the four experiments are shown in table 4.2, where the unit for the rotation is degree. From the table, we see that the error in rotation is quite small.

Table 4.2 Results for SE(2) motion

Trial No.		1	2	3	4	average
Final Error	x (mm)	1.7	1.0	0.8	0.7	1.1
	y (mm)	0.4	2.7	2.7	0.7	1.6
	θ (°)	0.01	0.32	0.41	0.83	0.39

4.6 Conclusions

In this chapter, a bio-inspired non-vector space approach is presented. The control method formulates the system dynamics in the space of sets. Due to the lack of linear structure in such a space, new tools from the mutational analysis are employed. The Lyapunov theory can also be extended in such a space. Based on the dynamics and Lyapunov theory, the stabilization problem is proposed and a stabilizing controller is designed for a general system. The designed controller is applied to vision based control. The testing results using a redundant robotic manipulator demonstrate the effectiveness of the controller to steer the current image set to a desired image set.

Chapter 5

Compressive Feedback based Non-vector Space Control

5.1 Introduction

Although the non-vector space control approach discussed in the previous chapter can be used for vision based control of robot's landing postures, the vision feedback from vision sensor has a large amount of data, which cannot be handled by meso-scale robots such as the tailbot, which has a limited computation power [88].

We can alleviate this problem by reducing the number of samples. A smaller number of samples, however, may lose information in the original image. This problem can be addressed by the recently breakthrough in signal processing: the compressive sensing. In essence, instead of sampling the entire signal, compressive sensing directly samples the signal in its compressed form. In this way, the number of samples can be drastically reduced compared to the original image size. After the sampling, the original image can be recovered using advanced optimization algorithms [128].

In previous works, the compressive sensing and non-vector space control are discussed separately in signal processing and control society, respectively. In this chapter, we propose the idea of compressive feedback. Furthermore, we aim to apply the compressive feedback to the non-vector space control approach: the compressive feedback based non-vector space control method [129]. In other words, we directly used the compressive feedback as the input to the non-vector space controller to achieve the control goal. The general structure of the proposed method is shown in Fig. 5.1. A reference input (goal set) is given in the form of compressive representation. Then based on the current compressive feedback, the non-vector space controller will generate a control signal to correct the error between the compressive goal set and the compressive feedback.

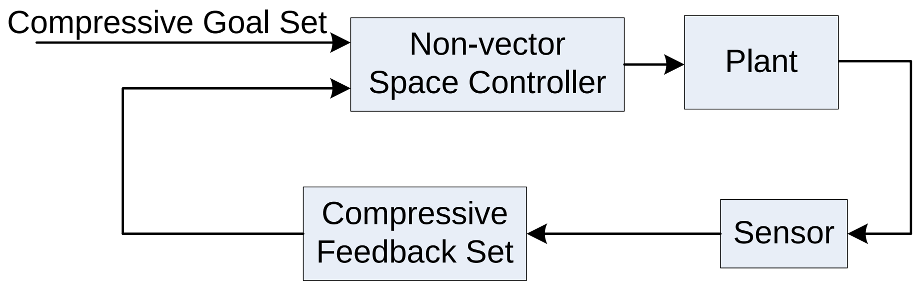

Figure 5.1 Schematic for non-vector space control with compressive feedback

The concept of compressive sensing has been introduced to control systems in recent years [129, 130]. The observability matrix is analyzed in the framework of compressive sensing and the observability and identification of linear system are discussed in [131] and [132]. The observability problem is also recently discussed in [133] for linear systems. With a different motivation, the compressive sensing is used to sparsify the system states, and then the recovered states are used for feedback [134]. The idea of sparsity is also employed in [135, 136] to solve the network control problem with rate-limited channels. However, all of the feedbacks used in these approaches are still regular state/output feedbacks. The only difference is that they are recovered from compressive sensing instead of direct sensing. In contrast, we intend to directly use the compressive data as the feedback without recovering.

The rest of this chapter is structured as follows. First of all, the mathematical preliminaries will be discussed in section 5.2, where the basics for compressive sensing are reviewed.

After that, the stabilizing controller design based on full feedback and compressive feedback are discussed in section 5.3. With the designed controller, the stability analysis is performed for sparse and approximate sparse feedback in section 5.4. Finally, applications to visual servoing for robotic manipulations are discussed in section 5.5.

5.2 Mathematical Preliminaries

The work presented in this chapter relies on the compressive sensing to develop compressive feedbacks. We review the basics for compressive sensing in this section.

The notations in this chapter are as follows. $\mathbb{R}$, $\mathbb{R}_{>0}$, and $\mathbb{R}_{\geq 0}$ represent the set of real, positive real, and nonnegative real numbers, respectively. $\mathcal{P}(\mathbb{R}^p)$ denotes the powerset of $\mathbb{R}^p$; that is, the collection of all the subsets in $\mathbb{R}^p$. Similarly, $\mathcal{P}(E)$, with $E \subset \mathbb{R}^p$, is the powerset of E. Unless otherwise stated, $||\cdot||$ denotes the Euclidean norm of a vector.

Compressive sensing is a new paradigm to acquire signals. Traditional signal acquisition methods sample the signal based on the Shannon-Nyquist theorem. After the sampling, the signal is compressed for storage or transmission. In contrast, the compressive sensing directly samples the signal in its compressed form [137]. Then it relies on convex optimization or greedy algorithms to recover the original signal. Again, we only include the essentials here for the sake of completeness, and a recent comprehensive introduction can be found in [138].

Suppose an unknown finite dimensional signal $x \in \mathbb{R}^n$ is sampled in the compressed form $y \in \mathbb{R}^m$ with $m \ll n$ through a measurement matrix $\Phi \in \mathbb{R}^{m\times n}$, that is

$$y = \Phi x \tag{5.1}$$

Then, x can be faithfully recovered from y using tractable numerical algorithms if x and Φ satisfy some general conditions, which we will elaborate in the following discussions.

For the original signal x, it should be sparse or approximately sparse, or have a sparse or approximately sparse representation in some basis. A vector $x \in \mathbb{R}^n$ is S-sparse if the number of nonzero elements of x is at most S. Denote all the S-sparse vectors by Ω_S

$$\Omega_S = \{x \in \mathbb{R}^n : \ ||x||_0 \leq S\}$$

where $||x||_0$ is the number of non-zero elements for x [138].

In some cases, $x \in \mathbb{R}^n$ may not be sparse itself but sparse in some orthonormal basis. Let $\Psi \in \mathbb{R}^{n \times n}$ be such a basis. In this case, x can be expanded in Ψ as follows

$$x = \Psi \overline{x}, \qquad \text{with} \qquad \overline{x} \in \Omega_S$$

The exact S-sparse, however, cannot be achieved in practical signals. In most situations, the signals can be well approximated by an S-sparse signal. The following definition quantifies such approximately sparse signals.

Definition 8 *The best S-sparse approximation for a vector $x \in \mathbb{R}^n$ is a vector $x_S \in \Omega_S$ such that*

$$||x - x_S|| \leq ||x - \hat{x}||, \quad \forall\, \hat{x} \in \Omega_S$$

Note that x_S can be obtained by retaining the S largest elements in x and setting the other elements to zero. If $||x - x_S||$ is small enough, then x is well approximated by x_S, and we say x is an approximately sparse signal.

If x is sparse or approximately sparse in some orthonormal basis Ψ, the compressive sensing problem can be written as

$$y = \Phi\Psi\overline{x} \tag{5.2}$$

Let $A = \Phi\Psi$, which is the new measurement matrix. With Eq. (5.2), the original signal can be obtained from $x = \Psi\overline{x}$ after $\overline{x}$ is recovered from y.

Besides the sparse requirement for the original signal, the measurement matrix should also satisfy some condition for recovering x from y in Eq. (5.1) or $\overline{x}$ from y in Eq. (5.2). One of such conditions is the restricted isometry property.

Definition 9 *A matrix $A \in \mathbb{R}^{m\times n}$ with $m < n$ satisfies the restricted isometry property (RIP) of order S if there exists a constant $\sigma_S \in (0,1)$ such that for any $x \in \Omega_S$, we have*

$$(1-\sigma_S)||x||^2 \leq ||Ax||^2 \leq (1+\sigma_S)||x||^2 \tag{5.3}$$

The major result in compressive sensing is that if x or $\overline{x}$ is approximately S-sparse and A satisfies RIP condition with order $2S$, then x or $\overline{x}$ can be recovered from y to the best S-sparse approximation x_S or $\overline{x}_S$ [139]. Since the recovery result is not used in this chapter, we omit the details here.

The next question is how to design the measurement matrix A to satisfy the RIP condition. The goal is to obtain a matrix so that the number of measurements m is as small as possible given a fixed number of signal dimension n. Although deterministic matrices can be constructed satisfying the RIP condition, the number of measurements can be quite large [140]. Fortunately, random matrices with elements being chosen from Gaussian, Bernoulli, or sub-Gaussian distributions satisfy the RIP condition of order S with high probability if $m = O(S\log(n/S))$ [141].

Another important random matrix satisfying the RIP condition is the random subsampled Fourier matrix. Let $\Psi \in \mathbb{R}^{n \times n}$ be the inverse Discrete Fourier Transform (DFT) matrix. If we choose $m = O(S(\log n)^4)$ random rows from Ψ to form a new matrix, then this matrix satisfies the RIP condition of order S with overwhelming probability [142]. Therefore, if a signal $x \in \mathbb{R}^n$ is S-sparse in the frequency domain, then we can randomly sample the signal at m points in the time domain, and the original signal can be recovered with high probability. For example, if an image is S-sparse in the frequency domain, then a small number of pixels in the image are sufficient to recover the original image. In other words, these small number of pixels contain the essential information for the entire image.

5.3 Stabilizing Controller Design

Based on the non-vector space control theory, a stabilizing controller can be designed. With compressive sensing, the same controller can still be used for stabilization if only a compressed set instead of the full set is available for feedback. In this section, we discuss the full and compressive feedback cases separately in detail.

5.3.1 Controller Design with Full Feedback

If the dynamics of sets is used, the stabilization problem with full feedback can be formulated as follows

Problem 1 *Consider the controlled mutation system described by Eq.* (4.9) *starting from an initial set* K_0*. Given a desired set* $\hat{K}$ *in the vicinity of* K_0*, we need to design a feedback controller* $u = \gamma(K(t))$ *so that* $\mathcal{D}(K(t), \hat{K}) \to 0$ *as* $t \to \infty$*.*

This problem can be solved using the controller Eq. (4.16) in Theorem 5. The controller is implemented as follows. First, we form the set for an image with each element in the set corresponding to a pixel in the image. In fact, each element in the set is $z = [z_1, z_2, z_3]^{\mathrm{T}}$ where z_1, z_2, and z_3 are defined as before, but in computation, z_1 and z_2 are the pixel indices representing the coordinates in discrete form in the image plane. Given a current image set represented by K and a desired image set $\hat{K}$, the control input u can be computed using Eq. (4.16) by replacing the integral with a summation because of the discrete image.

Note that although each element in the image set is a vector, the dynamics and controller are formulated in non-vector space (the space of sets). Therefore, this method is different from traditional vector space based visual servoing approaches.

5.3.2 Controller Design with Compressive Feedback

The controller in Theorem 5 is based on the full feedback when set K is available. Under the framework of compressive sensing, it is interesting to see what will happen if the compressive feedback K_c is used. Specifically, we are interested in the case of compressive feedback $K_c \subset K$. In other words, the compressive feedback is when only partial elements in set K are available for feedback. With compressive feedback, the stabilization problem can be stated as follows

Problem 2 *Consider the controlled mutation system described by Eq.* (4.9) *starting from an initial set* K_0*. Given a goal compressive set* $\hat{K}_c \subset \hat{K}$ *and an initial compressive set* $K_c(0) \subset K_0$*, design a controller* $u(t) = \gamma(K_c(t))$ *based on the current compressive feedback set* $K_c(t) \subset K(t)$ *such that* $\mathcal{D}(K(t), \hat{K}) \to 0$ *as* $t \to \infty$*.*

For this problem, we can first design a controller to make sure $\mathcal{D}(K_c(t), \hat{K}_c) \to 0$ as $t \to \infty$. After that, we can find the conditions on which if $\mathcal{D}(K_c(t), \hat{K}_c) \to 0$, then $\mathcal{D}(K(t), \hat{K}) \to 0$. Since $K_c(t) \subset K(t)$ is still a set, and the system dynamics described by Eq. (4.15) in the non-vector space is the same, the same controller can be utilized to locally stabilize K_c at $\hat{K}_c$ as stated in the following proposition.

Proposition 1 *For the system described by Eq.* (4.15) *with compressive feedback $K_c(t) \subset K(t)$, a compressive goal set $\hat{K}_c \subset K_c$, and a compressive initial set $K_c(0)$, the following controller can locally stabilize K_c at $\hat{K}_c$:*

$$u = \gamma(K_c) = -\alpha D(K_c)^+ \tag{5.4}$$

with $D(K_c)$ being obtained from Eq. (4.17) by replacing K and $\hat{K}$ with K_c and $\hat{K}_c$, respectively.

With Proposition 1, we need to ensure if $\mathcal{D}(K_c(t), \hat{K}_c) \to 0$, then $\mathcal{D}(K(t), \hat{K}) \to 0$, which is the stability analysis in the next section. For stability analysis, we assume the set K and $\hat{K}$ have the following form.

$$K = \{[i,\, x_i]^{\mathrm{T}} : i = 1,\, 2,\, \ldots,\, n\}, \quad \hat{K} = \{[i,\, \hat{x}_i]^{\mathrm{T}} : i = 1,\, 2,\, \ldots,\, n\} \tag{5.5}$$

where x_i and $\hat{x}_i$ are the i-th component in signals $x \in \mathbb{R}^n$ and $\hat{x} \in \mathbb{R}^n$, respectively. In other words, the i-th element in K or $\hat{K}$ is a vector containing the index and the i-th component in x or $\hat{x}$. Therefore, we can consider K and $\hat{K}$ correspond to x and $\hat{x}$, respectively. One implicit assumption for the form of K and $\hat{K}$ in Eq. (5.5) is that they have the same cardinality. This is correct for control systems because the sampled signals always have the same dimension. For instance, in visual servoing, the sampled images have the same size as the camera resolution. Another implicit assumption is the dimension of signal $p = 2$ in Theorem 5.

Suppose the compressive feedback set K_c and the desired set $\hat{K}_c$ are subsets of K and $\hat{K}$, respectively. In this case, they are represented as follows

$$K_c = \{[I_j,\, y_j]^{\mathrm{T}} : j = 1, 2, \ldots, m\}, \hat{K}_c = \{[I_j,\, \hat{y}_j]^{\mathrm{T}} : j = 1, 2, \ldots, m\} \tag{5.6}$$

where $y_j = x_i$ for some i, and $I_j = i$ is the corresponding index for y_j. Similar arguments apply to $\hat{K}_c$. Stacking all the y_j or $\hat{y}_j$ into vector $y \in \mathbb{R}^m$ or $\hat{y} \in \mathbb{R}^m$, we can assume K_c and $\hat{K}_c$ correspond to the signals y and $\hat{y}$, respectively. Therefore, x and $\hat{x}$ can be considered as being projected to lower dimension vectors y and $\hat{y}$ via a special matrix $\Phi \in \mathbb{R}^{m \times n}$ comprising the m different row vectors from the standard basis of $\mathbb{R}^n$ as its row vectors

$$y = \Phi x, \quad \hat{y} = \Phi \hat{x} \tag{5.7}$$

Remark: We choose the vector form for each element in the set for the stability analysis in the next section. However, the stabilization problem is still analyzed in the non-vector space since the controllers in Eq. (4.16) and Eq. (5.4) are obtained in the non-vector space.
Remark: We choose $p = 2$ in the previous discussion for simplicity; however, the same arguments can be applied to $p > 2$ by considering each axtra dimension with the index separately.

5.4 Stability Analysis with Compressive Feedback

Although we have $\mathcal{D}(K_c, \hat{K}_c) \to 0$ with the controller in Eq. (5.4), our goal stated in Problem 2 to steer K to $\hat{K}$ such that $\mathcal{D}(K, \hat{K}) \to 0$ may fail. It is possible that some other set $\tilde{K}$, after being compressed, can yield the same $\hat{K}_c$. In this case, we may have the undesirable result $\mathcal{D}(K, \tilde{K}) \to 0$. In this section, we will develop conditions to guarantee $\mathcal{D}(K, \hat{K}) \to 0$ or $\mathcal{D}(K, \hat{K})$ less than some constant number if $\mathcal{D}(K_c, \hat{K}_c) \to 0$.

5.4.1 Stability for Sparse Feedback

We first investigate the case with exact sparse feedback signals. We assume the sets in Eqs. (5.5) and (5.6). In other words, let set K correspond to vector $x \in \mathbb{R}^n$, set $\hat{K}$ correspond to vector $\hat{x} \in \mathbb{R}^n$, set K_c correspond to vector $y \in \mathbb{R}^m$, and set $\hat{K}_c$ correspond to vector $\hat{y} \in \mathbb{R}^m$. Moreover, x and y, $\hat{x}$ and $\hat{y}$ are related by Eq. (5.7). Under this setting, we have the following Lemma:

Lemma 3 *With the set defined by Eq.* (5.5)*, we have $\mathcal{D}(K, \hat{K}) \to 0$ if and only if $||x - \hat{x}|| \to 0$.*

Proof: *(1) First of all, let's show $\mathcal{D}(K, \hat{K}) \to 0 \Rightarrow ||x - \hat{x}|| \to 0$. By the definition of Hausdorff distance, if $\mathcal{D}(K, \hat{K}) \to 0$, then for any $[i, x_i]^{\mathrm{T}} \in K$, we have $\min_{[j, \hat{x}_j]^{\mathrm{T}} \in \hat{K}} ||[i, x_i]^{\mathrm{T}} - [j, \hat{x}_j]^{\mathrm{T}}|| \to 0$. Without loss of generality, let $[j, \hat{x}_j]^{\mathrm{T}}$ be the element in $\hat{K}$ when the minimum is achieved, then $||[i, x_i]^{\mathrm{T}} - [j, \hat{x}_j]^{\mathrm{T}}|| \to 0$. Since the norm cannot approach zero if the indices are different, we have $i = j$. Therefore, $||x_i - \hat{x}_j|| = ||x_i - \hat{x}_i|| \to 0$. Since $||x - \hat{x}||$ is the sum of all the squares of such differences, we have $||x - \hat{x}|| \to 0$.*

(2) Second, let's show $||x - \hat{x}|| \to 0 \Rightarrow \mathcal{D}(K, \hat{K}) \to 0$. From $||x - \hat{x}|| \to 0$, each element $||x_i - \hat{x}_i|| \to 0$. For any $[i, x_i]^{\mathrm{T}} \in K$, we have $\min_{[j, \hat{x}_j]^{\mathrm{T}} \in \hat{K}} ||[i, x_i]^{\mathrm{T}} - [j, \hat{x}_j]^{\mathrm{T}}|| \leq$

$||x_i - \hat{x}_i|| \to 0$. *For any other elements in K, we also have similar arguments. As a result,* $\max_{[i,x_i]^{\mathrm{T}} \in K} \min_{[j,\hat{x}_j]^{\mathrm{T}} \in \hat{K}} ||[i, x_i]^{\mathrm{T}} - [j, \hat{x}_j]^{\mathrm{T}}|| \to 0$. *Similarly, we have*

$$\max_{[j,\hat{x}_j]^{\mathrm{T}} \in \hat{K}} \min_{[i,x_i]^{\mathrm{T}} \in K} ||[j, \hat{x}_j]^{\mathrm{T}} - [i, x_i]^{\mathrm{T}}|| \to 0$$

Therefore, $\mathcal{D}(K, \hat{K}) \to 0$ by the definition of Hausdorff distance.

Remark: We provided a similar proof of the lemma with the image as an example in [129]. With the compressive set in Eq. (5.6), we also have $\mathcal{D}(K_c, \hat{K}_c) \to 0$ if and only if $||y - \hat{y}|| \to 0$ following similar arguments.

Remark: This lemma is also valid for $p > 2$ with the set K and $\hat{K}$ defined similar to Eqs. (5.5) and (5.6). In fact, if each element in K or $\hat{K}$ is a p-dimensional vector with the first one being the index value, then the same proof can be conducted by combining each non-index element with the index element to form a two dimensional vector. Based on Lemma 3, we have the following theorem

Theorem 6 *Suppose x and $\hat{x}$ are S-sparse in the Ψ-domain, i.e., $x = \Psi\bar{x}$ and $\hat{x} = \Psi\hat{\bar{x}}$ with $\bar{x} \in \Omega_S$ and $\hat{\bar{x}} \in \Omega_S$, and $\Psi \in \mathbb{R}^{n \times n}$ an orthornormal matrix. With the sets defined by Eqs. (5.5) and (5.6), if matrix $A = \Phi\Psi$ satisfies the RIP condition with order $2S$ (Φ comes from Eq. (5.7)), then we have $\mathcal{D}(K, \hat{K}) \to 0$ if $\mathcal{D}(K_c, \hat{K}_c) \to 0$.*

Proof: *From $\mathcal{D}(K_c, \hat{K}_c) \to 0$, we have $||y - \hat{y}|| \to 0$ based on Lemma 3. Since A satisfies the RIP condition with order $2S$, there exists $\sigma_{2S} \in (0,\ 1)$ such that:*

$$(1 - \sigma_{2S})||\bar{x} - \hat{\bar{x}}||^2 \leq ||A(\bar{x} - \hat{\bar{x}})||^2 = ||y - \hat{y}||^2 \tag{5.8}$$

Since $1-\sigma_{2S}>0$ *and* $||y-\hat{y}||\rightarrow 0$*, we have* $||x-\hat{x}||^2 = ||\Psi\bar{x}-\Psi\hat{\bar{x}}||^2 = ||\bar{x}-\hat{\bar{x}}||^2 \rightarrow 0$*. Based on Lemma 2 again,* $\mathcal{D}(K,\hat{K})\rightarrow 0$*.*

5.4.2 Stability for Approximate Sparse Feedback

Signals are rarely exactly sparse in reality, but they can be well approximated by exact sparse signals. Furthermore, most of them obey the so-called power law decay. Suppose the entries in a signal $x\in\mathbb{R}^n$ are rearranged such that $|x_1|\geq|x_2|\geq\cdots\geq|x_n|$. If

$$|x_i| < Ri^{-1/w}, \qquad 0<w<1$$

with R the smallest possible constant, then the signal belongs to the weak ℓ_w ball with radius R, denoted by $\mathbb{B}(\ell_w,R)$. The signals in $\mathbb{B}(\ell_w,R)$ can be approximated by their S-sparse approximation quite well. In fact, for any $x\in\mathbb{R}^n$, we have [143]

$$||x-x_S||_1 \leq C_w R S^{1-1/w}, \quad ||x-x_S|| \leq D_w R S^{0.5-1/w}$$

where x_S is the S-sparse approximation defined by Definition 1, $C_w=(1/w-1)^{-1}$, and $D_w=(2/w-1)^{-0.5}$. It would be interesting to see whether Theorem 2 is still valid for approximately sparse signals. In this sub section, we derive an upper bound for $\mathcal{D}(K,\hat{K})$ if $\mathcal{D}(K_c,\hat{K}_c)\rightarrow 0$. In order to do this, we need the following lemma (Proposition 3.5 in [143])

Lemma 4 *If a matrix* $A\in\mathbb{R}^{m\times n}$ *satisfies the RIP with order* S *and a constant* σ_S*, then for any* $x\in\mathbb{R}^n$*, we have*

$$||A(x-x_S)|| \leq \sqrt{1+\sigma_S}\left[||x-x_S|| + \frac{1}{\sqrt{S}}||x-x_S||_1\right] \tag{5.9}$$

Theorem 7 *Suppose x and $\hat{x}$ are approximately sparse in the Ψ-domain, i.e., $x = \Psi\bar{x}$ and $\hat{x} = \Psi\hat{\bar{x}}$ with $\bar{x} \in \mathbb{B}(\ell_w, R)$ and $\hat{\bar{x}} \in \mathbb{B}(\ell_w, R)$, and $\Psi \in \mathbb{R}^{n\times n}$ an orthornormal matrix. With the sets defined by Eqs. (5.5) and (5.6), if matrix $A = \Phi\Psi$ satisfies the RIP condition with order $2S$ and constant σ_{2S}, then we have*

$$\mathcal{D}(K, \hat{K}) \leq 2(1 + \frac{\sqrt{1+\sigma_{2S}}}{\sqrt{1-\sigma_{2S}}})D_w RS^{0.5-1/w} + \frac{\sqrt{2(1+\sigma_{2S})}}{\sqrt{S(1-\sigma_{2S})}}C_w RS^{1-1/w} \tag{5.10}$$

if $\mathcal{D}(K_c, \hat{K}_c) \to 0$.

Proof: *We first show $||x - \hat{x}|| = ||\Psi\bar{x} - \Psi\hat{\bar{x}}|| = ||\bar{x} - \hat{\bar{x}}||$ is bounded. Let $\bar{x}_S$ and $\hat{\bar{x}}_S$ be the S-sparse approximation for $\bar{x}$ and $\hat{\bar{x}}$, respectively. Let $e = \bar{x} - \hat{\bar{x}}$, $e_1 = \bar{x}_S - \hat{\bar{x}}_S$, and $e_2 = e - e_1$. Since $e_1 \in \Omega_{2S}$ and A satisfies the RIP condition with order $2S$, we have*

$$||A(e - e_1)|| \leq \sqrt{1+\sigma_{2S}}\left[||e_2|| + \frac{1}{\sqrt{2S}}||e_2||_1\right]$$

from Lemma 4. From $\mathcal{D}(K_c, \hat{K}_c) \to 0$, we have $||y - \hat{y}|| \to 0$, which is equivalent to $||Ae|| \to 0$. Therefore, $||Ae_1|| \leq \sqrt{1+\sigma_{2S}}\,[||e_2|| + \frac{1}{\sqrt{2S}}||e_2||_1]$. Since A satisfies the RIP condition with order $2S$, we have

$$||e_1|| \leq \frac{||Ae_1||}{\sqrt{1-\sigma_{2S}}} \leq \frac{\sqrt{1+\sigma_{2S}}}{\sqrt{1-\sigma_{2S}}}\left[||e_2|| + \frac{1}{\sqrt{2S}}||e_2||_1\right]$$

Since $||e_2|| = ||e - e_1|| = ||x - x_S - (\hat{x} - \hat{x}_S)|| \leq 2D_w RS^{0.5-1/w}$ and similarly $||e_2||_1 \leq 2C_w RS^{1-1/w}$, we obtain the bound for $||x - \hat{x}||$ as

$$||x - \hat{x}|| = ||e|| \leq ||e_1|| + ||e_2|| \leq 2(1 + \frac{\sqrt{1+\sigma_{2S}}}{\sqrt{1-\sigma_{2S}}})D_w RS^{0.5-1/w} + \frac{\sqrt{2(1+\sigma_{2S})}}{\sqrt{S(1-\sigma_{2S})}}C_w RS^{1-1/w}$$

Next, we need to establish the relation between $\mathcal{D}(K, \hat{K})$ and $||x - \hat{x}||$. In fact, we can show that $\mathcal{D}(K, \hat{K}) \leq ||x - \hat{x}||$. For any $k_i = [i, x_i]^{\mathrm{T}} \in K$, we have:

$$d_{\hat{K}}(k_i) = \min_{w \in \hat{K}} d(k_i, w) \leq |x_i - \hat{x}_i|$$

Then

$$d(K, \hat{K}) = \max_{k_i \in K} d_{\hat{K}}(k_i) \leq \max\{|x_i - \hat{x}_i|, i = 1, 2, \cdots, n\}$$

Similarly,

$$d(\hat{K}, K) \leq \max\{|\hat{x}_i - x_i|, i = 1, 2, \cdots, n\}$$

Therefore,

$$\mathcal{D}(K, \hat{K}) = \max\{d(K, \hat{K}), d(\hat{K}, K)\} \leq \max\{|\hat{x}_i - x_i|, i = 1, 2, \cdots, n\} \leq ||x - \hat{x}||$$

Based on the above arguments, we finish the proof of the theorem.

Remark: The above proposition suggests, with $\mathcal{D}(K_c, \hat{K}_c) \to 0$, the Hausdorff distance between the current full set and the desired full set is bounded, and the stability of the system can be guaranteed.

Remark: We have shown the stability for a special case when the matrix A satisfies the RIP condition with order n in [130]. In Theorem 7, we extend our results to the case when A satisfy the RIP condition with order $2S$, which is general than the special case with $S = \lceil n/2 \rceil$, where $\lceil \cdot \rceil$ is the ceil operator.

Remark: Theorem 6 and Theorem 7 can be extended to the case with $p > 2$. In this case, elements in each set K, $\hat{K}$, K_c, and $\hat{K}_c$ are p-dimensional vectors with the index value in the first dimension. We can treat each elements in the $p-1$ dimensional vectors except the index individually. This way, Theorem 6 still holds, while the bound in Theorem 7 will change. The derivation is omitted here.

5.5 Testing Results

In this section, we present experimental results on a robotic manipulator to validate the designed controller with compressive feedback.

The experiments are conducted on a seven DOF Schunk LWA3 redundant manipulator. A camera is attached to the manipulator's end-effector (the eye-in-hand configuration). As a first step to validate the controller, a white planar board with regular black shapes including a rectangle, a square, and a circle is employed for the experiment [112]. Although we can use the image moments based servoing method for such shapes [79], our goal here is to test our compressive feedback based non-vector space controller.

The experimental procedure follows the general look-and-move structure [124]. The robot is first moved to a position and the image is recorded as the desired image. Then, the robot is relocated to some other position as the initial position, where an initial image is taken. With these two images, the non-vector space controller computes a camera velocity, which is resolved into the joint speeds via the inverse velocity kinematics. Then, the robot executes this speed through the robot controller. After reaching a new position, an updated image is acquired, and a new velocity is calculated. This process is repeated until the desired image is obtained from the camera.

We use an ordinary CMOS camera for experiments. To reduce the noise effect for such a camera, we convert grey scale images to binary images. The image size recorded by the

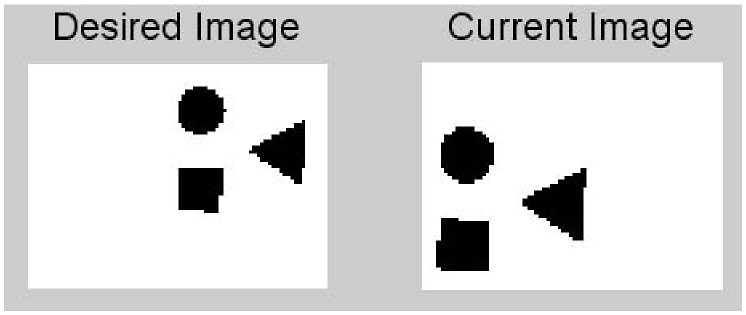

Figure 5.2 The initial and goal images for the three dimensional translational motion experiment.

camera is 60×80 pixels. Because of the binary image, the number of random sampling points can be small compared to the image size. In fact, we choose the number to be 500. Under such settings, two experiments are performed, which are detailed as follows.

5.5.1 3D Translational Motion

For the first experiment, the robot motion is restricted to a three dimensional translation. In this case, the row vector $D(K_c)$ in the controller Eq. (5.4) is simplified to:

$$D(K_c) = \int_{K_c} \frac{1}{p_z}[0,\, 0,\, d^2_{\hat{K}_c}(z)]^{\mathrm{T}} dz + \int_{K_c} \frac{1}{p_z} L(z)^{\mathrm{T}} (z - P_{\hat{K}_c}(z)) dz - \int_{\hat{K}_c} \frac{1}{p_z} L(P_{K_c}(\hat{z}))^{\mathrm{T}} (\hat{z} - P_{K_c}(\hat{z})) d\hat{z}$$

with

$$L(z) = \begin{bmatrix} -1 & 0 & z_1 \\ 0 & -1 & z_2 \\ 0 & 0 & 0 \end{bmatrix}$$

In general, p_z varies with different $z \in K$ or $\hat{z} \in \hat{K}$. But if the observed object is planar such as the board used in our experiment, then p_z will be the same, and it can be taken out from the integral. In this case, although p_z will change during the translation along the optical axis, it only effects the magnitude of $u(t)$, and we can assume p_z to be one.

For the initial and desired images shown in Fig. 5.2, the experimental results are shown Fig. 5.3, where the errors in three axes with respect to time are plotted. From Fig. 5.3, the controller can make the manipulator move to the desired position since the errors decrease to values around zero. The small steady state error (within 4 mm) also verifies the theory since the image is only approximately sparse in the frequency domain.

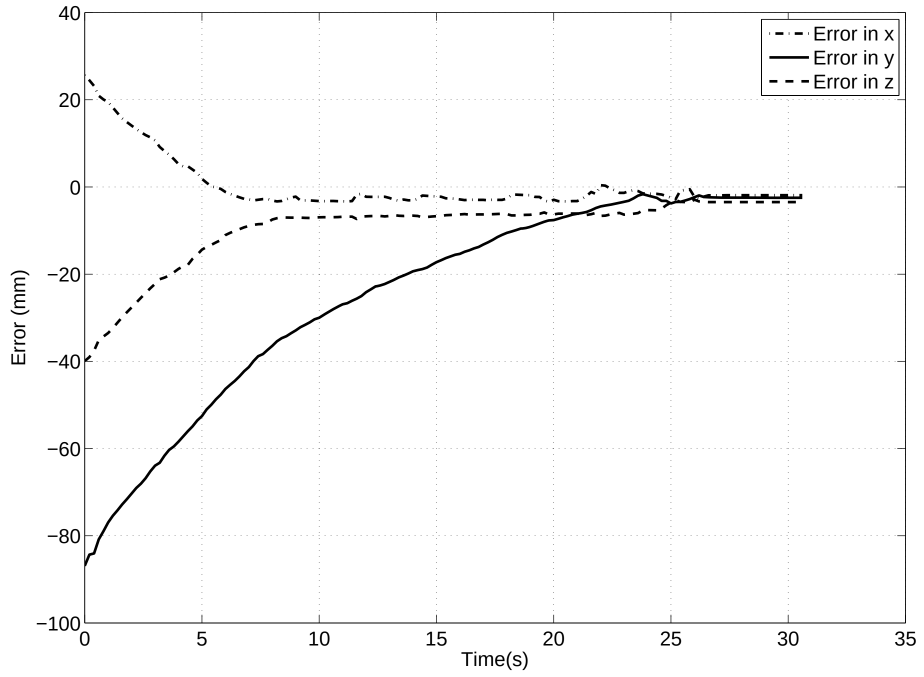

Figure 5.3 Task space errors for the three dimensional translational motion experiment.

5.5.2 SE(2) Motion

The second experiment is performed similar to the first one. In this experiment, the robot's motion is constrained to the SE(2) motion group — the two translational DOF in the plane perpendicular to the optical axis and the rotation around the axis. In this case, the row vector $D(K_c)$ in the controller Eq. (5.4) is simplified to:

$$D(K_c) = \int_{K_c} L(z)^{\mathrm{T}}(z - P_{\hat{K}_c}(z))dz - \int_{\hat{K}_c} L(P_{K_c}(\hat{z}))^{\mathrm{T}}(\hat{z} - P_{K_c}(\hat{z}))d\hat{z} \tag{5.11}$$

with

$$L(z) = \begin{bmatrix} -1/p_z & 0 & z_2 \\ 0 & -1/p_z & -z_1 \\ 0 & 0 & 0 \end{bmatrix}$$

Note that p_z is a constant if the observed object is planar.

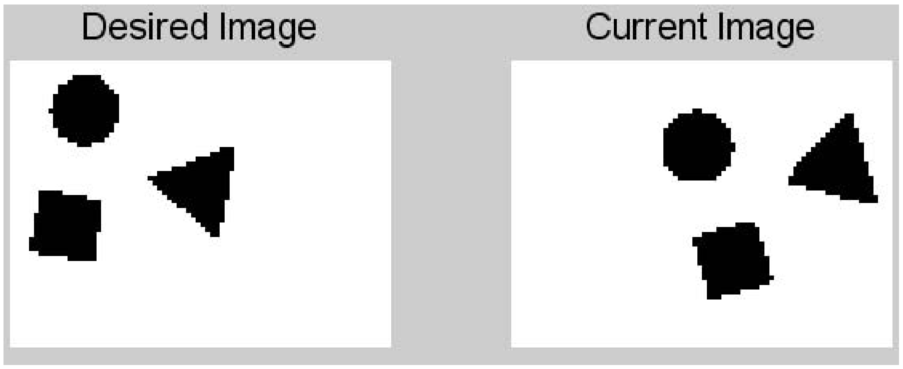

Figure 5.4 The initial and goal images for the SE(2) motion experiment.

For the initial and desired images shown in Fig. 5.4, the experimental results are shown in Fig. 5.5, where the task space errors with respect to time are plotted. From Fig. 5.5, the controller can make the manipulator move to the desired position. Moreover, the error for rotation motion keeps constant initially (from zero to five seconds). This suggests the rotational motion happens after the position is close enough. Again, a small steady state error exists because the image is only approximately sparse in the frequency domain.

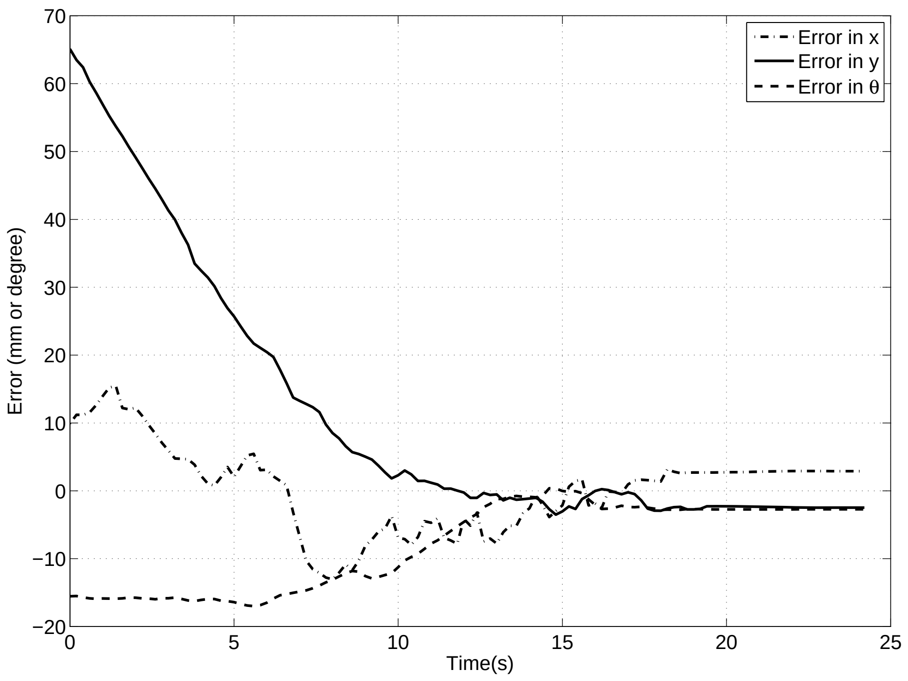

Figure 5.5 Task space errors for the SE(2) motion experiment.

5.6 Conclusions

In this chapter, we proposed the concept of compressive feedback and incorporated it to the non-vector space control method. The compressive feedback can reduce the number of samples for feedback, while the non-vector space control can perform the control directly on sets instead of vectors. Meanwhile, the non-vector space controller with compressive feedback computes faster due to a smaller number of samples. We prove the stability for both sparse and approximate sparse feedback signals. Experimental results on the robotic manipulators show that a small number of feedbacks can guarantee the controller's stability.

Chapter 6

Non-vector Space Landing Control for MSU Tailbot

6.1 Introduction

In this chapter, we aim to implement the non-vector space approach to control the landing posture of the MSU tailbot using vision feedback. Specifically, the robot body's mid-air orientation can be controlled by the tail's movement. Using vision feedback, the non-vector space controller computes a control input to actuate the tail to control the body's orientation so that the robot can land on an unknown surface with a desired posture.

Two challenges exist for controlling a miniature robot's mid-air orientation with vision. On one hand, the small size of the robot requires a small embedded system that has the visual sensing, computation, and control capability. The design of such an embedded system is difficult. On the other hand, with a small embedded system, the control bandwidth should be large enough since the robot only stays in mid-air for a short time (less than half second for a free fall from a height of one meter).

To address the first challenge, we developed a small embedded system with a tiny camera, a microcontroller with wireless communication capability, inertial sensors, and a DC motor driver. Using such an embedded system and our previous tailed jumping robot [109], we implement the non-vector space approach in the system to address the second challenge.

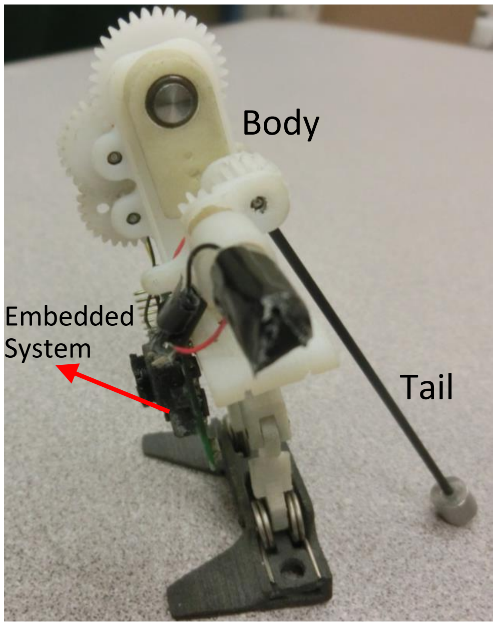

Figure 6.1 The robot prototype for experiments

The rest of this chapter is organized as follows. First, we describe the robotic system including the tailed robot and the embedded control system in section 6.2. Then we present the experimental setup and results and discuss future works in section 6.3.

6.2 System Description

The non-vector space control algorithm discussed in Chapter 4 is implemented on the MSU tailbot as shown in Fig. 6.1. The system has two major components: the mechanical part and the embedded system part.

The mechanical part is based on our previous tailed jumping robot. Since the detailed design can be found in [98, 109], we only briefly describe it here. The mechanical part can be divided into a body and a tail part, which are connected to each other through a revolute joint. This revolute joint is actuated by a miniature DC motor (GH6123S from Gizmoszone). When the robot is in mid-air, the swinging of the tail can control the body's angle due to

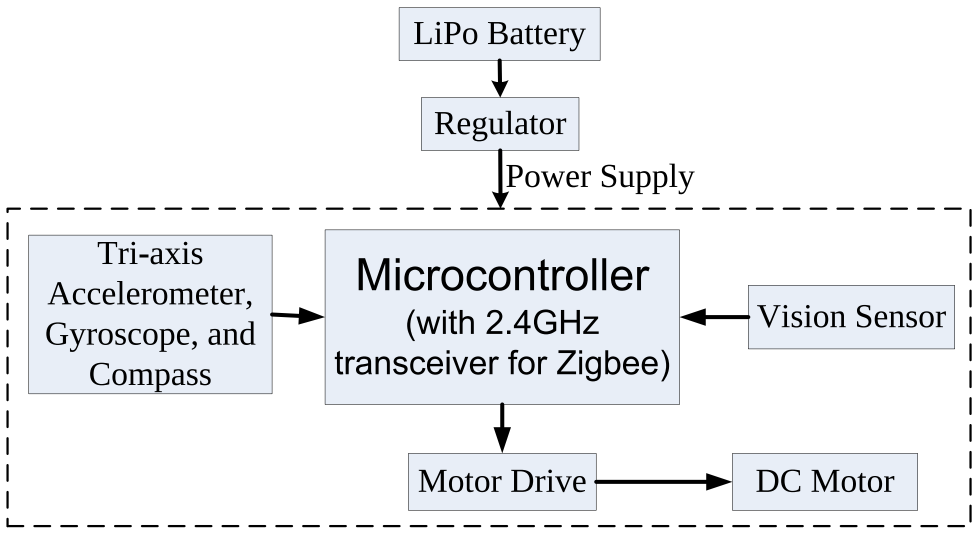
LiPo Battery
Regulator
Power Supply
Tri-axis Accelerometer, Gyroscope, and Compass
Microcontroller (with 2.4GHz transceiver for Zigbee)
Vision Sensor
Motor Drive
DC Motor

Figure 6.2 The schematic of the embedded control system

the conservation of angular momentum if the air resistance is neglected.

For the tailed jumping robot, the ultimate goal for this research is to let the robot use vision as feedback to control its landing posture after it jumps up. However, since the tail has only one degree-of-freedom, only the orientation of the body around an axis along the revolute joint axis can be controlled. As a result, it is difficult to perform the landing experiment after jumping because the robot may rotate in other uncontrollable axes once it jumps from the ground due to unpredictable initial angular momentum it may have at the take-off process [109]. To circumvent this issue, we let the robot fall from some height to eliminate the motion in uncontrollable axes because this free fall motion is the same for the jumping robot during the falling down motion.

To control the robot's body orientation using vision feedback, all of the existing embedded systems cannot be used due to the size limit (centimeter scale) for the robot. Therefore, we designed a miniature embedded system with the architecture shown in Fig. 6.2. A microcontroller (ATmega128RFA1 from Atmel) severs as the central processing unit. It has an onboard $2.4GHz$ RF transceiver for wireless communication. A stonyman vision chip from

Centeye Inc, the main sensing unit in the system, provides the vision feedback. A MPU9150 inertial sensor from Invensense—including a tri-axis accelerometer, a tri-axis gyroscope, and a tri-axis compass—serves as a secondary sensing unit. A MC34933 motor driver from Freescale is the actuation unit to drive the DC motor that actuates the tail. Finally, a $50mAh$ Lithium polymer battery powers the whole control system after being regulated to $3.3V$. The embedded system is implemented with a printed circuit board (PCB) having only a size of $22mm \times 22mm$ and a mass of $1.93g$.

One of the most important parts in the system is the stonyman vision chip, which is directly wire bonded to the designed PCB. Different from traditional complementary metal-oxide semiconductor (CMOS) or charge-coupled device (CCD) sensors that use linear pixels, the stonyman chip employs analog logarithmic sensing elements for each pixel, which means the voltage output of each pixel is a logarithmic function of the light intensity sensed by that pixel.

The analogy logarithmic pixels have three major advantages. First, we can easily read the sensor data by analog-to-digital sampling, which is available in almost all kinds of microcontrollers. Moreover, we can read arbitrary pixel by specifying the column and row numbers. Second, logarithmic pixels allow a wide range of light intensities due to the logarithm nature of each reading. Third, with analogy logarithmic pixels, the vision senor can work with only a few external electrical components, and the interface between the sensor and the microcontroller is simple. Therefore, we can design the system to have a small size.

Although we can read the intensity value for a specific pixel, we need to read in serial in order to obtain one image since only one pixel can be read at each time. In the application of vision based control, it is unnecessary and time consuming to read the whole picture with a resolution of 112×112 pixels for the stonyman vision sensor. Therefore, we only read images

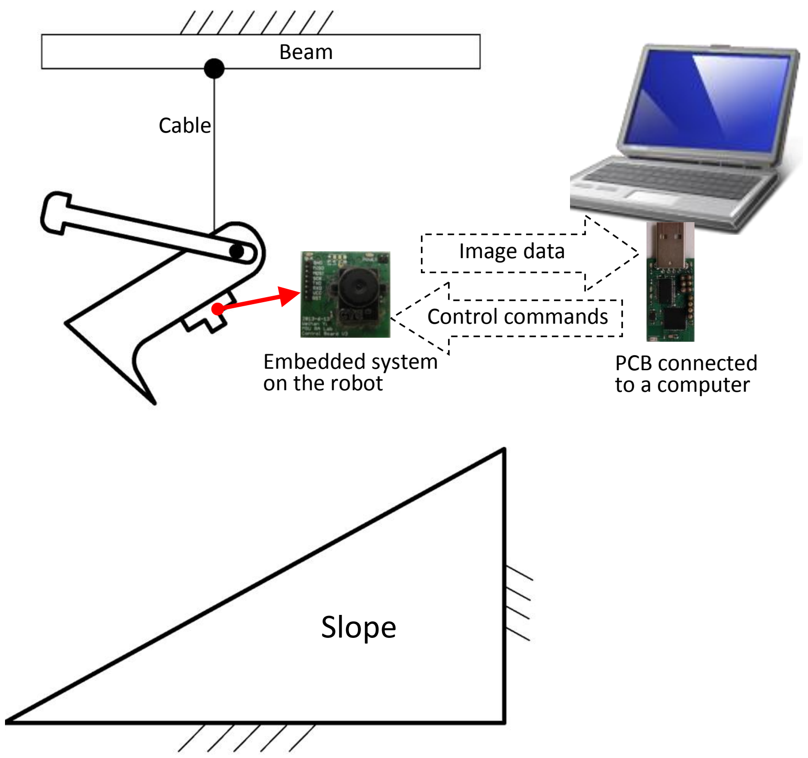

Figure 6.3 The illustrated experimental setup of the tailed robot system

of 20×20 at the center of the sensor to increase the frame rate and the control bandwidth.

To receive the data from the embedded system on the robot, we designed another PCB that can perform wireless communication with the embedded system on the robot through the IEEE 802.15.4 protocol. The PCB has two major parts: a microcontroller (ATmega128RFA1 from Atmel) and chip for USB to serial interface (FT232RL from FTDI). It connects to a computer through a USB connector. The data obtained from the embedded system on the robot can be wirelessly transmitted to the microcontroller on the PCB that connects to the computer. Then, they can be forwarded to the computer through the USB to serial interface.

6.3 Experimental Setup and Results

Using the mechanical and electrical systems discussed in the previous section, we can implement the non-vector space control method. The ultimate goal is to use the vision feedback to make the robot land on arbitrary surfaces with a desired unknown posture. However, as our first step, the robot is controlled to land on a slope with an unknown tilted angle.

Fig. 6.3 illustrates the basic idea of experimental setup. The robot is hang from a fixed beam with a cable. The embedded system is attached to the robot's body with the vision sensor facing a slope. If the cable is cut, the robot undergoes a free fall motion. Although our goal is to achieve onboard control, as our initial step, we send the image data wirelessly to a computer to compute the control command using the non-vector space control. The control command is then sent back to the robot to actuate the tail. Before the experiment starts, a desired image is obtained which corresponds to the desired posture of the robot for landing on the slope. This desired image can be taken by putting the robot close to the hypotenuse of the slope.

The non-vector space control algorithm is implemented as follows. As the robot falls down, the motion is the translational motion in the yz image plane and the rotational motion about an axis perpendicular to yz plane. Therefore, we simplify the stabilization controller by only considering the translation along y and z axis and the rotation about x axis, which is the special SE(2) motion. In this case, if we consider a constant p_z, the interaction matrix becomes

$$L = \begin{bmatrix} 0 & x_1 & x_1 x_2 \\ -1 & x_2 & 1 + x_2^2 \end{bmatrix}$$

Given two images S and $\hat{S}$, the control algorithm is implemented as follows.

1. Form a set from an image. Given a gray scale image represented by matrix $A \in \mathbb{R}^{m \times n}$ with the entry a_{ij}, $(1 \leq i \leq m,\ 1 \leq j \leq n)$, the set for this image is

$$\{[1, 1, a_{11}]^T, [1, 2, a_{12}]^T, \cdots, [m, n, a_{mn}]^T\}$$

The intensity value a_{ij} can be properly rescaled to the range of the index values.

2. Obtain the Lyapunov function value using a discrete version of Eq. (4.11).

$$V(S) = \frac{1}{2}\sum_{x \in S} d^2_{\hat{S}}(x) + \frac{1}{2}\sum_{\hat{x} \in \hat{S}} d^2_S(\hat{x}) \tag{6.1}$$

3. Obtain the column vector $D(S) \in \mathbb{R}^3$ from Eq. (4.17):

$$D(S) = \frac{1}{2}\sum_{x \in S} d^2_{\hat{S}}(x)(\sum_{i=1}^{m} \frac{\partial f_i}{\partial x_i})^{\mathrm{T}} dx + \sum_{x \in S} f(x)^{\mathrm{T}}(x - P_{\hat{S}}(x)) - \sum_{\hat{x} \in \hat{S}} f(P_S(\hat{x}))^{\mathrm{T}}(\hat{x} - P_S(\hat{x})) \tag{6.2}$$

4. Calculate the control input using Eq. (4.16) by choosing a proper gain value α. Note that the control input will have three values including the translations along y and z, and a rotation around x. Since the translation motion is uncontrollable, we only use the value for rotation as the control input.

Based on the experimental setup and the detailed implementation procedure of the controller, we performed the experiment as follows. First, the embedded system on the robot uses the accelerometer to detect the free fall motion to see if the robot falls or not. If the free fall motion is detected, the embedded system on the robot starts to read and send the image to the computer. Based on the desired image and the current feedback image, the computer computes a command and sends it to the robot. Then the embedded system on the robot will use this command to actuate the tail. After that, another cycle including image reading, sending, and control command computing will be repeated until the robot lands on the ground.

We implement the experimental setup as shown in Fig. 6.4, where papers with rectangles, triangles, and circles are placed on top of the slope. During the experiment, the microcontroller runs at a frequency of 16MHz, and it uses the maximum wireless transmission speed of 2Mbps. Under such a setup, the system spends 0.11s to finish one control loop. Since we let the robot fall from a height about 1.5 meters, the control can be executed five times during the free fall motion. The desired image for the experiment is shown in Fig. 6.5(f), which is obtained by placing the robot at a posture when the image plane of the camera is approximately parallel to the slope. Before the experiment, the robot is hang at a position right above the place where the desired image is taken. Also, the initial posture of the robot is carefully tuned to make sure only the motion in the yz plane exists.

The experimental results are shown in Fig. 6.5, where images obtained from the camera during the control process are displayed. As seen from the figure, we obtained five images in total. As the robot falls down, shapes on the slope become larger in the image. By comparing the final image Fig. 6.5(e) and the desired image in Fig. 6.5(f), we can see that the two are quite close to each other, although the contrasts for them are different.

Note that a more rigorous comparison between the final posture and the desired posture where the desired image is taken will be performed in the future. The gyroscope on the embedded system can be used to obtain real time posture for the robot's body by integrating the angular velocities [109]. At this time, however, the system cannot continuously sample the gyroscope data since it is busy with reading and transmitting image data. In the future,

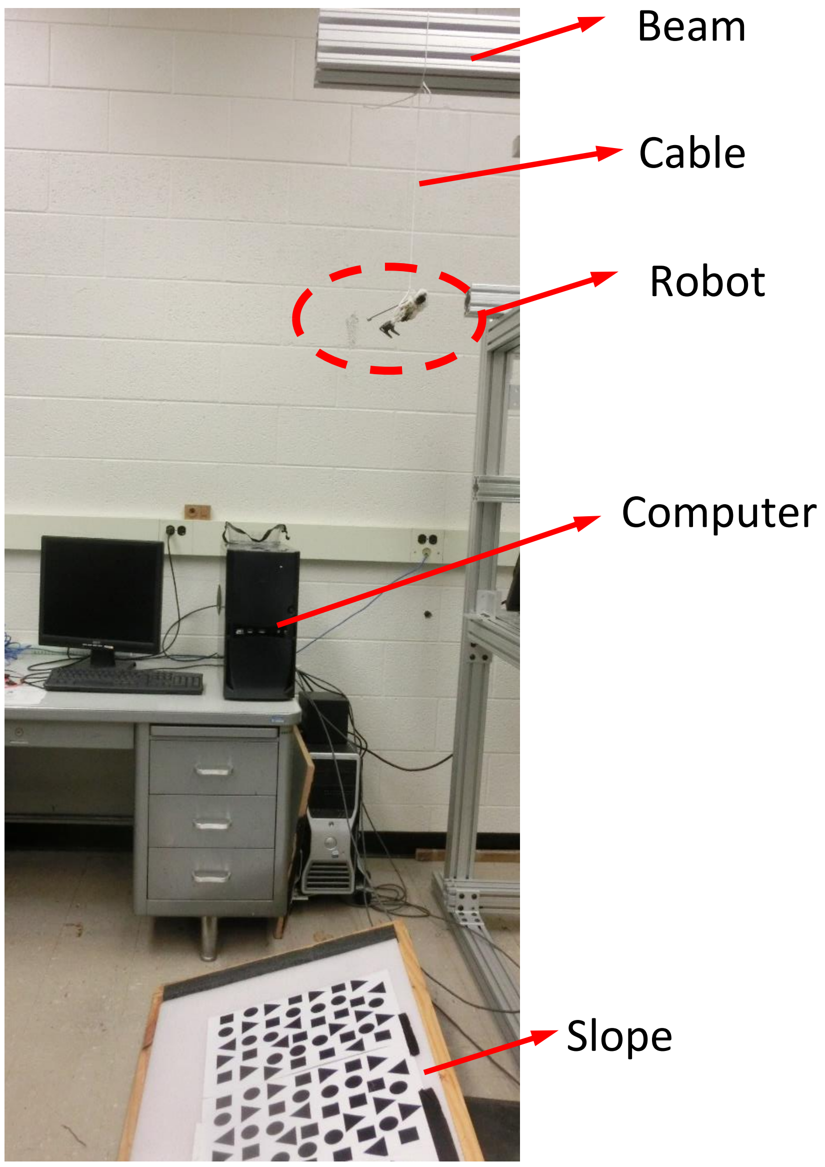

Figure 6.4 The experimental setup for implementing the non-vector space control on the tailed robot system

another embedded system will be attached to the robot and used to obtain the real time orientation of the robot to provide the ground truth for comparisons.

For a system in the non-vector space, if it is asymptotically stable, then the lyapunov function value for the system will decrease to zero as time goes to infinity. Therefore, we plot the lyapunov function values during the control process as shown in Fig. 6.6. From the figure, the value decreases as the robot falls down. The small increase for the fourth step might be due to the image noise.

The experimental results demonstrate the correctness of the non-vector space controller for image based control, although the control bandwidth is relatively small. However, with the idea of compressive feedback [144] and hardware improvement, it is possible to achieve real time onboard control using the non-vector space approach. In fact, the compressive feedback can be used when the feedback image is compressed. For example, under certain conditions, only partial image feedback can still guarantee the stability of system with the non-vector space controller. For hardware, there exist many microcontrollers that can run at speeds up to several hundred Hz such as ARM-based microcontrollers. Moreover, the computation for the non-vector space controller can be much faster if it is implemented on field-programmable gate array (FPGA) since the control algorithm is always the same.

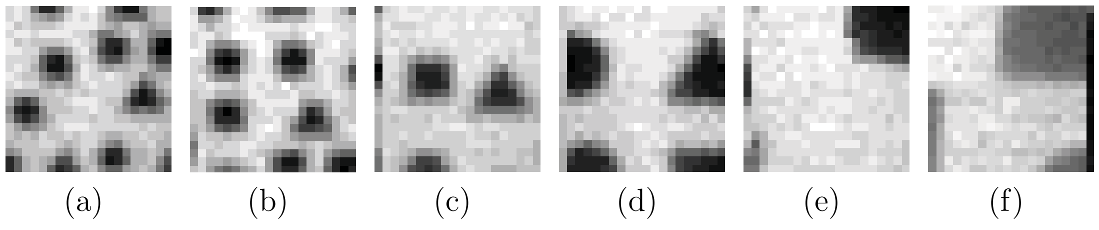

Figure 6.5 Images for the landing control experiment: (a) 1st image; (b) 2nd image; (c) 3rd image; (d) 4th image, (e) 5th image; (f) desired image.

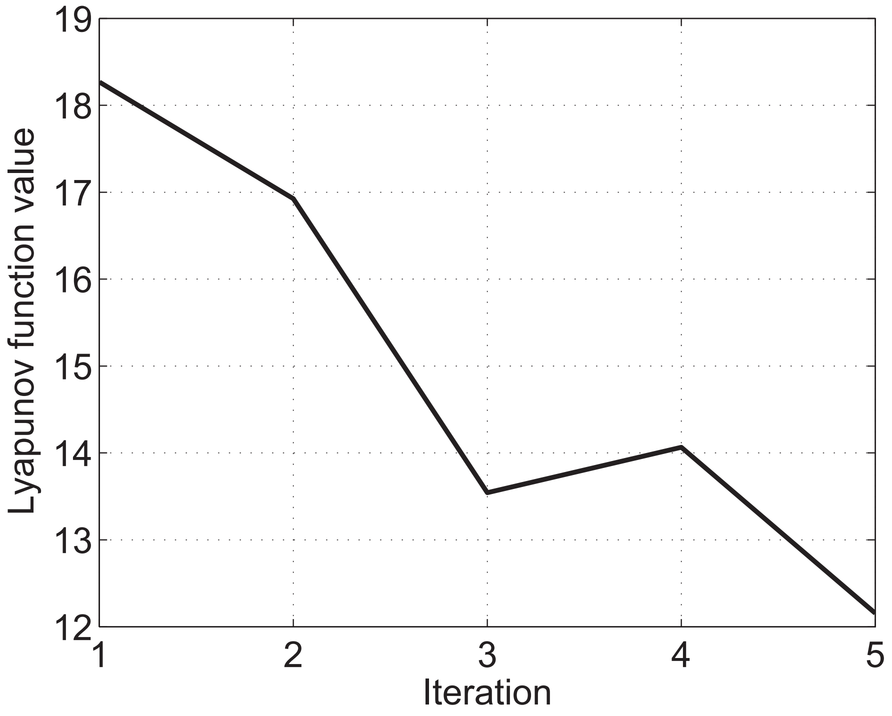

Figure 6.6 The value for the Lyapunov function decreases during the control process.

6.4 Conclusions

In this chapter, the controlled landing for miniature robots using vision feedback is discussed. Given a desired image and based on image feedback from a camera, a miniature tailed robot can achieve the desired landing posture after falling from some height by actively swinging its tail. The landing control strategy employs a non-vector control method by considering images as sets and formulating the control problem in the space of sets. In this new non-vector space, a controller can be designed. Such a method, when applied to vision based control, can eliminate the feature extraction and tracking, which are required by traditional approaches. Experimental results on the tailed root verify the correctness of the theory.

Chapter 7

Conclusions and Future Work

7.1 Conclusions

In this dissertation, a biologically inspired approach for robot design and control is investigated. The aim of such an approach is to see if small robots with sizes of a few centimeters could achieve multiple locomotion methods and real time onboard control to be able to dynamically interact with unstructured and uncertain environments. But with the robot's small size, two challenges exist. First, it is difficult to achieve multi-mode locomotion with a small size since the design space is limited. Second, it is difficult to achieve real time onboard control with a small size since the robot only has a limited computation power. This dissertation tries to address these two challenges by using biologically inspired design and control methods.

For the design part, both the MSU jumper and MSU tailbot show that biologically inspirations can be used for the design of small robots that have multiple locomotion methods. The MSU jumper can achieve functions such as jumping, steering, and self-righting using a single motor. The MSU tailbot can achieve jumping, wheeling, and aerial maneuvering with a small size. Such results cannot be achieved if biological inspirations are not used. Specially, the jumping mechanism is inspired by how small animals jump such as frogs. The tail mechanism is inspired by how small animals such as lizards can use its tail to control its mid-air orientation once it leaps into the air.

For the control part, the non-vector space control approach can be applied to vision based control without extracting and tracking features during the control process. By considering the image feedback as sets, the method directly formulates the control problem in the space of sets. Based on non-vector space control, compressive feedback is proposed to further reduce the computation requirement by using only a limited amount but an essential set of feedback. The stability for the closed loop system with compressive feedback is proved. Experimental results using a redundant robotic manipulator clearly show that the non-vector space approach can be used for vision based control with full and compressive feedback. Moreover, preliminary experiments on the MSU tailbot have also show the possibility of implementing the non-vector space approach on small size robots.

Both the bio-inspired design and control approach discussed in this dissertation can be used for other small scale robots. Ultimately, the bio-inspired approach can be used to address the two challenges for small robots. First, small robots can achieve multiple locomotion methods to travel in unstructured environments, just like small animals or insects. Second, small robots with limited computation power can also dynamically interact with uncertain environments. Eventually, the research presented in this dissertation can pave the way for the next generation agile and versatile small scale robots that can achieve or even surpass similar locomotions of their biological counterparts.

7.2 Future Research Work

Based on the research presented in this dissertation, there can be many future research directions, among which only a few are outlined in the following.

Almost all existing jumping robots can only jump from solid grounds. However, small animals such as frogs can jump out of water. Some insects such as water strider can even jump from the surface of water. Therefore, how could small robots jump from soft or fluid surface? This presents not only the design challenge but also the dynamics challenge. For the design part, the robot should be extremely lightweight to be able to jump from water surface. In this case, traditional DC motors and gear transmissions may not work. We need to explore new design methods employing novel actuations for such robots. For the dynamics part, it is difficult to model the dynamic jumping process from water since it involves many forces such as surface tension force, hydrodynamic force, and buoyancy force, etc. A more difficult problem would be how to model the dynamics to predict the jumping performance.

For all existing jumping robots, all of them are subject to landing impacts, which lead to an unpredictable landing position. Therefore, jumping locomotion is always associated with imprecise landing positions. Therefore, how can we achieve precise landing for jumping robots? Two possible solutions exist. First, we can add impact absorption structure to the robot. Such a passive way will ease the control of robot, but it will add a substantial amount of weight to the robot. Second, the robot can be equipped with fixed wings to glide down to the ground. A tail can be used to control the robot to minimize the landing impact while achieving precise landing position. This approach, however, requires complicated dynamics modeling and implementation on embedded control systems.

For the non-vector space control approach, future research can be focused on the implementation with more advanced embedded systems. For example, instead of using microcontroller with maximum frequency of only tens of MHz, more powerful single board computers such as the Raspberry Pi or the Beagleboard with about one GHz computation power can be used. In this way, it is possible that small robots can achieve real time onboard control, although the power consumption will be much larger. But the robots do not need to use such high computation power for all activities. For example, the MSU tailbot will only need to compute fast when it performs the aerial maneuvering. Therefore, it justifies the use of single board computers for small size robots.

For the compressive feedback, although it is proposed based on the non-vector space controller, it can be use for traditional vector space control as well. Future work can be done on how the compressive feedback be applied to vector space control with various control methods such as adaptive, robust, or optimal control. Moreover, with such an extension to vector space, the idea of compressive feedback can be used for control with a large amount of data for feedback. This is especially true for extending traditional control with big data feedback. In addition, extensions to the vector space may also allow fast computation speed. It is possible that this method can be implemented on those microcontrollers discussed in this dissertation.

REFERENCES

REFERENCES

[1] J. Burdick and P. Fiorini, "Minimalist jumping robots for celestial exploration," *Int. J. Robot. Res.*, vol. 22, no. 7, pp. 653–674, 2003.

[2] G. Song, K. Yin, Y. Zhou, and X. Cheng, "A surveillance robot with hopping capabilities for home security," *IEEE Trans. on Consumer Electronics*, vol. 55, no. 4, pp. 2034–2039, 2009.

[3] J. Zhang, G. Song, G. Qiao, T. Meng, and H. Sun, "An indoor security system with a jumping robot as the surveillance terminal," *IEEE Trans. on Consumer Electronics*, vol. 57, no. 4, pp. 1774–1781, 2011.

[4] L. Bai, W. Ge, X. Chen, and R. Chen, "Design and dynamics analysis of a bio-inspired intermittent hopping robot for planetary surface exploration," *Int J Adv Robotic Sy*, vol. 9, no. 109, 2012.

[5] B. G. A. Lambrecht, A. D. Horchler, and R. D. Quinn, "A small, insect inspired robot that runs and jumps," in *Proc. IEEE Int. Conf. Robot. Autom.*, Barcelona, Spain, 2005, pp. 1240–1245.

[6] U. Scarfogliero, C. Stefanini, and P. Dario, "The use of compliant joints and elastic energy storage in bio-inspired legged robots," *Mech. Mach. Theory*, vol. 44, no. 3, pp. 580–590, 2009.

[7] F. Li, W. Liu, X. Fu, G. Bonsignori, U. Scarfogliero, C. Stefanini, and P. Dario, "Jumping like an insect: Design and dynamic optimization of a jumping mini robot based on bio-mimetic inspiration," *Mechatronics*, vol. 22, no. 2, pp. 167–176, 2012.

[8] K. Kikuchi, K. Sakaguchi, T. Sudo, N. Bushida, Y. Chiba, and Y. Asai, "A study on a wheel-based stair-climbing robot with a hopping mechanism," *Mechanical Systems and Signal Processing*, vol. 22, no. 6, pp. 1316–1326, 2008.

[9] M. Kovac, M. Fuchs, A. Guignard, J. Zufferey, and D. Floreano, "A miniature 7g jumping robot," in *Proc. IEEE Int. Conf. Robot. Autom.*, Pasadena, CA, USA, 2008, pp. 373–378.

[10] M. Kovac, M. Schlegel, J. Zufferey, and D. Floreano, “A miniature jumping robot with self-recovery capabilities,” in *Proc. IEEE/RSJ Int. Conf. Intell. Robots Syst.*, St. Louis, MO, USA, 2009, pp. 583–588.

[11] ——, “Steerable miniature jumping robot,” *Auton. Robots*, vol. 28, no. 3, pp. 295–306, 2010.

[12] M. A. Woodward and M. Sitti, “Design of a miniature integrated multi-modal jumping and gliding robot,” in *Proc. IEEE/RSJ Int. Conf. Intell. Robots Syst.*, San Francisco, CA, USA, 2011, pp. 556–561.

[13] J. Zhao, R. Yang, N. Xi, B. Gao, X. Fan, M. W. Mutka, and L. Xiao, “Development of a self-stabilization miniature jumping robot,” in *Proc. IEEE/RSJ Int. Conf. Intell. Robots Syst.*, St. Louis, MO, USA, 2009, pp. 2217–2222.

[14] J. Zhao, N. Xi, B. Gao, M. W. Mutka, and L. Xiao, “Design and testing of a controllable miniature jumping robot,” in *Proc. IEEE/RSJ Int. Conf. Intell. Robots Syst.*, Taipei, Taiwan, 2010, pp. 3346–3351.

[15] S. A. Stoeter and N. Papanikolopoulos, “Kinematic motion model for jumping scout robots,” *IEEE Trans. Robot. Autom.*, vol. 22, no. 2, pp. 398–403, 2006.

[16] A. Yamada, M. Watari, H. Mochiyama, and H. Fujimoto, “A compact jumping robot utilizing snap-through buckling with bend and twist,” in *Proc. IEEE/RSJ Int. Conf. Intell. Robots Syst.*, Taipei, Taiwan, 2010, pp. 389–394.

[17] S. Dubowsky, S. Kesner, J. Plante, and P. Boston, “Hopping mobility concept for search and rescue robots,” *Ind. Robot*, vol. 35, no. 3, pp. 238–245, 2008.

[18] R. Armour, K. Paskins, A. Bowyer, J. Vincent, and W. Megill, “Jumping robots: a biomimetic solution to locomotion across rough terrain,” *Bioinsp. Biomim.*, vol. 2, no. 3, pp. 65–82, 2007.

[19] Y. Sugiyama and S. Hirai, “Crawling and jumping by a deformable robot,” *Int. J. Robot. Res.*, vol. 25, no. 5-6, pp. 603–620, 2006.

[20] M. Noh, S.-W. Kim, S. An, J.-S. Koh, and K.-J. Cho, “Flea-inspired catapult mechanism for miniature jumping robots,” *IEEE Trans. Robotics*, vol. 28, no. 5, pp. 1007–1018, 2012.

[21] H. Tsukagoshi, M. Sasaki, A. Kitagawa, and T. Tanaka, "Design of a higher jumping rescue robot with the optimized pneumatic drive," in *Proc. IEEE Int. Conf. Robot. Autom.*, Barcelona, Spain, 2005, pp. 1276–1283.

[22] E. Watari, H. Tsukagoshi, A. Kitagawa, and T. Tanaka, "A higher casting and jump motions realized by robots using magnetic brake cylinder," *Journal of mechanisms and robotics*, vol. 3, no. 4, 2011.

[23] D. H. Kim, J. H. Lee, I. Kim, S. H. Noh, and S. K. Oho, "Mechanism, control, and visual management of a jumping robot," *Mechatronics*, vol. 18, no. 10, pp. 591–600, 2008.

[24] T. Tanaka and S. Hirose, "Development of leg-wheel hybrid quadruped airhopper: Design of powerful light-weight leg with wheel," in *Proc. IEEE Int. Conf. Robot. Autom.*, Pasadena, CA, USA, 2008, pp. 3890–3895.

[25] R. Niiyama, A. Nagakubo, and Y. Kuniyoshi, "Mowgli: A bipedal jumping and landing robot with an artificial musculoskeletal system," in *Proc. IEEE Int. Conf. Robot. Autom.*, Roma, Italy, 2007, pp. 2546–2551.

[26] R. Hayashi and S. Tsujio, "High-performance jumping movements by pendulum-type jumping machines," in *Proc. IEEE/RSJ Int. Conf. Intell. Robots Syst.*, Maui, USA, 2001, pp. 722–727.

[27] J. German, "Hop to it: Sandia hoppers leapfrog conventional wisdom about robot mobility," http://www.sandia.gov/LabNews/LN10-20-00/hop_story.html, 2000.

[28] E. Ackerman, "Boston dynamics sand flea robot demonstrates astonishing jumping skills," IEEE spectrum Robotics Blog, 2012.

[29] W. A. Churaman, A. P. Gerratt, and S. Bergbreiter, "First leaps toward jumping microrobots," in *Proc. IEEE/RSJ Int. Conf. Intell. Robots Syst.*, San Francisco, CA, USA, 2011, pp. 1680–1686.

[30] P. Zhang and Q. Zhou, "Voice coil based hopping mechanism for microrobot," in *Proc. IEEE Int. Conf. Robot. Autom.*, Kobe, Japan, 2009, pp. 3001–3006.

[31] R. M. Alexander, *Principles of Animal Locomotion.* Princeton University Press, 2003.

[32] R. Pfeifer, M. Lungarella, and F. Iida, "Self-organization, embodiment, and biologically inspired robotics," *Science*, vol. 318, no. 5853, pp. 1088–1093, 2007.

[33] A. J. Ijspeert, “Biorobotics: Using robots to emulate and investigate agile locomotion,” *Science*, vol. 346, no. 6206, pp. 196–203, 2014.

[34] C. Li, T. Zhang, and D. I. Goldman, “A terradynamics of legged locomotion on granular media,” *Science*, vol. 339, no. 6126, pp. 1408–1412, 2013.

[35] P. Birkmeyer, K. Peterson, and R. S. Fearing, “Dash: A dynamic 16g hexapedal robot,” in *Intelligent Robots and Systems. IROS 2009. IEEE/RSJ International Conference on*, 2009, pp. 2683–2689.

[36] N. J. Kohut, A. M. Hoover, K. Y. Ma, S. S. Baek, and R. S. Fearing, “Medic: A legged millirobot utilizing novel obstacle traversal,” in *Robotics and Automation (ICRA), 2011 IEEE International Conference on*, 2011, pp. 802–808.

[37] A. O. Pullin, N. J. Kohut, D. Zarrouk, and R. S. Fearing, “Dynamic turning of 13 cm robot comparing tail and differential drive,” in *Robotics and Automation (ICRA), 2012 IEEE International Conference on*, 2012, pp. 5086–5093.

[38] D. W. Haldane, K. C. Peterson, F. Garcia Bermudez, and R. S. Fearing, “Animal-inspired design and aerodynamic stabilization of a hexapedal millirobot,” in *Robotics and Automation (ICRA), 2013 IEEE International Conference on*, 2013, pp. 3279–3286.

[39] R. J. Wood, B. Finio, M. Karpelson, K. Ma, N. O. Pérez-Arancibia, P. S. Sreetharan, H. Tanaka, and J. P. Whitney, “Progress on pico air vehicles,” *The International Journal of Robotics Research*, vol. 31, no. 11, pp. 1292–1302, 2012.

[40] K. Y. Ma, P. Chirarattananon, S. B. Fuller, and R. J. Wood, “Controlled flight of a biologically inspired, insect-scale robot,” *Science*, vol. 340, no. 6132, pp. 603–607, 2013.

[41] J. Whitney, P. Sreetharan, K. Ma, and R. Wood, “Pop-up book mems,” *Journal of Micromechanics and Microengineering*, vol. 21, no. 11, p. 115021, 2011.

[42] M. Rubenstein, C. Ahler, and R. Nagpal, “Kilobot: A low cost scalable robot system for collective behaviors,” in *Robotics and Automation (ICRA), 2012 IEEE International Conference on*, 2012, pp. 3293–3298.

[43] F. Cintrón, K. Pongaliur, M. W. Mutka, L. Xiao, J. Zhao, and N. Xi, “Leveraging height in a jumping sensor network to extend network coverage,” *IEEE Trans. on Wireless Communications*, vol. 11, no. 5, pp. 1840–1849, 2012.

[44] E. Baird, N. Boeddeker, M. R. Ibbotson, and M. V. Srinivasan, "A universal strategy for visually guided landing," *Proceedings of the National Academy of Sciences*, vol. 110, no. 46, pp. 18 686–18 691, 2013.

[45] S. Bergbreiter, "Autonomous jumping microrobots," Ph.D. dissertation, University of California, Berkeley, Dec 2007.

[46] R. Armour, "A biologically inspired jumping and rolling robot," Ph.D. dissertation, University of Bath, May 2010.

[47] M. Kovac, "Bioinspired jumping locomotion for miniature robotics," Ph.D. dissertation, Swiss Federal Institute of Technology, Lausanne (EPFL), Switzerland, June 2010.

[48] E. Dupuis, S. Montminy, M. Farhad, and H. Champliaud, "Mechanical design of a hopper robot for planetary exploration," in *Proceedings of 9th ESA Workshop on Advanced Space Technologies for Robotics and Automation*, 2006.

[49] U. Scarfogliero, C. Stefanini, and P. Dario, "Design and development of the long-jumping "grillo" mini robot," in *Proc. IEEE Int. Conf. Robot. Autom.*, Roma, Italy, 2007, pp. 467–472.

[50] A. Yamada, M. Watari, H. Mochiyama, and H. Fujimoto, "An asymmetric robotic catapult based on the closed elastica for jumping robot," in *Proc. IEEE Int. Conf. Robot. Autom.*, Pasadena, CA, USA, 2008, pp. 232–237.

[51] S. Kesner, J. Plante, P. Boston, and S. Dubowsky, "A hopping mobility concept for a rough terrain search and rescue robot," in *Int. Conf. on Climbing and Walking Robots and Supporting Technologies for Mobile Machines (CLAWAR)*, Singapore, 2007, pp. 271–280.

[52] Y. Matsuyama and S. Hirai, "Analysis of circular robot jumping by body deformation," in *Proc. IEEE Int. Conf. Robot. Autom.*, Roma, Italy, 2007, pp. 1968–1973.

[53] T. Ho and S. Lee, "A shape memory alloy-actuated bio-inspired mesoscale jumping robot," *Int J Adv Robotic Sy*, vol. 9, no. 91, 2012.

[54] F. Kikuchi, Y. Ota, and S. Hirose, "Basic performance experiments for jumping quadruped," in *Proc. IEEE/RSJ Int. Conf. Intell. Robots Syst.*, Las Vegas, NV, USA, 2003, pp. 3378–3383.

[55] S. Bergbreiter and K. Pister, "Design of an autonomous jumping microrobot," in *Proc. IEEE Int. Conf. Robot. Autom.*, Roma, Italy, 2007, pp. 447–453.

[56] Y. Pei, F. Cintrón, M. Mutka, J. Zhao, and N. Xi, “Hopping sensor relocation in rugged terrains,” in *Proc. IEEE/RSJ Int. Conf. Intell. Robots Syst.*, 2009, pp. 3856–3861.

[57] S. Stoeter and N. Papanikolopoulos, “Autonomous stair-climbing with miniature jumping robots,” *IEEE Trans. Systems, Man, and CyberneticsPart B*, vol. 35, no. 2, pp. 313–325, 2005.

[58] T. Kane and M. Scher, “A dynamical explanation of the falling cat phenomenon,” *International journal of solids and structures*, vol. 5, no. 7, pp. 663–666, 1969.

[59] A. Jusufi, D. Goldman, S. Revzen, and R. Full, “Active tails enhance arboreal acrobatics in geckos,” *Proceedings of the National Academy of Sciences*, vol. 105, no. 11, pp. 4215–4219, 2008.

[60] T. Libby, T. Moore, E. Chang-Siu, D. Li, D. Cohen, A. Jusufi, and R. Full, “Tail-assisted pitch control in lizards, robots and dinosaurs,” *Nature*, vol. 481, no. 7380, pp. 181–184, 2012.

[61] G. B. Gillis, L. A. Bonvini, and D. J. Irschick, “Losing stability: tail loss and jumping in the arboreal lizard anolis carolinensis,” *Journal of Experimental Biology*, vol. 212, no. 5, pp. 604–609, 2009.

[62] E. Chang-Siu, T. Libby, M. Tomizuka, and R. J. Full, “A lizard-inspired active tail enables rapid maneuvers and dynamic stabilization in a terrestrial robot,” in *Proc. IEEE/RSJ Int. Conf. Intell. Robots Syst.*, San Francisco, CA, USA, 2011, pp. 1887–1894.

[63] A. Johnson, T. Libby, E. Chang-Siu, M. Tomizuka, R. Full, and D. Koditschek, “Tail assisted dynamic self righting,” in *Proceedings of the International Conference on Climbing and Walking Robots*, Baltimore, Maryland, USA, 2012, pp. 611–620.

[64] A. Demir, M. M. Ankarali, J. P. Dyhr, K. A. Morgansen, T. L. Daniel, and N. J. Cowan, “Inertial redirection of thrust forces for flight stabilization,” in *Proceedings of the International Conference on Climbing and Walking Robots*, Baltimore, Maryland, USA, 2012, pp. 239–245.

[65] R. Briggs, J. Lee, M. Haberland, and S. Kim, “Tails in biomimetic design: Analysis, simulation, and experiment,” in *Proc. IEEE/RSJ Int. Conf. Intell. Robots Syst.*, 2012, pp. 1473–1480.

[66] N. Kohut, A. Pullin, D. Haldane, D. Zarrouk, and R. Fearing, “Precise dynamic turning of a 10 cm legged robot on a low friction surface using a tail,” in *Proc. IEEE Int. Conf. Robot. Autom.*, Karlsruhe, Germany, 2013, pp. 3299–3306.

[67] C. Casarez, I. Penskiy, and S. Bergbreiter, “Using an inertial tail for rapid turns on a miniature legged robot,” in *Proc. IEEE Int. Conf. Robot. Autom.*, Karlsruhe, Germany, 2013, pp. 5469–5474.

[68] F. Van Breugel and M. H. Dickinson, “The visual control of landing and obstacle avoidance in the fruit fly drosophila melanogaster,” *The Journal of experimental biology*, vol. 215, no. 11, pp. 1783–1798, 2012.

[69] F. van Breugel, K. Morgansen, and M. H. Dickinson, “Monocular distance estimation from optic flow during active landing maneuvers,” *Bioinspiration & biomimetics*, vol. 9, no. 2, p. 025002, 2014.

[70] S. B. Fuller, A. D. Straw, M. Y. Peek, R. M. Murray, and M. H. Dickinson, “Flying drosophila stabilize their vision-based velocity controller by sensing wind with their antennae,” *Proceedings of the National Academy of Sciences*, vol. 111, no. 13, pp. E1182–E1191, 2014.

[71] F. T. Muijres, M. J. Elzinga, J. M. Melis, and M. H. Dickinson, “Flies evade looming targets by executing rapid visually directed banked turns,” *Science*, vol. 344, no. 6180, pp. 172–177, 2014.

[72] D. Floreano, R. Pericet-Camara, S. Viollet, F. Ruffier, A. Brückner, R. Leitel, W. Buss, M. Menouni, F. Expert, R. Juston *et al.*, “Miniature curved artificial compound eyes,” *Proceedings of the National Academy of Sciences*, vol. 110, no. 23, pp. 9267–9272, 2013.

[73] Y. M. Song, Y. Xie, V. Malyarchuk, J. Xiao, I. Jung, K.-J. Choi, Z. Liu, H. Park, C. Lu, R.-H. Kim *et al.*, “Digital cameras with designs inspired by the arthropod eye,” *Nature*, vol. 497, no. 7447, pp. 95–99, 2013.

[74] A. Beyeler, J.-C. Zufferey, and D. Floreano, “Vision-based control of near-obstacle flight,” *Autonomous robots*, vol. 27, no. 3, pp. 201–219, 2009.

[75] B. Herissé, T. Hamel, R. Mahony, and F.-X. Russotto, “Landing a vtol unmanned aerial vehicle on a moving platform using optical flow,” *Robotics, IEEE Transactions on*, vol. 28, no. 1, pp. 77–89, 2012.

[76] P.-E. Duhamel, N. O. Pérez-Arancibia, G. L. Barrows, and R. J. Wood, "Biologically inspired optical-flow sensing for altitude control of flapping-wing microrobots," *IEEE/ASME Transactions on Mechatronics*, vol. 18, no. 2, pp. 556–568, 2013.

[77] M. Srinivasan, S. Thurrowgood, and D. Soccol, "Competent vision and navigation systems," *IEEE Robotics & Automation Magazine*, vol. 16, no. 3, pp. 59–71, 2009.

[78] F. Chaumette and S. Hutchinson, "Visual servo control part I: Basic approaches," *IEEE Robot. Autom. Mag.*, vol. 13, no. 4, pp. 82–90, 2006.

[79] F. Chaumette, "Image moments: a general and useful set of features for visual servoing," *IEEE Trans. on Robotics*, vol. 20, no. 4, pp. 713–723, 2004.

[80] V. Kallem, M. Dewan, J. P. Swensen, G. D. Hager, and N. J. Cowan, "Kernel-based visual servoing," in *Proc. IEEE/RSJ Int. Conf. Intell. Robots Syst.*, San Diego, CA, USA, 2007, pp. 1975–1980.

[81] C. Collewet and E. Marchand, "Photometric visual servoing," *IEEE Transactions on Robotics*, vol. 27, no. 4, pp. 828–834, 2011.

[82] A. Dame and E. Marchand, "Mutual information-based visual servoing," *IEEE Transactions on Robotics*, vol. 27, no. 5, pp. 1–12, 2011.

[83] S. Han, A. Censi, A. D. Straw, and R. M. Murray, "A bio-plausible design for visual pose stabilization," in *Proc. IEEE/RSJ Int. Conf. Intell. Robots Syst.*, Taipei, Taiwan, 2010, pp. 5679–5686.

[84] J. Zhao, W. Yan, N. Xi, M. W. Mutka, and L. Xiao, "A miniature 25 grams running and jumping robot," in *Proc. IEEE Int. Conf. Robot. Autom.*, Hongkong, May 2014, pp. 5115–5120.

[85] M. Burrows, "Biomechanics: froghopper insects leap to new heights," *Nature*, vol. 424, no. 6948, pp. 509–509, 2003.

[86] S. Bergbreiter, "Effective and efficient locomotion for millimeter-sized microrobots," in *Proc. IEEE/RSJ Int. Conf. Intell. Robots Syst.*, Nice, France, 2008, pp. 4030–4035.

[87] F. Cintrón, K. Pongaliur, M. Mutka, and L. Xiao, "Energy balancing hopping sensor network model to maximize coverage," in *Proc. the 18th Int. Conf. Computer Communications and Networks*, San Francisco, CA, USA, 2009, pp. 1–6.

[88] J. Zhao, N. Xi, B. Gao, M. W. Mutka, and L. Xiao, "Development of a controllable and continuous jumping robot," in *Proc. IEEE Int. Conf. Robot. Autom.*, Shanghai, China, 2011, pp. 4614–4619.

[89] R. W. Fox, P. J. Pritchard, and A. T. McDonald, *Introduction to Fluid Mechanics*, 7th ed. John Wiley & Sons, Inc., 2008.

[90] A. M. Johnson, T. Libby, E. Chang-Siu, M. Tomizuka, R. J. Full, and D. E. Koditschek, "Tail assisted dynamic self righting," in *Proceedings of the Fifteenth International Conference on Climbing and Walking Robots*, July 2012, pp. 611–620.

[91] H. C. Bennet-Clark and G. M. Alder, "The effect of air resistance on the jumping performance of insects," *J. Exp. Biol.*, vol. 82, no. 1, pp. 105–121, 1979.

[92] R. M. Alexander, "Leg design and jumping technique for humans, other vertebrates and insects," *Philos. Trans. R. Soc. Lond. B Biol. Sci.*, vol. 347, pp. 235–248, 1995.

[93] L. Frantsevich, "Righting kinematics in beetles (insecta: Coleoptera)," *Arthropod Structure & Development*, vol. 33, no. 3, pp. 221–235, 2004.

[94] G. Domokos and P. L. Várkonyi, "Geometry and self-righting of turtles," *Proccedings of Royal Society: Biological Sciences*, vol. 275, no. 1630, pp. 11–17, 2008.

[95] J. A. Carretero, R. P. Podhorodeski, M. A. Nahon, and C. M. Gosselin, "Kinematic analysis and optimization of a new three degree-of-freedom spatial parallel manipulator," *ASME J. Mech. Des.*, vol. 122, no. 1, pp. 17–24, 2000.

[96] Y. Pei, F. Cintrón, M. Mutka, J. Zhao, and N. Xi, "Hopping sensor relocation in rugged terrains," in *IEEE/RSJ International Conference on Intelligent Robots and Systems (IROS)*, 2009, pp. 3856–3861.

[97] M. Sitti, A. Menciassi, A. Ijspeert, K. H. Low, and S. Kim, "Survey and introduction to the focused section on bio-inspired mechatronics," *IEEE/ASME Transactions on Mechatronics*, vol. 18, no. 2, pp. 409–418, 2013.

[98] J. Zhao, T. Zhao, N. Xi, F. J. Cintrón, M. W. Mutka, and L. Xiao, "Controlling aerial maneuvering of a miniature jumping robot using its tail," in *Proc. IEEE/RSJ Int. Conf. Intell. Robots Syst.*, Tokyo, Japan, 2013, pp. 3802–3807.

[99] J. Zhao, J. Xu, B. Gao, N. Xi, F. J. Cintron, M. W. Mutka, and L. Xiao, "MSU jumper: A single-motor-actuated miniature steerable jumping robot," *IEEE Trans. Robotics*, vol. 29, no. 3, pp. 602–614, 2013.

[100] Z. Li and R. Montgomery, "Dynamics and optimal control of a legged robot in flight phase," in *Proc. IEEE Int. Conf. Robot. Autom.*, Cincinnati, OH, USA, 1990, pp. 1816–1821.

[101] M. Berkemeier and R. Fearing, "Sliding and hopping gaits for the underactuated acrobot," *IEEE Transactions on Robotics and Automation*, vol. 14, no. 4, pp. 629–634, 1998.

[102] C. Chen and N. Sreenath, "Control of coupled spatial two-body systems with nonholonomic constraints," in *Proceedings of the 32nd IEEE Conference on Decision and Control*, 1993, pp. 949–954.

[103] T. Mather and M. Yim, "Modular configuration design for a controlled fall," in *Proc. IEEE/RSJ Int. Conf. Intell. Robots Syst.* IEEE, 2009, pp. 5905–5910.

[104] E. Yang, P. Chao, and C. Sung, "Landing posture control for a generalized twin-body system using methods of input–output linearization and computed torque," *IEEE/ASME Transactions on Mechatronics*, vol. 14, no. 3, pp. 326–336, 2009.

[105] ——, "Optimal control of an under-actuated system for landing with desired postures," *IEEE Transactions on Control Systems Technology*, vol. 19, no. 2, pp. 248–255, 2011.

[106] S. Agrawal and C. Zhang, "An approach to posture control of free-falling twin bodies using differential flatness," in *Proc. IEEE/RSJ Int. Conf. Intell. Robots Syst.*, 2010, pp. 685–690.

[107] E. Chang-Siu, T. Libby, M. Brown, R. J. Full, and M. Tomizuka, "A nonlinear feedback controller for aerial self-righting by a tailed robot," in *Proc. IEEE Int. Conf. Robot. Autom.*, Karlsruhe, Germany, 2013, pp. 32–39.

[108] H. K. Khalil, *Nonlinear systems*, 3rd ed. Prentice Hall, 2002.

[109] J. Zhao, T. Zhao, N. Xi, M. W. Mutka, and L. Xiao, "Msu tailbot: Controlling aerial maneuver of a miniature-tailed jumping robot," *IEEE/ASME Transactions on Mechatronics*, vol. PP, no. 99, pp. 1–12, 2015.

[110] E. Marchand and F. Chaumette, "Feature tracking for visual servoing purposes," *Robot. Auton. Syst.*, vol. 52, no. 1, pp. 53–70, 2005.

[111] J. Zhao, B. Song, N. Xi, and K. W. C. Lai, "Mutation analysis models for visual servoing in nanomanipulations," in *Proc. IEEE Int. Conf. Decision and Control*, Orlando, Florida, USA, 2011, pp. 5683–5688.

[112] J. Zhao, Y. Jia, N. Xi, W. Li, B. Song, and L. Sun, "Visual servoing using non-vector space control theory," in *IEEE/ASME International Conference on Advanced Intelligent Mechatronics*, KaoHsiung, Taiwan, 2012, pp. 1–6.

[113] J. P. Aubin, *Mutational and Morphological Analysis: Tools for Shape Evolution and Morphogenesis.* Birkhäuser, 1998.

[114] T. Lorenz, "A viability theorem for morphological inclusions," *SIAM J. Control Optim.*, vol. 47, no. 3, pp. 1591–1614, 2008.

[115] ——, "Morphological control problems with state constraints," *SIAM J. Control Optim.*, vol. 48, no. 8, pp. 5510–5546, 2010.

[116] ——, "Set-valued maps for image segmentation," *Comput Visual Sci*, vol. 4, no. 1, pp. 41–57, 2001.

[117] L. Doyen, "Mutational equations for shapes and vision-based control," *Journal of Mathematical Imaging and Vision*, vol. 5, no. 2, pp. 99–109, 1995.

[118] A. Goradia, N. Xi, Z. Cen, and M. W. Mutka, "Modeling and design of mobile surveillance networks using a mutational analysis approach," in *Proc. IEEE/RSJ Int. Conf. Intell. Robots Syst.*, Alberta, Canada, 2005, pp. 3003–3008.

[119] T. Lorenz, *Mutation Analysis: A Joint Framework for Cauchy Problems in and Beyond Vector Spaces.* Springer, 2010.

[120] W. Rudin, *Principles of Mathematical Analysis*, 3rd ed. McGraw-Hill Science, 1976.

[121] H. K. Khalil, *Nonlinear Systems*, 3rd ed. Prentice Hall, 2001.

[122] M. C. Delfour and J.-P. Zolésio, *Shapes and Geometries: Metrics, Analysis, Differential Calculus, and Optimization*, 2nd ed. Society for Industrial and Applied Mathematics, 2011.

[123] L. Doyen, "Shape laypunov functions and stabilization of reachable tubes of control problems," *Journal of Mathematical Analysis and Applications*, vol. 184, no. 2, pp. 222–228, 1994.

[124] S. Hutchinson, G. D. Hager, and P. I. Corke, "A tutorial on visual servo control," *IEEE Trans. Robot. Autom.*, vol. 12, no. 5, pp. 651–670, 1996.

[125] M. W. Spong, S. Hutchinson, and M. Vidyasagar, *Robot Modeling and Control.* John Wiley & Sons, Inc., 2006.

[126] H. Wang, Y. Jia, N. Xi, and J. Buether, "An online motion plan algorithm for a 7dof redundant manipulator," in *IEEE Conference on Robotics and Biomimetics*, Tianjin, China, 2010, pp. 1057–1062.

[127] X. Li, Y. Jia, N. Xi, and A. Song, "Image based approach to obstacle avoidance in mobile manipulators," in *IEEE Conference on Robotics and Biomimetics*, Phuket Island, Thailand, 2011, pp. 1658–1663.

[128] J. Romberg, "Imaging via compressive sampling," *IEEE Signal Processing Magazine*, vol. 25, no. 2, pp. 14–20, 2008.

[129] J. Zhao, B. Song, N. Xi, K. W. C. Lai, H. Chen, and C. Qu, "Compressive feedback based non-vector space control," in *Proc. of the American Control Conference*, Montreal, Canada, 2012, pp. 4090–4095.

[130] J. Zhao, N. Xi, L. Sun, and B. Song, "Stability analysis of non-vector space control via compressive feedbacks," in *IEEE 51st Annual Conference on Decision and Control (CDC)*, Maui, Hawaii, USA, 2012, pp. 5685–5690.

[131] M. Wakin, B. Sanandaji, and T. Vincent, "On the observability of linear systems from random, compressive measurements," in *IEEE Conference on Decision and Control*, Atlanta, Georgia, 2010, pp. 4447–4454.

[132] B. M. Sanandaji, T. L. Vincent, M. B. Wakin, R. Toth, and K. Poolla, "Compressive system identification of LTI and LTV ARX models," in *IEEE Conference on Decision and Control and European Control Conference*, Orlando, Florida, 2011, pp. 791–798.

[133] W. Dai and S. Yuksel, "Observability of a linear system under sparsity constraints," *IEEE Transactions on Automatic Control*, vol. 58, no. 9, pp. 2372–2376, 2013.

[134] S. Bhattacharya and T. Basar, "Sparsity based feedback design: A new paradigm in opportunistic sensing," in *Proc. of the American Control Conference*, San Francisco, CA, USA, 2011, pp. 3704–3709.

[135] M. Nagahara and D. E. Quevedo, "Sparse representations for packetized predictive networked control," in *Proc. IFAC World Congr.*, Milano, Italy, 2011, pp. 84–89.

[136] M. Nagahara, T. Matsuda, and K. Hayashi, “Compressive sampling for remote control systems,” *IEICE TRANSACTIONS on Fundamentals of Electronics, Communications and Computer Sciences*, vol. 95, no. 4, pp. 713–722, 2012.

[137] E. Candès and T. Tao, “Near-optimal signal recovery from random projections: universal encoding strategies?” *IEEE Trans. Inform. Theory*, vol. 52, no. 12, pp. 5406–5425, 2006.

[138] M. A. Davenport, M. F. Duarte, Y. Eldar, and G. Kutyniok, *Introduction to Compressed Sensing.* Cambridge University Press, 2012, ch. One.

[139] E. J. Candès, “The restricted isometry property and its implications for compressed sensing,” *Comptes Rendus Mathematique*, vol. 346, no. 9, pp. 589–592, 2008.

[140] R. A. DeVore, “Deterministic constructions of compressed sensing matrices,” *Journal of Complexity*, vol. 23, no. 4-6, pp. 918–925, 2007.

[141] R. Baraniuk, M. Davenport, R. Devore, and M. Wakin, “A simple proof of the restricted isometry property for random matrices,” *Constructive Approximation*, vol. 28, no. 3, pp. 253–263, 2008.

[142] M. Rudelson and R. Vershynin, “On sparse reconstruction from Fourier and Gaussian measurements,” *Commun. Pure Appl. Math.*, vol. 61, no. 8, pp. 1025–1045, 2008.

[143] D. Needell and J. A. Tropp, “CoSaMP: Iterative signal recovery from incomplete and inaccurate samples,” *Applied and Computational Harmonic Analysis*, vol. 26, no. 3, pp. 301–321, 2009.

[144] B. Song, J. Zhao, N. Xi, H. Chen, K. W. C. Lai, R. Yang, and L. Chen, “Compressive feedback-based motion control for nanomanipulation—theory and applications,” *IEEE Transactions on Robotics*, vol. 30, no. 1, pp. 103–114, 2014.